MODELING CHAR OXIDATION AS A FUNCTION OF PRESSURE USING AN INTRINSIC LANGMUIR RATE EQUATION

by

Jianhui Hong

A dissertation submitted to the faculty of

Brigham Young University

in partial fufillment of the requirements for the degree of

Doctor of Philosophy

Department of Chemical Engineering

Brigham Young Univeristy

April 2000

BRIGHAM YOUNG UNIVERSITY

GRADUATE COMMITTEE APPROVAL

of a dissertation submitted by

Jianhui Hong

This dissertation has been read by each member of the following graduate committee and by majority vote has been found to be satisfactory.

Date	Thomas H. Fletcher, Chair
Date	L. Douglas Smoot
Date	William C. Hecker
Date	Calvin H. Batholomew
Date	W. Vincent Wilding

BRIGHAM YOUNG UNIVERSITY

As chair of the candidate's graduate committee, I have read the dissertation of Jianhui Hong in its final form and have found that (1) its format, citations, and bibliographical style are consistent and acceptable and fufill university and department style requirements; (2) its illustrative materials including figures, tables, and charts are in place; and (3) the final manuscript is satisfactory to the graduate committee and is ready for submission to the university library.

Date

Thomas H. Fletcher
Chair, Graduate Committee

Accepted for the Department

Kenneth A. Solen
Department Chair

Accepted for the College

Douglas M. Chabries
Dean, College of Engineering and Technology

ABSTRACT

MODELING CHAR OXIDATION AT ATMOSPHERIC AND ELEVATED PRESSURES USING AN INTRINSIC LANGMUIR RATE EQUATION AND AN EFFECTIVENESS FACTOR

Jianhui Hong

Chemical Engineering Department

Doctor of Philosophy

A global n-th order rate equation is often used to model char oxidation rates at atmospheric pressure. However, it was recently shown that this approach was inadequate for modeling char oxidation rates as a function of total pressure. It is generally thought that in order to model the effects of total pressure, an intrinsic modeling approach (i.e., pore diffusion effects are accounted for explicitly) is required, and a Langmuir-Hinshelwood type expression is needed. The objective of this project was to develop a model that can be used to explain and unify char oxidation rates over wide ranges of experimental conditions (including temperature, total pressure, oxygen mole fraction, particle size, etc.) without excessive computational efforts.

In this project a new High Pressure Carbon Burnout Kinetics (HP-CBK) model was developed on the basis of the CBK model by Hurt and his co-workers. The HP-

CBK model uses: 1) an intrinsic Langmuir rate equation rather than global n-th order kinetics; 2) an analytical solution of the effectiveness factor for the Langmuir rate equation with a correction function (developed in this project) to improve its accuracy; 3) a pore structure model for calculation of the effective diffusivity, taking into account both Knudsen diffusion and molecular diffusion; and 4) general correlations for Nusselt and Sherwood numbers, which allow the HP-CBK model to be used for both entrained-flow, pulverized char oxidation and large-particle combustion in fixed beds. The HP-CBK model was evaluated by comparison with five sets of experimental measurements: 1) graphite flake oxidation data; 2) rough sphere combustion data; 3) large particle oxidation data; 4) pulverized char drop-tube data, and 5) TGA and FFB data from this study. Results showed that the HP-CBK model was able to quantitatively explain: 1) the effects of temperature, total gas pressure, oxygen mole fraction, particle size and gas velocity on reaction rates, and 2) the change of reaction order with temperature and oxygen partial pressure. Therefore, the Langmuir rate equation, when used with the appropriate effectiveness factor, seems to be satisfactory for modeling char oxidation over wide ranges of experimental conditions.

ACKNOWLEDGEMENTS

I would like to thank my graduate advisor, Professor Thomas H. Fletcher, for his guidance, friendship and financial support during the course of this project. I have learned a great deal from his daily conduct and leadership. I am grateful to the Chemical Engineering Department and Brigham Young University for providing me the opportunity to study here and get to know the truth. Special thanks to Dr. Robert Hurt at Brown University for proving the source code of the CBK model. Funding contributed by ACERC is also gratefully acknowledged.

I would like to thank those with whom I have exchanged so many ideas, namely Steven Perry, Haifeng Zhang, Paul and Mary Goodman, Rebecca Sawaya, Joshua Wong and Jared Parker. I am especially indebted to Steven Perry, who is always willing and ready to help others, and cares so much about others. Lastly I would like to thank my lovely wife, Jinru Wu, for her unending support throughout the pursuit of this degree.

Table of Contents

List of Figures

List of Tables

Nomenclature

A	pre-exponential factor
A_1	pre-exponential factor for k_1
A_{1p}	pre-exponential factor for k_{1p}
A_p	pre-exponential factor of K_p
a	coefficient in the discretization equation
A_c	pre-exponential factor for the $\mathrm{CO/CO_2}$ product ratio
AFR	Advanced Fuel Research
ASA	active surface area
ASTM	American Society of Testing and Materials
atm	atmosphere
B	particle dry ash-free burnout
BYU	Brigham Young University
b	constant term in the discretization equation
C	carbon
C	oxygen concentration, mol/cm^3
CBA	cantilever balance attachment
CBK	Carbon Burnout Kinetics model
C_f	total gas concentration at film temperature, equal to $P/(RT_f)$
CHNS	four elements in coal or char: carbon, hydrogen, nitrogen and sulfur
C_g	bulk stream oxygen concentration, mol/m^3
C_{og}	same as C_g
C_p	heat capacity
C_s	oxygen concentration at particle surface, mol/cm^3
D	diffusivity, cm^2/sec
D_1	macro diffusivity, cm^2/sec
D_2	micro diffusivity, cm^2/sec
D_{AB}	molecular diffusivity, cm^2/sec
D_{ABf}	molecular diffusivity at film temperature, cm^2/sec
D_e	effective diffusivity, cm^2/sec
D_K	Knudsen diffusivity, cm^2/sec
DOE	Department of Energy
d	same as $\mathrm{d_p}$, particle diameter
d_p	particle diameter
E	neighbor in the positive x direction, i.e., on the east side
E	activation energy, kcal/mol
E_1	activation energy for k_1, kcal/mol
E_{1p}	activation energy for k_{1p}, kcal/mol
E_a	activation energy of adsorption, kcal/mol
E_c	activation energy of the $\mathrm{CO/CO_2}$ product ratio, kcal/mol

E_d	activation energy of desorption, kcal/mol
E_{obs}	observed activation energy
E_p	activation energy for K_p, kcal/mol
E_{true}	true activation energy, kcal/mol
f_c	correction function
FFB	flat-flame burner
HP-CBK	High Pressure Carbon Burnout Kinetics model, developed in this study
HPCP	high pressure controlled-profile reactor
h	heat transfer coefficient, cal/cm^2/K
h_{xm}	mass transfer coefficient, mol/cm^2/sec
K	rate constant in the Langmuir rate equation, $K= A\ exp(-E/RT)$, cm^3/mol
K_p	equal to (K/RT), $K_p = A_p\ exp(-E_p/RT)$, atm^{-1}
K	Kelvin
k	rate constant
k_0	defined as k_1/K, equal to k_{1p}/K_p, mol/cm^3/sec
k_1	rate constant in the Langmuir rate equation, $k_1 = A_1\ exp(-E_1/RT)$, sec^{-1}
k_{1p}	equal to (k_1/RT), $k_{1p} = A_{1p}\ exp(-E_{1p}/RT)$, mol C/cm^3/sec/atm
k_a	adsorption rate constant
k_c	surface migration rate constant
k_d	desorption rate constant
k_D	composite parameter related to mass transfer, g/cm^2/sec/atm
k_m	rate constant in the m-th order rate equation, (mol C/cm^3)$^{1-m}$ sec^{-1}
k_{mp}	equal to $k_m/(RT)^m$
k_{xm}	mass transfer coefficient, mol/cm^2/sec
L	characteristic length, V_p/S_g , cm
L	reaction length between injection and collection points, cm
M_1	an intermediate modulus in the discretization equation
m	mass, g
m	intrinsic (true) reaction order
M_C	molecular weight of carbon, 12
m_{obs}	observed reaction order in Zone I
MR	product CO/CO_2 mole ratio
M_T	general (Thiele) modulus
N	nitrogen
N	neighbor in the positive y direction, i.e., on the north side
N	molar flux, mol/cm^2/sec
N	the number of layers into which the spherical particle is divided
N_p	the number of pores in a char particle
n	the reaction order in the n-th order rate equation
n_{obs}	observed reaction order in Zone II
O	oxygen
P	central grid point under consideration
P, P_{tot}	total gas pressure, atm
PCFB	pressurized circulating fluidized bed
PCGC-3	Pulverized Coal Gasification and Combustion code (3 dimensional)
P_∞	oxygen partial pressure in the bulk stream, atm

P_{os}, P_s	oxygen partial pressure at particle surface, atm
Pr	Prandtl number
q	carbon consumption rate in the form of mass flux, g/cm^2/sec
q_{diff}	mass flux from boundary layer diffusion consideration, g/cm^2/sec
q_{heat}	mass flux from energy balance consideration, g/cm^2/sec
q_{max}	maximum mass flux allowed by boundary layer diffusion, g/cm^2/sec
q_{obs}	observed mass flux, g/cm^2/sec
q_{ps}	converged value of mass flux determined from the P_s loop; when the P_s loop is converged, $q_{ps} = q_{diff} = q_{rxn}$
q_{rxn}	mass flux from reaction kinetics consideration, g/cm^2/sec
R	gas constant, 1.987 cal/mol/K
Re	Reynolds number
r	radial distance from the particle center
r_{in}'''	intrinsic reaction rate per unit volume of particle, mol C/cm^3/sec
r_{obs}'''	observed reaction rate per unit volume of particle, mol C/cm^3/sec
r_{obs}''	observed reaction rate per unit external surface area of particle, mol-C/cm^2/sec
r_{p1}	average macropore radius
r_{p2}	average micropore radius
$r_{p,crit}$	critical pore radius
r_{obs}'''	observed reaction rate per unit volume of particle, mol C/cm^3/sec
r_s	radius of the particle
S	sulfur
S	neighbor in the negative y direction, i.e., on the south side
Sc	Schmidt number
S_{ext}	external surface area of a particle, equal to $4\pi d_p^2\Omega$, cm^2
S_g	geometric external surface area of a particle, equal to $4\pi d_p^2$, cm^2
Sh	Sherwood number
S_{int}	internal surface area of a particle, cm^2
S_m	surface area per unit mass, cm^2/g
SNDL	simple, non-dissociative Langmuir rate equation (often referred to in this dissertation as the Langmuir rate equation for simplicity)
S_{pore}	the surface area of a single pore, cm^2
S_{tot}	total surface area of a particle, $S_{tot} = (S_{ext} + S_{int})$
T	temperature, K
T_f	same as T_m, film temperature, K
T_g	gas temperature, K
TGA	thermogravimetric analysis
T_m	film temperature, equal to $(T_p + T_g)/2$, K
T_p	particle temperature, K
T_w	wall temperature, K
U	unburned fraction of carbonaceous material, equal to $(1 - B)$
V_p	the total volume of a particle, cm^3
V_{pore}	the volume of a single pore
v_a	the volume of ash in a char particle

v_c	the volume of combustible material in a char particle
W	neighbor in the negative x direction, i.e., on the west side
x	oxygen mole fraction
x_a	fraction of ash

Greek symbols

α	power index of the normalized density-diameter relationship
χ	observed reaction rate over the maximum reaction rate allowed by boundary layer diffusion
ΔH_1	heat of reaction for $C + O_2 \rightarrow CO_2$
ΔH_2	heat of reaction for $C + 0.5O_2 \rightarrow CO$
ε	emissivity
ε	second effectiveness factor
ε	total porosity
ε_M	macro porosity
ε_μ	micro porosity
γ	$(\psi - 1)/(\psi + 1)$
η	effectiveness factor
λ	thermal conductivity
ν_o, ν_O, ν_{O2}	stoichiometric coefficient of oxygen for each mole of carbon consumed
θ	fraction of covered carbon sites
θ	normalized oxygen concentration, equal to C/C_s
ρ, ρ_p	particle density, g/cm^3
ρ_{app}	apparent density, same as particle density, g/cm^3
ρ_b	bed density, defined as mass of particle/(volume of solid + intra-particle void volume + inter-particle void volume)
ρ_a	density of ash, g/cm^3
ρ_c	density of combustible material, g/cm^3
τ	tortuosity factor
Ω	roughness factor
ξ	normalized r, equal to r/r_s
ψ	fraction of carbon converted to CO_2 for each mole of carbon consumed

Subscript

a	ash
c	combustible material
diff	diffusion
E	neighbor in the positive x direction
e	effective
f	at film temperature, $T_f = 0.5(T_p + T_g)$
g	bulk steam

in	intrinsic
K	Knudsen diffusion
M	macro
o	initial
obs	observed
P	central grid point under consideration
rxn	reaction
W	neighbor in the negative x direction
s	on external surface
μ	micro
∞	in the bulk stream

1. Introduction

Background

The rate of char oxidation is an important issue in coal utilization. Char oxidation is the rate-determining primary step in coal combustion. The other primary step, devolatilization, typically occurs about an order of magnitude faster (Smith, 1982). The kinetics of char oxidation determine the pattern of heat release in combustors, which may be important in influencing other variables, including NO_x formation (Bar-Ziv *et al.*, 1989). Unburned carbon in fly ash affects many aspects of power plant performance and economy, including boiler efficiency, electrostatic precipitation of fly ash particulates and the value of fly ash as salable byproduct (Tyson and Blackstock, 1995; Hurt, 1998). High carbon content prevents the sale of the fly ash to cement and construction industries, and necessitates the disposal of the fly ash at the expense of the producer (Hurt, 1998). Although acceptably low unburned carbon levels are achieved for many traditional steam coals, combustion zone modifications for NO_x control have made the task of maintaining low residual carbon levels in boiler fly ash much more difficult (Fiveland and Jamaluddin, 1992). In order to keep unburned carbon below a certain level, knowledge of the char oxidation rate, especially during late burnout, is essential in boiler design and operation.

Technologies have been under development to burn coal more efficiently and cleanly. Among these technologies, two have attracted increasing interest around the world: pressurized fluidized bed combustion and high pressure coal gasification (Balzhiser and Yeager, 1987). In these processes, high pressure is used to reduce the required size of reactors and to increase the conversion efficiency to electric power in combined-cycle power plants.

While much research has been conducted on char oxidation at atmospheric pressure, relatively few char oxidation experiments have been conducted at elevated pressures. Among these experiments, drop tube experiments and TGA (or fixed-bed) experiments have provided the most useful kinetic data for char oxidation at elevated pressures. Other high pressure experiments, such as pressurized, fluidized bed combustion, are less helpful in providing kinetic data due to the complex flow patterns involved.

A global *n*-th order rate equation is often used to model char oxidation rates at atmospheric pressure. The global *n*-th order approach, however, was recently shown to be inadequate in modeling char oxidation rates when total pressure is varied (Monson, 1992; Monson *et al.*, 1995). It is generally thought that in order to model the effects of total pressure over a broad temperature range, an intrinsic modeling approach (i.e., pore diffusion effects are accounted for explicitly) is required, and a Langmuir-Hinshelwood type expression is needed (Essenhigh, 1988; Essenhigh, 1991; Banin *et al.*, 1997; Du *et al.*, 1991; Croiset *et al.*, 1996). A Langmuir-Hinshelwood type expression can reflect the physical processes involved in the carbon-oxygen reaction and thus hold more potential in modeling char oxidation rates at elevated pressures. A significant challenge of using a Langmuir-Hinshelwood type expression lies in accounting for the pore diffusion effects in a numerically economic manner. Methods of accounting for pore diffusion effects on such rate expressions will be explored in this project.

Organization of this Dissertation

First, literature pertinent to high pressure char oxidation is presented in Chapter 2. The objective and approach used in this study are explained in Chapter 3. Analytical expressions are developed to accurately predict the effectiveness factors for *m*-th order rate equations and the Langmuir rate equation in Chapter 4. Some theoretical developments related to high pressure char oxidation are presented in Chapter 5. Next, the CBK model developed at Brown University is detailed in Chapter 6, from which an improved model (referred to as the HP-CBK model) is developed to model char oxidation rates over a wide range of temperature and gas pressure. The HP-CBK model is evaluated with high pressure char oxidation data in Chapter 7. Finally, a summary is given in Chapter 8, and several recommendations are made in Chapter 9.

A limited series of experiments was performed in the early stages of this Ph.D. project to determine the influence of steam and oxygen on char properties and reactivity. Later, some of the data from these experiments were found useful in the modeling project that was the main focus of this dissertation. These experiments are described in Appendix A in order to preserve the modeling focus in the main text of this dissertation.

2. Literature Review

This chapter reviews previous studies of char oxidation with the emphasis on issues directly or indirectly related to the effects of total gas pressure. Reviews on general issues in modeling char oxidation are available in the literature (Walker *et al.*, 1959; Laurendeau, 1978; Essenhigh, 1981; Smith, 1982; Simons, 1983; Sotirchos *et al.*, 1984; Smoot and Smith, 1985; Morrison, 1986; Prado *et al.*, 1987; Smoot, 1991; and Annamalai and Ryan, 1993).

The Three-Zone Theory

The rate of char oxidation is controlled by the sequential or parallel processes of boundary layer diffusion, chemical reaction and pore diffusion. Several investigators, such as Walker *et al.* (1959) and Gray *et al.* (1976) have postulated the existence of the three different temperature zones or regimes in which one or more different processes control the overall reaction rate. This classic “three-zone” theory has been widely accepted and used to interpret experimental data in char oxidation literature.

In Zone I, which occurs when chemical reaction is slow compared to diffusion (at low temperature or for small particles), chemical reaction is the rate-determining step. In Zone II, reaction rate is controlled by both chemical reaction and pore diffusion. Zone III, which occurs at high temperatures, is characterized by mass-transfer limitations in the boundary layer of the particle. Figure 2.1 illustrates these zones graphically and indicates the theoretical dependence of the reaction rate on oxygen concentration (Smoot and Smith, 1985).

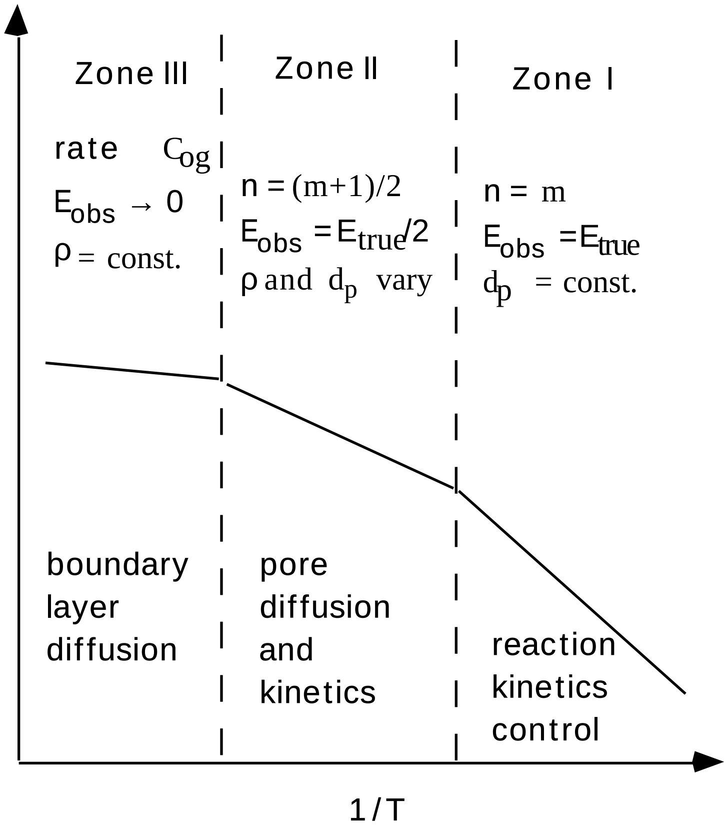

Figure 2.1. Rate-controlling zones for heterogeneous char oxidation.

It should be noted that the three-zone theory idealizes and simplifies the actual variation of reaction rate with temperature. First, the “three-zone” theory assumes that boundary layer diffusion (BLD) resistance dominates in Zone III, is present during the transition from Zone II to Zone III, and is totally absent from Zone I to Zone II. In reality, BLD resistance is often present in Zone II. In other words, char oxidation rate is typically influenced by all three processes: BLD, pore diffusion, and chemical kinetics. Second, the three-zone theory applies only to *m*-th order kinetics and fails to predict the variation of reaction rate with temperature for Langmuir-Hinshelwood kinetics. For example, Essenhigh (1991) suggested that the true activation energy of the char-oxygen reaction changed from 32.95 kcal/mol to 10.04 kcal/mol (corresponding to desorption control and adsorption control, respectively) as temperature increased. Third, the three-zone theory assumes that the combustion rate contributed from the external surface area is negligible compared to the rate contributed from the internal surface area. This assumption is true for most cases, since the internal surface area is typically much larger than the external surface. However, the external surface area can become important under some conditions, these being favored by low internal surface area (typically in highly ordered carbons) or severe pore diffusion limitations, which lead to an extremely low effectiveness factor (Hurt, 1998). When the external combustion rate cannot be neglected compared to the internal combustion rate, the so-called “rough sphere combustion” occurs (Banin *et al*., 1997a, b).

Char Oxidation Model Classifications

Char oxidation models can be classified into two main categories: global models and intrinsic models (Smith *et al*., 1994). Global models consider char particles impervious to pore diffusion effects or else lump intraparticle diffusion effects into the chemical reaction rate constants. These models are highly empirical, basing the reaction rate on the particle’s external surface area and on the oxidizer concentration at the external surface. In contrast, intrinsic models relate char oxidation rate to the active surface area involved in the reaction and consider the non-uniform oxidizer concentration profile within the particle. Intrinsic models rely on pore structure models to describe gaseous diffusion through complex pore structures and to model the local oxidizer concentration at the active surface area. Thus the intrinsic model approach has the potential of providing coal-general kinetic rate constants instead of the coal-specific and condition-specific constants used in the global models.

Intrinsic models vary in levels of sophistication and can be classified into two subcategories: macroscopic and microscopic (Laurendeau, 1978; Reade, 1996). Macroscopic models use average properties of the particle to estimate the effective diffusivity in the porous structures in the char particle, and usually do not model the evolution of pore structure with burnout. In other words, macroscopic models assume spatially uniform properties (porosity, pore size and surface reactivity) and temporally invariant pore structures. Spatially uniform properties are required to solve for the analytical solutions of the effectiveness factor, which saves substantial computational time over the numerical solutions. Microscopic models involve the development of a reaction model for a single pore and then the prediction of the overall particle reactivity by an appropriate statistical description of the pore size distribution (Laurendeau, 1978). Microscopic models use a pore structure model to approximate the spatial and temporal variations in local diffusivity, pore structure, and surface area. If the pore structure is not allowed to change with conversion, and the properties of particle are assumed to be uniform, then the microscopic approach becomes equivalent to the macroscopic approach. Microscopic models have the potential to capture the effects of burnout on reactivity. However, these models are numerically combersome and generally less desirable as submodels in comprehensive combustion codes (Cope, 1995).

Microscopic models can be further classified into discrete and continuum models, depending on whether the pore space and solid are treated as discrete phases or as continuum phases (Sahu *et al.*, 1989; Sahimi, 1990). Generally, the discrete models are too complicated for practical use and therefore are seldom used. Several continuum, microscopic models were reviewed by Smith *et al.* (1994).

Stoichiometry of the Carbon-Oxygen Reaction

CO and CO_2 are two possible products of char oxidation. The overall reactions leading to these two products are, respectively,

$$C + O_2 \rightarrow CO_2 + \Delta H_1 \tag{2.1}$$

$$C + \frac{1}{2} O_2 \rightarrow CO + \Delta H_2 \tag{2.2}$$

where ΔH_1 and ΔH_2 are the heats of reaction for Reactions 2.1 and 2.2. If the fraction of carbon converted to CO_2 is denoted as ψ, the overall carbon-oxygen reaction can be expressed as

$$C + \frac{1+\psi}{2} O_2 \rightarrow \psi CO_2 + (1-\psi) CO + \psi \Delta H_1 + (1-\psi) \Delta H_2 \tag{2.3}$$

The stoichiometric coefficient of oxygen in the above equation is denoted as ν_o. That is,

$$\nu_o = \frac{1+\psi}{2} \tag{2.4}$$

The fraction of carbon converted to CO_2 (ψ) is often calculated from the CO/CO_2 product ratio, which is often empirically correlated with an Arrhenius equation (Arthur, 1951; Tognotti *et al.*, 1990; Mitchell *et al.*, 1992):

$$\frac{CO}{CO_2} = \frac{1-\psi}{\psi} = A_c \exp(-\frac{E_c}{RT_P}) \tag{2.5}$$

The stoichiometric coefficient of oxygen represents a major uncertainty in modeling char oxidation.

Boundary Layer Diffusion

The molar flux of oxygen, N_{O2}, in the bulk phase can be related to the surface mole fraction (Bird *et al.*, 1960):

$$N_{O2} - x_s(N_{O2} + N_{CO} + N_{CO2}) = k_{xm}(x_\infty - x_s) \tag{2.6}$$

where N denotes the molar flux of a substance, x_∞ is the oxygen mole fraction in the bulk stream, x_s is the oxygen mole fraction at the external surface of the particle, and k_{xm} is the mass transfer coefficient and can be obtained from the Sherwood number correlation for spheres in a convective flow (Bird *et al.*, 1960; Field *et al.*, 1967; Mulcahy and Smith, 1969)

$$\frac{k_{xm} d_p}{C_f D_{ABf}} = Sh = 2.0 + 0.60\mathrm{Re}^{1/2}\ Sc^{1/3} \tag{2.7}$$

where Sh is the Sherwood number, C_f is the total gas concentration at the film temperature, D_{ABf} is the molecular diffusivity at the film temperature, Re is the Reynolds number, and Sc is the Schmidt number. Note that in Eq. 2.6, the positive flux direction is designated as the direction from the bulk phase to the particle. As a result, N_{CO} and N_{CO2} take negative values. Using the stoichiometric relations in Eq. (2.3), N_{CO} and N_{CO2} in Eq. (2.4) can be expressed in terms of N_{O2}. Eq. 2.6 can be re-written as

$$N_{O2} - x_s \gamma\ N_{O2} = \frac{C_f D_{ABf} Sh}{d_p}(x_\infty - x_s) \tag{2.8}$$

where $$\gamma = \frac{\psi - 1}{\psi + 1} \tag{2.9}$$

The oxygen molar flux can be converted to carbon consumption rate q_{diff} (gC/cm^2/sec) by multiplying the molecular weight of carbon and the reciprocal of the stoichiometric coefficient of oxygen

$$q_{diff}(1-x_s\gamma) = \frac{M_C}{\nu_o}\frac{c_f D_{ABf} Sh}{d_p}(x_\infty - x_s) \tag{2.10}$$

It is convenient to define a new parameter k_D as

$$k_D = \frac{M_C}{\nu_o}\frac{c_f D_{ABf} Sh}{d_p}\frac{1}{P} = \frac{M_C}{\nu_o}\frac{D_{ABf} Sh}{d_p}\frac{1}{RT_f} \tag{2.11}$$

Eq. 2.10 can thus be written as

$$q_{diff}(1-\frac{P_s}{P}\gamma) = k_D(P_\infty - P_s) \tag{2.12}$$

The net mass diffusion rate (N_{O2} + N_{CO} + N_{CO2}) is often neglected (equivalent to assuming equil-molar counter diffusion), and the above equation is further simplified to

$$q_{diff} = k_D(P_\infty - P_s) \tag{2.13}$$

Despite the widespread use of this simplified equation (Smith, 1982; Essenhigh, 1988), the more accurate form (Eq. 2.12) is recommended.

At high temperatures, surface reaction is so fast that the surface oxygen partial pressure approaches zero, and the overall reaction rate approaches the maximum value allowed by boundary layer diffusion:

$$q_{\max} = q_{diff}\big|_{P_s=0} = k_D P_\infty \tag{2.14}$$

In this case the overall reaction rate is solely controlled by boundary layer diffusion. This situation is also called Zone III combustion.

In the char combustion literature, the χ factor is often used to determine the importance of boundary layer diffusion effects. The χ factor is defined as the observed reaction rate (g/sec/cm^2) over the maximum reaction rate allowed by boundary layer diffusion (g/sec/cm^2):

$$\chi = \frac{q_{obs}}{q_{\max}} \tag{2.15}$$

The χ factor can be used as a criterion of whether combustion occurs in Zone III. Combustion is considered occurring in Zone III when the χ factor is close to unity. For example, Mitchell *et al.* (1992) set this threshold at 0.9. Of course, the χ factor is affected by the stoichiometric coefficient of oxygen (ν_o), which lies between 0.5 and 1 and is sometimes difficult to determine accurately.

The Global *n*-th Order Rate Equation

An empirical *n*-th order rate equation is often used to describe kinetics of char oxidation at typical industrial boiler temperatures (Smith, 1982; Hurt and Mitchell, 1992; Monson *et al.*, 1995). The most common form of the *n*-th order rate equation is

$$q_{rxn} = k_s P_{os}{}^n = A\exp(\frac{-E_{obs}}{RT_p})P_{os}{}^n, \tag{2.16}$$

where q_{rxn} is the global char oxidation rate in gram *C* per unit time per unit external surface area, *n* is the apparent reaction order, P_{os} is the oxygen partial pressure at the external surface, *A* is the pre-exponential factor, E_{obs} is the observed activation energy, T_p is the particle temperature in K. This simple equation provides a basis for estimating char oxidation rates, and has often been adequate for practical use at atmospheric pressure over small temperature ranges (Smoot and Smith, 1985). Due to its simplicity, this equation is often used in comprehensive computer models. However, the global *n*-th order rate equation does not explicitly account for pore diffusion effects on kinetics. Pore diffusion effects are implicitly included in the observed activation energy and the pre-exponential factor. One weakness of this equation is that it cannot be extrapolated between Zone I and Zone II. In addition, the reaction order is often observed to vary as experimental conditions vary, with limits of zero and unity (Suuberg, 1988). Presently no theory can satisfactorily explain or predict how the reaction order of char oxidation would change with experimental conditions.

The global *n*-th order rate equation has been criticized for lack of theoretical basis and inadequacy for predicting rates over wide ranges of experimental conditions, especially for high pressure char oxidation modeling (Monson *et al*., 1995; Monson, 1992; Essenhigh, 1996). Monson (1992) conducted about 100 char oxidation experiments using a high pressure drop tube reactor at 1, 5 10, and 15 atm total pressure with 5-21% oxygen in the bulk gas. The particle temperature ranged from 1400 to 2100 K. The pressure dependence of apparent reaction rate coefficients (A and E_{obs}) was significant when assuming an apparent reaction order of 0.5. Variations of activation energies for a given coal as a function of pressure are thought to indicate the inadequacy of the *n*-th order rate equation in correlating these data.

Langmuir-Hinshelwood Kinetics

Fundamental studies show that the carbon-oxygen reaction involves chemisorption, oxygen surface diffusion, and desorption of surface oxygen complexes (Essenhigh, 1981; Essenhigh, 1991; Du *et al.*, 1991). The *n*-th order rate equation fails to reflect the adsorption-desorption nature of this reaction. A more mechanistically meaningful representation of the intrinsic reaction rate is a Langmuir-Hinshelwood form (Laurendeau, 1978; Essenhigh, 1981), which in its simplest form becomes **the Langmuir rate equation**:

$$r_{in}'''(C) = \frac{k_1 C}{1 + KC} \tag{2.17}$$

where k_1 and K are two kinetic parameters. It should be noted that 1) the product of K and C is non-dimensional; 2) there are different possible mechanisms leading to Eq. 2.17; 3) the physical meanings of the two parameters k_1 and K depend on the mechanism leading to Eq. 2.17. The discussion in this study is general and independent of mechanisms. The above equation is also referred to as a "Langmuir adsorption isotherm" (Essenhigh, 1988), a shifting order rate equation (Farrauto and Bartholomew, 1997) and more specifically, a non-dissociative, single-adsorbed-species Langmuir rate equation (Hill, 1977). The Langmuir rate equation can be re-written as:

$$\frac{1}{r_{in}'''} = \frac{1}{k_1 C} + \frac{1}{k_0} \qquad (2.18)$$

where k_0 is the ratio of k_1 to K. The Langmuir rate equation is the simplest form of all Langmuir-Hinshelwood kinetic expressions capable of modeling apparent reaction order shifting between zero and unity.

In an attempt to treat effects of pressure, Essenhigh proposed a so-called "second effectiveness factor" (Essenhigh, 1988) to account for the internal combustion. This method uses some approximations to achieve a simple form of the final rate expression. The second effectiveness factor (ε) was calculated from the power index (α) of the normalized density-diameter relationship (Essenhigh, 1988; Essenhigh and Mescher, 1996; Essenhigh *et al.*, 1999) in the following manner:

$$\varepsilon = 1 + \alpha / 3 \qquad (2.19)$$

$$\frac{\rho}{\rho_o} = \left(\frac{d}{d_o} \right)^{\alpha} \qquad (2.20)$$

The second effectiveness factor approach has several weaknesses: First, the second effectiveness factor approach requires density and diameter data, which are often not available *a priori*, in order to determine the power index α. Hence, this method is not truly predictive in nature. Second, the power index α is very difficult to determine accurately, since it can vary over several orders of magnitude. For example, Essenhigh (1988) reported a value of α around 1 for high temperature char oxidation and values of α in the range of $10^4 \sim 10^5$ for low temperature char oxidation. Third, this approach assumes that the power index α remains constant throughout the whole range of burnout. In a typical pulverized char combustor, the single char particle travels through different zones of the reactor and interacts with different combustion environments, leading to different burning modes (corresponding to α between zero and infinity), and a constant value of α is no longer realistic; hence it is inadequate to account for internal combustion. The original effectiveness factor approach, however, has the potential to overcome all these difficulties associated with the second effectiveness factor approach.

Pore Diffusion and Effectiveness Factor

The effectiveness factor is widely used to account for the intra-particle diffusion effects on kinetics in catalytic pellets and solid fuel particles. The effectiveness factor is defined as the ratio of (a) the reaction rate actually observed, to (b) the reaction rate calculated if the surface reactant concentration persisted throughout the interior of the particle (i.e., no oxidizer concentration gradient within the particle). The reaction rate in a particle can therefore be conveniently expressed by its rate based on surface reactant concentrations multiplied by the effectiveness factor:

$$r'''_{obs}(C_s) = -\frac{dn_C}{V_p dt} = \frac{1}{V_p}(\eta S_{\text{int}} + S_{ext}) r''_{in}(C_s)$$

$$= \frac{S_{\text{int}}}{V_p}(\eta + \frac{S_{ext}}{S_{\text{int}}}) r''_{in}(C_s) = (\eta + \frac{S_{ext}}{S_{\text{int}}}) \frac{S_{\text{int}}}{S_{tot}} \frac{S_{tot}}{V_p} r''_{in}(C_s)$$

$$= (\eta + \frac{S_{ext}}{S_{\text{int}}}) \frac{S_{\text{int}}}{S_{tot}} r'''_{in}(C_s) \qquad (2.21)$$

It is commonly observed that the external surface area is negligible compared to the internal surface area. Therefore the above equation becomes:

$$r'''_{obs}(C_s) = \eta\, r'''_{in}(C_s) \qquad (2.22)$$

The intrinsic char oxidation rate can be represented by an intrinsic *m*-th order rate equation in the form of

$$r'''_{in} = k_m C^m \qquad (2.23)$$

where k_m is the kinetic coefficient in (mol C/m^3)$^{1\text{-m}}$ sec^{-1}, and *m* is the intrinsic reaction order. Correspondingly, the observed reaction rate becomes

$$r'''_{obs} = \eta k_m C_s^{\ m} \qquad (2.24)$$

Alternatively the intrinsic char oxidation rate can be represented by the Langmuir rate equation (Eq. 2.17), and the observed reaction rate becomes:

$$r'''_{obs} = \eta \frac{k_1 C_s}{1 + K C_s} \qquad (2.25)$$

It has been established that the effectiveness factor can be approximately (except that it is exact for first order reactions) predicted by (Bischoff, 1965; Thiele, 1939):

$$\eta = \frac{\tanh(M_T)}{M_T} \quad \text{in Cartesian coordinates} \tag{2.26}$$

$$\eta = \frac{1}{M_T}\left(\frac{1}{\tanh(3M_T)} - \frac{1}{3M_T}\right) \quad \text{in spherical coordinates} \tag{2.27}$$

$$M_T = \frac{L\nu_O r_{in}'''(C_s)}{\sqrt{2}}\left[\int_0^{C_s} D_e(C)\nu_O r_{in}'''(C)dC\right]^{-\frac{1}{2}} \tag{2.28}$$

where L is the characteristic length of the particle (Aris, 1957), which is equal to V_p/S_g, C is the local concentration of oxidizer in the particle, r_{in}''' is the intrinsic molar reaction rate in any form, ν_o is the stoichiometric coefficient of oxygen for each mole of carbon consumed, which converts the carbon consumption rate into oxygen consumption rate, and D_e is the effective diffusivity, which can be a function of oxygen concentration, but is assumed to be spatially uniform (but still allowed to vary temporally) in this study for simplicity. In particular, the general modulus for the m-th order rate equation (Eq. 2.23) becomes (Bischoff, 1965):

$$M_T = L\sqrt{\frac{(m+1)}{2}\frac{\nu_o k_m C_s{}^{m-1}}{D_e}} \tag{2.29}$$

This general modulus has been widely used in the chemical engineering literature (Laurendeau, 1978; Hill, 1977; Bischoff, 1965; Aris, 1975; Carberry, 1976; Fogler, 1992; Froment and Bischoff, 1979; Levenspiel, 1993; Levenspiel, 1999; Mehta and Aris, 1971). For the Langmuir rate equation, a general modulus was obtained in this study by substituting Eq. 2.17 into Eq. 2.28:

$$M_T = L\sqrt{\frac{\nu_o k_1}{2D_e}\frac{KC_s}{1+KC_s}}\,[KC_s - \ln(1+KC_s)]^{-\frac{1}{2}}. \tag{2.30}$$

This is the first time that the general modulus for the Langmuir rate equation has been applied to char oxidation.

Eqs. (2.26) to (2.28) were originally referred to as the general asymptotic solution of the effectiveness factor for general reaction rate forms. As shown in Figure 2.2, by using the general modulus defined in Eq. (2.28), all of the η vs. M_T curves lie within a narrow region, bounded by the first order and zero-th order reactions. The general asymptotic solution uses the known analytical expression for first order reactions (Eq. 2.26 or 2.27) to approximate all other curves, since analytical expressions for these other curves are not known (except for the zero order curve in Cartesian coordinates). The general asymptotic solution, as the name indicates, tends to be accurate when M_T approaches either zero or infinity, where the general asymptotic solution approaches the two asymptotic lines ($\eta = 1$ and $\eta = 1/M_T$). Generally speaking, when M_T is less than 0.2, η can be approximated as unity (this situation is referred to as Zone I in the char combustion literature). When M_T is greater than 5, η can be approximated as $1/M_T$ (this situation is referred to as Zone II; Smoot, 1985). However, the general asymptotic solution is inaccurate in the intermediate range of the general modulus ($0.2 < M_T < 5$), which is recognized by Bischoff (1965). In Cartesian coordinates, the error of the general asymptotic solution can be as high as -24% on a relative basis. It is therefore desirable to eliminate or at least reduce this error. A method to reduce this error was developed in this project, and is described later in the dissertation.

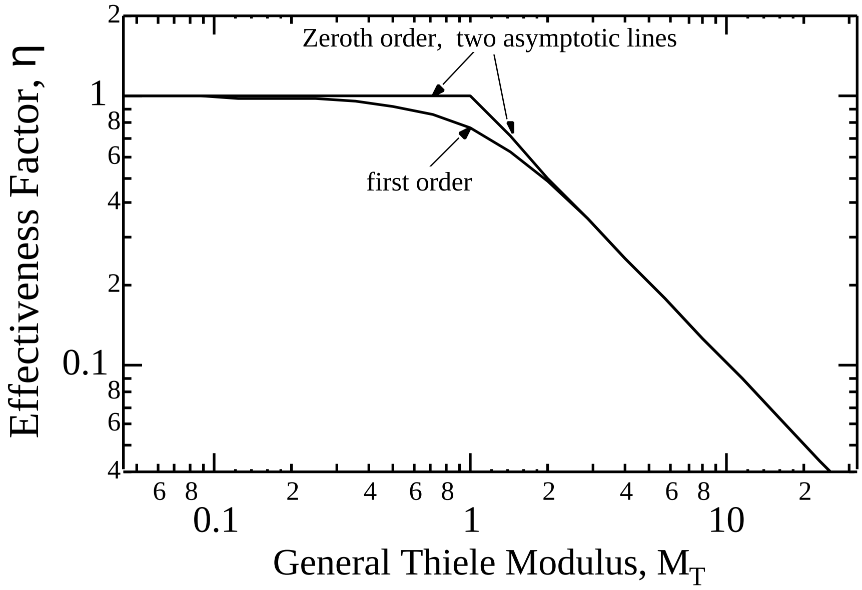

Figure 2.2. The effectiveness factor curves for first order and zero-th order reactions in Cartesian Coordinates. For reactions between zero-th order and first order limits ($0 < m < 1$ or $0 < KC_s < \infty$), the curves lie in the narrow band bounded by the first order and the zeroth order curves.

High Pressure Data in the Literature

A review of published data from high pressure coal combustion and char oxidation experiments is listed in Table 2.1. The experiments by Monson (1992) have been mentioned earlier. The rest of these experiments are discussed briefly below.

Table 2.1. Test Conditions for Various High Pressure Oxidation Rate Measurements

Investigator(s)	Fuel	diameter (μm)	T_p (K)	P_{total}(atm)	x_{O2}(%)
Monson (1992)	chars	63-75	1300-2100	1-15	5~21
Mathias (1996)	coals and chars	Mostly 8000	900-1300	0.86-5	6-18
Ranish and Walker (1993)	graphite	flakes	733-842	1-64	100
Banin *et al*. (1997)	chars	~6	1200-1800	8	0-100
Croiset *et al*. (1996)	chars	90-106	850-1200	2-10	1.5-10
MacNeil and Basu (1998)	chars	417-2000	973-1123	1-7	10-21

Data of Mathias

Mathias (1996) performed oxidation experiments on char particles of mostly 8-mm diameter with a Cantilever Balance Attachment (CBA) in their High Pressure Controlled Profile Reactor (HPCP). The gas temperatures were 825, 1050, and 1200 K (measured by a type-S thermocouple 1.2 cm above the particle). The gas velocities were 0.08, 0.32, and 1.28 m/s. The pressures tested were 0.86, 3.0, and 5.0 atm. Major findings include: 1) An increase in the partial pressure of oxygen had a significant increase on the char oxidation rate on the runs performed at atmospheric pressure; 2) An increase in total pressure while maintaining the same partial pressure of oxygen drastically decreased the oxidation rate; 3) An increase of the total pressure between 0.86 and 5.0 atm while maintaining oxygen mole fraction at 21% produced a small increase in the oxidation rate; 4) Correlating the oxidation rate to the mole fraction of oxygen rather than to the partial pressure of oxygen better described the trends in the experimental data.

Data of Ranish and Walker

Ranish and Walker (1993) studied the oxidation rates of highly crystalline graphite flakes at oxygen pressures between 1-64 atm and temperatures between 733-842 K. The global activation energy (defined as the slope of the log(reaction rate) vs. $1/T_p$ curve, the term “global” arises from the fact that the form of the reaction rate is unknown) for the reaction was found to be 204±4 kJ/mole and was independent of carbon burnout. The intrinsic reaction order decreased from 0.83 to 0.69 as the reaction temperature increased from 733 to 813 K. A mechanism was proposed as:

$$C + 1/2\ O_2 \rightarrow C(O), \qquad (k_a) \tag{R.1}$$

$$C^* + 1/2\ O_2 \rightarrow C(O), \qquad (k_b) \tag{R.2}$$

$$C(O) \rightarrow CO + C^*, \qquad (k_c) \tag{R.3}$$

$$C^* \rightarrow C. \qquad (k_d) \tag{R.4}$$

Reactions (R.1) and (R.2) are not written in rigorous form to make the mathematics more tractable. Although accuracy is lost, the general features are preserved according to the original authors. A nascent site C*, is created during the gasification step (R.3). For simplicity, only CO is considered as a product, and both regular and nascent active sites are assumed to form the same kind of surface oxide. The total active surface is thus comprised of regular bare sites C, nascent bare sites C*, and covered sites C(O). The assumption of steady-state values of these parts of the TASA (Total Active Surface Area) results in an expression for the fraction of covered sites, θ, given below:

$$\theta = \frac{k_d P^{\frac{1}{2}} + k_b P}{k_c k_d / k_a + (k_c + k_d) P^{\frac{1}{2}} + k_b P} \quad . \tag{2.31}$$

The reaction rate equation is then easily obtained:

$$r = \frac{k_c (k_d P^{\frac{1}{2}} + k_b P)}{k_c k_d / k_a + (k_c + k_d) P^{\frac{1}{2}} + k_b P} \quad . \tag{2.32}$$

This equation has four rate constants. Each rate constant has two parameters (*E* and *A*). Thus there are eight adjustable parameters in this rate equation. No values of the rate constants or quantitative examination of this equation were given in their paper.

Data of Banin *et al.*

Banin *et al.* (1997) studied the combustion behavior of pulverized char in drop-tube experiments. The gas temperature was varied between 1200 and 1800 K and the gas pressure was about 8 atm. The oxygen partial pressure was varied between 0.3 and 8 atm. In all cases, 95% of the coal and char particles had diameters less than 6 μm. The apparent reaction order at high oxygen pressure was observed to be as low as 0.3. This could not be explained as Zone I combustion since the char particles were observed to burn with shrinking diameters, and the particle temperatures (1480 ~ 2850 K) were beyond the temperature range where Zone I combustion typically occurs. Zone I corresponds to the complete penetration of oxygen into the particles and a non-shrinking combustion mode. In Zone II, the apparent reaction order can never be less than 0.5, unless the true reaction order is negative (which is unlikely true for carbon-oxygen reaction) assuming the external surface area is negligible compared to the internal surface area.

A "rough sphere" combustion theory was proposed to explain the conflicting observations. When the contribution to reaction rate from the external surface is comparable to that from the internal surface, rough sphere combustion occurs. Rough sphere combustion occurs when reaction rate is controlled by both kinetics and pore diffusion (Zone II), but allows the apparent reaction order to be less than 0.5 due to the contribution from external surface area. However, a microscopic model was used in the original work to account for the spatial and temporal variation of pore structure, which required extensive computational efforts.

Data of Croiset *et al.*

Croiset *et al.* (1996) performed combustion experiments in a fixed-bed reactor at 2, 6, and 10 atm at temperatures between 850 and 1200 K with Westerholt bituminous coal char with diameters in the range of 90-106 μm. The reaction was claimed to be first order in both Zone I and Zone II. The pre-exponential factor, *A*, decreased when the total pressure increased from 2 to 6 atm. Above 6 atm, the effect of total pressure was very weak. High pressure also favored the combustion regime controlled by pore diffusion. Attempts were made to apply the Langmuir rate equation to these data. However, the mole fraction of oxygen was used instead of the oxygen concentration. The theoretical basis behind the selection between the mole fraction and concentration needs to be explored.

The data of Croiset *et al.* were reported in an Arrhenius plot [ln(k) vs. (1/T)] assuming the char/oxygen reaction is first order. The oxygen partial pressures associated with these values of k are required in order to: (1) convert these values of k into reaction rates, and (2) to evaluate other reaction rate forms, such as Langmuir-Hinshelwood rate forms. Unfortunately, these oxygen partial pressures were not reported. Therefore, this set of data was not considered in this project.

Data of MacNeil and Basu

MacNeil and Basu (1998) recently studied the combustion of char under simulated, pressurized, circulating fluidized bed (PCFB) conditions at furnace temperatures between 973 and 1123 K. A quartz wool matrix was used to disperse the char. The experiment was claimed to resemble the fluidized circulating bed conditions in that the voidage was very high. Kinetic rates of char combustion were measured at 1, 3, 5, 7 atm, at oxygen concentrations of 5, 10 and 21%. The surface reaction rates increased with pressure up to 5 atm and further increase of pressure led to decrease of reaction rates. This trend was thought to be consistent with Monson's observation (MacNeil and Basu, 1998). However, re-examination of Monson's data in this study showed that Monson's data at 1, 5, and 10 atm could be unified using a single rate expression, and the data at 15 atm were affected by ignition problems. The observation that the burning rate increased up to 5 atm and decreased beyond this point in Monson's experiments was an artifact and was actually due to the lower wall temperatures and gas temperatures at high pressures.

The unexpected effects of total pressure observed by MacNeil and Basu are difficult to explain and could also be an artifact. Therefore, this set of data was also excluded in this study.

3. Objectives and Approach

The objective of this project was to develop a model that can be used to explain and unify char oxidation rates over wide ranges of experimental conditions (including temperature, total pressure, oxygen mole fraction and particle size) without excessive computational effort. The following elements were to be incorporated into the new model: 1) intrinsic kinetics rather than global kinetics; 2) the Langmuir rate equation rather than the m-th order rate equation; 3) an analytical solution of the effectiveness factor for the Langmuir rate equation with a correction function to improve its accuracy (rather than using a numerical solution or a second effectiveness factor); 4) a pore structure model for calculation of the effective diffusivity, taking into account both Knudsen diffusion and molecular diffusion; and 5) correlations of thermodynamic and transport properties that can be used under both atmospheric and elevated pressures. In addition, modifications were to be made to allow the treatment of char oxidation rates for large particles. (Unlike pulverized char combustion in entrained flow, large particle combustion is often associated with much higher Reynolds numbers.) Once the model was finalized, an optimization program was to be used to adjust the kinetic and pore structure parameters to best fit existing experimental data. Since high-pressure experiments are relatively rare in the literature, and these experiments were conducted on vastly different fuels (from graphite to chars), establishing correlations that could be used for a wide variety of chars was not an objective of this study but rather the task of future work. In this sense, this work was aimed to explain and unify existing experimental data with a set of parameters for each set of experimental data but not to predict the rates *a priori* with a single set of parameters for all sets of data.

As part of the model evaluation, experiments were to be conducted on two South African coals (Koonfontain and Middleburg). The steam and oxygen concentrations during preparation were to be varied to determine the effects on surface area, apparent density, true density, TGA reactivity and high temperature reactivity. The TGA reactivity and high temperature reactivity data were to be used to validate the transition from Zone I to Zone II combustion in the HP-CBK model.

A secondary objective of this work was to explore how the apparent reaction order of char oxidation changes with experimental conditions. Some theoretical challenges in solid combustion, such as the rough sphere combustion phenomenon, were also to be explored.

4. Analytical Solutions of the Effectiveness Factors

Introduction

Pore diffusion effects can be treated with either a full numerical solution radially through the porous char matrix (Reade, 1996), or treated using the analytical Thiele modulus approach (Thiele, 1939). Since the char particle reactivity is often sought for inclusion into a comprehensive model of a coal combustor, an analytical solution is preferred here over the full numerical solution.

It was shown in the literature review that the effectiveness factor can be approximately predicted by the asymptotic solution in spherical coordinates (Thiele, 1939; Bischoff, 1965):

$$\eta = \frac{1}{M_T}\left(\frac{1}{\tanh(3M_T)} - \frac{1}{3M_T}\right) \tag{4.1}$$

where M_T is the general Thiele modulus, which is

$$M_T = L\sqrt{\frac{(m+1)}{2}\frac{\nu_o k_m C_s^{\,m-1}}{D_e}} \tag{4.2}$$

for the *m*-th order rate equation, and

$$M_T = L\sqrt{\frac{\nu_o k_1}{2D_e}}\,\frac{KC_s}{(1+KC_s)}\,[KC_s - \ln(1+KC_s)]^{-\frac{1}{2}} \tag{4.3}$$

for the Langmuir rate equation. It was also shown that the classic asymptotic solution of the effectiveness factor is inaccurate when the general Thiele modulus is in the intermediate range, and the error can be up to 24% in Cartesian coordinates, as shown in

Figure 4.1. The error in reaction rate may be amplified when the reaction rate calculation is coupled with the energy balance. It is therefore necessary to improve the accuracy of the analytical solution of the effectiveness factor.

One may argue that presently the effective diffusivity, D_e, in the M_T expression cannot be determined very accurately, and thus attempts to reduce the errors associated with the general asymptotic solution are unnecessary. However, the inability to accurately determine the effective diffusivity is **a separate problem**. This study shows how to reduce systematic errors associated with the general asymptotic solution.

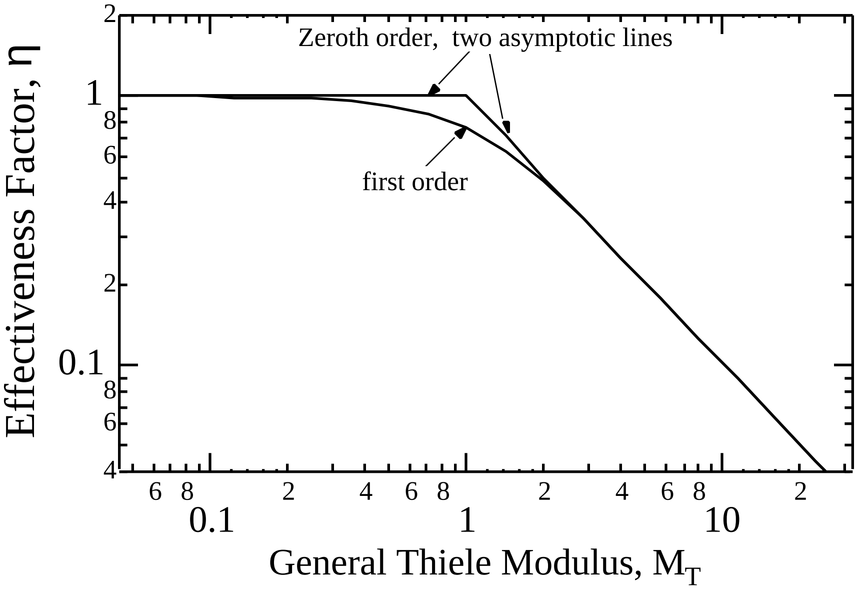

Figure 4.1. The effectiveness factor curves for first order and zeroth order reactions in Cartesian Coordinates. For reactions between zeroth order and first order limits ($0 < m < 1$ or $0 < KC_s < \infty$), the curves lie in the narrow band bounded by the first order and the zeroth order curves.

Task and Methodology

Task

One of the tasks of this aspect of the study was to find a correction function to improve the accuracy of the general asymptotic solution method in the intermediate range of M_T for both the Langmuir and *m*-th order rate equations;

Since catalytic pellets and solid fuel particles usually have shapes that can be approximated more or less by spheres, rather than by semi-infinite flat-slabs or infinite cylinders, this study focuses on analytical and numerical solutions in spherical coordinates. For simplicity, this study is limited to the following conditions:

a) Isothermal conditions (no temperature gradients in the particle).
b) No volume-change resulting from reactions (equi-molar counter-diffusion in the pores of the particle).
c) Irreversible reactions.
d) Two intrinsic reaction rate forms (*m*-th order and Langmuir rate equations).
e) Limits of zero and unity for the reaction order in the *m*-th order rate form.

Numerical Methods

A numerical model of diffusion of oxidizer through the particle interior was developed in order to test the accuracy of the Thiele modulus approaches. The concentration of oxidizer in the particle interior can be described by an ordinary differential equation and two boundary conditions. The generalized steady-state continuity equation in a spherical particle (a catalytic pellet or a solid fuel particle) may be expressed as (Smith, 1981):

$$\frac{d^2C}{dr^2}+\frac{2}{r}\frac{dC}{dr}-\frac{\nu_O r_{in}'''(C)}{D_e}=0 \tag{4.4}$$

where r_{in}''' is the molar carbon consumption rate per unit particle volume as a function of C, D_e is the effective diffusivity, ν_O is the stoichiometric coefficient of oxygen for each mole of carbon consumed in the reaction, C is the local oxygen concentration as a function of r, and r is the radial distance from the origin. The boundary conditions are

$$C = C_s, \text{ at } r = r_s \tag{4.5}$$

and

$$\frac{dC}{dr}=0, \text{ at } r = 0. \tag{4.6}$$

Substituting the Langmuir rate equation into Eq. (4.4) and normalizing the resulting equation lead to:

$$\frac{d^2\theta}{d^2\xi}+\frac{2}{\xi}\frac{d\theta}{d\xi}-\frac{r_s^{\,2}k_1}{D_e}\frac{\theta}{1+KC_s\theta}=0 \tag{4.7}$$

where $\theta = C/C_s$, and $\xi = r/r_s$. If an intermediate modulus is defined as:

$$M_1=\frac{r_s}{3}\sqrt{\frac{k_1}{D_e}}\ . \tag{4.8}$$

Eq. (4.7) can be re-written as:

$$\frac{d^2\theta}{d^2\xi}+\frac{2}{\xi}\frac{d\theta}{d\xi}-9M_1^{\,2}\frac{\theta}{1+KC_s\theta}=0\ . \tag{4.9}$$

By using similar techniques of Patankar (1980) and central differences for first and second order derivatives, Eq. (4.9) is discretized to:

$$a_P\theta_i = a_E\theta_{i+1} + a_W\theta_{i-1} + b\ , \text{ i = 2, 3, 4, …, } N \tag{4.10}$$

where

$$a_E=\frac{1}{\xi(i+1)-\xi(i)}+\frac{1}{\xi(i)}\ , \tag{4.11a}$$

$$a_W=\frac{1}{\xi(i)-\xi(i-1)}-\frac{1}{\xi(i)}\ , \tag{4.11b}$$

$$a_P = a_W + a_E\ , \tag{4.11c}$$

$$b = -9M_1^2 \frac{[\xi(i+1) - \xi(i-1)]}{2} \frac{\theta_i}{1 + KC_s\theta_i} \ , \tag{4.11d}$$

and N + 1 is the number of grid points in the radial coordinate in this model (therefore the spherical particle is divided into N layers). The boundary conditions are:

$$\theta_{n+1} = 1 \, , \tag{4.12a}$$

$$\theta_1 = \theta_2 \ . \tag{4.12b}$$

For m-th order rate equations, the discretization equations are the same as Eq. (4.10) and Eq. (4.11) except that Eq. (4.8) and (4.11d) are replaced by:

$$M_1 = \frac{r_s}{3}\sqrt{\frac{k_m C_s^{\ m-1}}{D_e}} \ , \tag{4.13}$$

$$b = -9M_1^2 \frac{[\xi(i+1) - \xi(i-1)]}{2} \theta_i^{\ m} \ . \tag{4.14}$$

As mentioned previously, in Zone II the effectiveness factor is approximately 1/M_T. Therefore as M_T gets large, only a small fraction (can be roughly estimated as 1/M_T) of the radial particle layers are accessible to oxygen. To maintain the accuracy of the model, the number of layers into which the particle is divided must be increased linearly with M_T. However, when the number of layers is too large, the computation is very slow and the round-off errors may prevent further improvement of accuracy through grid refinement. The number of layers N in the radial coordinate was chosen to be:

$$N = \max\left(150, 150\sqrt{M_T}\right) \ . \tag{4.15}$$

Non-uniform gridding was used, where each layer was given the same volume (V_p/N), in order to reduce numerical errors.

Results and Discussion

Evaluation of the General Asymptotic Solution

Values of the effectiveness factor predicted by the general asymptotic solution using the general moduli in Eqs. (4.2) and (4.3) were compared to the values of η obtained by numerical solution. It was found that in spherical coordinates, the general asymptotic solution predicted the effectiveness factor with errors ranging from -17% to 0% on a relative basis (see Tables 4.1 and 4.2, and Figure 4.2).

At the first order limit, the general asymptotic solution becomes an exact solution, and therefore the accuracy of the numerical solution was evaluated. The first column in Tables 4.1 and 4.2, corresponds to $m = 1$ and therefore represents the relative error between the numerical solution and the exact solution. It can be seen that at the first order limit, the error in the numerical solution for the m-th order model is less than 0.13%. The error in the numerical solution for the Langmuir rate equation is slightly higher (less than 1%). These small numerical errors likely arise due to the gridding scheme; even though the number of grid nodes used in the numerical model increases with M_T (Eq. 4.15), the decrease in effectiveness factor means that the oxidizer penetration depth decreases, and hence only a small fraction of the total number of nodes have non-zero oxygen concentration. The fraction of nodes with non-zero oxygen concentration is approximately proportional to $1/M_T$ when M_T is greater than 5. Therefore, numerical errors as large as 1% were incurred for $KC_s = 0$ and $M_T = 8$.

Table 4.1. The Relative Error* (%) in the General Asymptotic Solution for *m*-th Order Rate Equations Using Eq. (4.2)

m M_T	1.00**	0.75	0.50	0.25	0.00
0.125	0.027	-0.109	-0.290	-0.543	-0.925
0.25	0.046	-0.441	-1.103	-2.058	-3.560
0.5	0.097	-1.316	-3.326	-6.462	-12.375
0.707	0.124	-1.818	-4.630	-9.156	-15.789
1	0.126	-1.963	-4.836	-8.546	-12.014
2	0.053	-1.174	-2.580	-4.177	-5.525
4	0.043	-0.548	-1.224	-1.941	-2.483
8	0.042	-0.260	-0.597	-0.896	-1.375

*Relative error = $(\eta_{asymp} - \eta_{numerical})/\eta_{numerical}$

**$\eta_{asym} = \eta_{exact}$ when $m = 1.0$

Table 4.2. The Relative Error* (%) in the General Asymptotic Solution for the Langmuir Rate Equation Using Eq. (4.3)

$1/(1+KC_s)$ M_T	1.00	0.75	0.50	0.25	0.00
0.125	0.019	-0.162	-0.342	-0.583	-0.925
0.25	0.016	-0.588	-1.282	-2.188	-3.560
0.5	-0.013	-1.639	-3.672	-6.557	-12.375
0.707	-0.076	-2.162	-4.802	-8.618	-16.081
1	-0.215	-2.274	-4.756	-8.000	-12.392
2	-0.491	-1.584	-2.813	-4.277	-6.018
4	-0.679	-1.191	-1.774	-2.472	-3.156
8	-0.933	-1.186	-1.473	-1.821	-2.274

*Relative error = $(\eta_{asymp} - \eta_{numerical})/\eta_{numerical}$

**$\eta_{asym} = \eta_{exact}$ when $1/(1+KC_s) = 1.0$

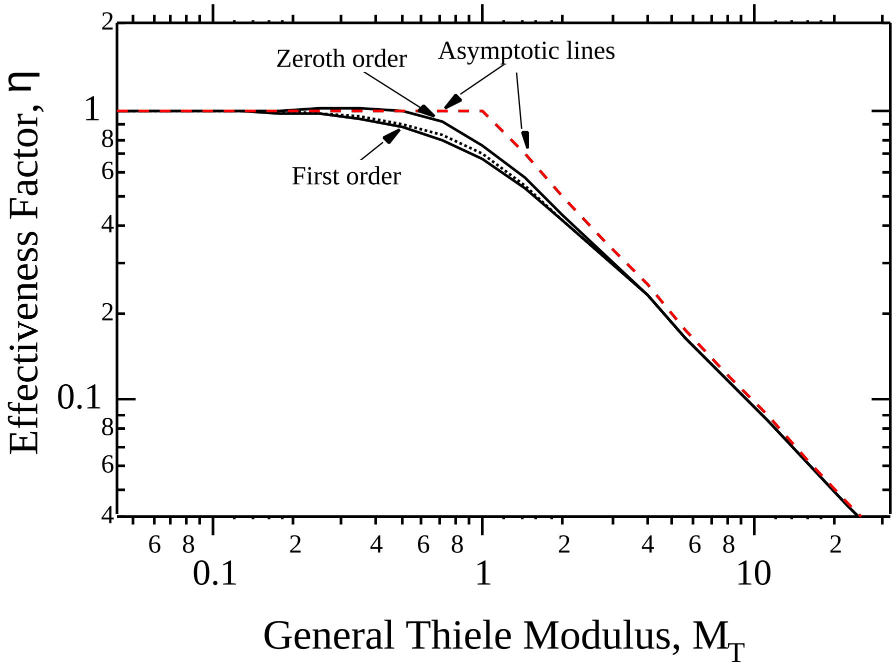

Figure 4.2. Effectiveness factor curves for first order and zeroth order reactions in spherical coordinates. For reactions described by the Langmuir and *m*-th order rate equations, the curves lie in the narrow band bounded by the first order and zero-th order curves. The dotted line in the band corresponds to $m = 0.5$ and corresponds approximately to $KC_s = 1$.

Correction Function

It was shown earlier that in the intermediate range of M_T ($0.2 < M_T < 5$), the general asymptotic solution leads to up to -17% error. The error in reaction rate may be amplified to an unacceptably high level when the reaction rate calculation is coupled with the energy equation. Therefore it is desirable to reduce the error in calculating the effectiveness factor by using an empirical correction function with the general asymptotic solution. Two correction functions were constructed to counter the errors associated with the general asymptotic solutions for (a) *m*-th order rate equations and (b) the Langmuir rate equation, respectively. In order to construct these correction functions, the patterns of error were studied for both the *m*-th order and the Langmuir rate equations.

The resulting observations regarding the patterns of error are shown in Table 4.3. Two observations were made: 1) At a constant value of m or KC_s, the maximum error occurs at about $M_T = \sqrt{1/2}$. Further, as M_T departs from $\sqrt{1/2}$ in a logarithmic scale, the error decreases at approximately the same rate in both directions. That is, if two values of the general modulus (M_{T1} and M_{T2}) satisfy the following relation:

$$\frac{M_{T1}}{\sqrt{1/2}} = \frac{\sqrt{1/2}}{M_{T2}}, \tag{4.16}$$

the error at M_{T1} is approximately equal to the error at M_{T2}. 2) As the observed reaction order (m_{obs}) in Zone I increases to unity, the error decreases monotonically to zero.

In constructing the correction functions, all of the above observations were taken into account. To counter the errors in the whole ranges of M_T (from 0 to ∞) and reaction orders (from 0 to 1), two correction functions were constructed as:

$$f_c(M_T, m) = \left(1 + \frac{\sqrt{1/2}}{2M_T^2 + \frac{1}{2M_T^2}}\right)^{\frac{1}{2}(1-m)^2} \tag{4.17}$$

$$f_c\left(M_T, \frac{1}{1+KC_s}\right) = \left(1 + \frac{\sqrt{1/2}}{2M_T^2 + \frac{1}{2M_T^2}}\right)^{\frac{1}{2}\left(1-\frac{1}{1+KC_s}\right)^2} \tag{4.18}$$

These two correction function can be unified into:

$$f_c(M_T, m_{obs}) = \left(1 + \frac{\sqrt{1/2}}{2M_T^2 + \frac{1}{2M_T^2}}\right)^{\frac{1}{2}(1-m_{obs})^2} \tag{4.19}$$

where $m_{obs} = m$ for m-th order rate equations, and

$m_{obs} = 1/(1+KC_s)$ for Langmuir rate equations.

The physical meaning of m_{obs} is the observed reaction order in Zone I, which will be explained in more detail in the next chapter.

The unified correction function models how all of the various η vs. M_T curves deviate from the η vs. M_T curve for first order reactions in the band shown in Figure 4.2. The correction function is used as a multiplier, f_c, preceding the first order curve expression in the following manner:

$$\eta = f_c \frac{1}{M_T}\left(\frac{1}{\tanh(3M_T)} - \frac{1}{3M_T}\right). \tag{4.20}$$

The $(0.5M_T^{-2} + 2M_T^2)$ part in the correction function needs to be justified. Consider a function $g(M_T) = (0.5M_T^{-2} + 2M_T^2)$. The first and second order derivatives of function g are, respectively,

$$g'(M_T) = -\frac{1}{M_T^{\,3}} + 4M_T \ , \tag{4.21}$$

$$g''(M_T) = \frac{3}{M_T^{\,4}} + 4 \ . \tag{4.22}$$

By setting $g'(M_T)$ to zero and comparing the value of $g''(M_T)$ to zero, it is easy to prove that $g(M_T)$ takes the minimum value at $M_T = \sqrt{1/2}$. As M_T departs from $\sqrt{1/2}$ in both directions, $g(M_T)$ grows rapidly, which decreases the value of f_c toward unity. This guarantees that the correction function would not alter the desirable asymptotic features of the general asymptotic solution. Further, if M_{T1} and M_{T2} satisfy Eq. (4.16), it is easy to prove that $g(M_{T1}) = g(M_{T2})$.

The $(1 - m_s)^2$ part in the power index of the correction function f_c allows a non-linear interpolation between the values of $f_c(M_T, 1)$ and $f_c(M_T, 0)$. In the first order limit, $f_c(M_T, 1) = 1$, since the curve for first order reactions is exact and does not need any correction. The values of functions $g(M_T)$ and $f_c(M_T, m_s)$ are listed in Table 4.4. The correction function is also illustrated in Figure 4.3.

Table 4.3. The Pattern of Error Associated with the General Asymptotic Solution for both Types of Reaction Rate Equations

	m-th Order Rate Equations	Langmuir Rate Equation
General Moduli	$M_T = L\sqrt{\frac{(m+1)}{2}\frac{\nu_o k_m C_s^{\,m-1}}{D_e}}$	$M_T = \frac{r_s}{3}\sqrt{\frac{\nu_o k_1}{2D_e}}\frac{KC_s}{1+KC_s}[KC_s - \ln(1+KC_s)]^{-\frac{1}{2}}$
Patterns of Errors for Predicting the Effectiveness Factor	0% to -17%	0% to -17%
	Very small error at $m = 1$ (Ideally error should be zero)	Very small error at $KC_s = 0$ (Ideally error should be zero)
	Error increases as m decreases to zero at a constant M_T	Error increases as KC_s approaches infinity at a constant M_T
	Error decreases toward zero as M_T departs from 0.707 in both directions at a constant m	Error decreases toward zero as M_T departs from 0.707 in both directions at a constant KC_s
	Maximum error occurs at zeroth order limit at $M_T = 0.707$	Maximum error occurs at zeroth order limit at $M_T = 0.707$

Table 4.4. Values of $g(M_T)$ and $f_c(M_T, m_s)$

M_T	$g(M_T)$	$f_c(M_T, 1)$	$f_c(M_T, 0.75)$	$f_c(M_T, 0.5)$	$f_c(M_T, 0.25)$	$f_c(M_T, 0)$
0.125	32.0	1	1.001	1.003	1.006	1.011
0.250	8.13	1	1.003	1.010	1.024	1.043
0.354	4.25	1	1.005	1.019	1.044	1.079
0.500	2.50	1	1.008	1.032	1.073	1.133
0.707	2.00	1	1.010	1.039	1.089	1.163
1.000	2.50	1	1.008	1.032	1.073	1.133
1.414	4.25	1	1.005	1.019	1.044	1.080
2.000	8.13	1	1.003	1.010	1.024	1.043
4.000	32.0	1	1.001	1.003	1.006	1.011

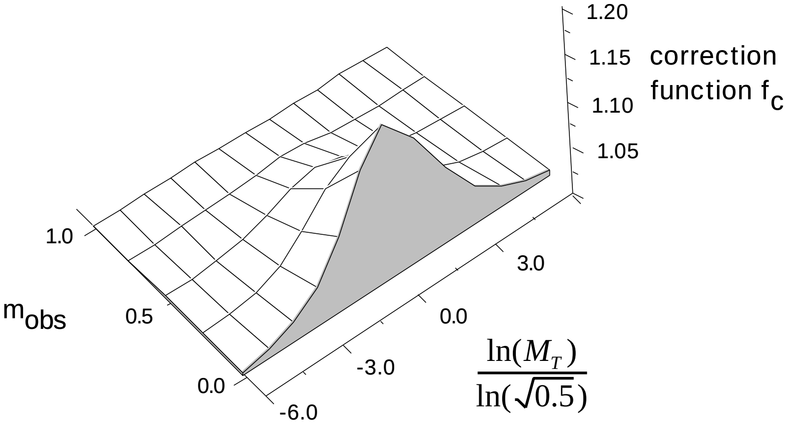

Figure 4.3. The correction function f_c plotted as a function of both the general modulus (M_T) and the observed reaction order in Zone I (m_{obs}).

Accuracy of the Corrected General Asymptotic Solution

The accuracy of the corrected general asymptotic solution (Eq. 4.20) was determined by comparison with the numerical model. As shown in Tables 4.5 and 4.6, the corrected general asymptotic solution predicts the effectiveness factor with errors less than 2% for both the *m*-th order and Langmuir rate equations.

Table 4.5. The Relative Error* (%) in the Corrected General Asymptotic Solution for *m*-th Order Rate Equations

m / M_T	1.00	0.75	0.50	0.25	0.00
0.125	0.027	-0.041	-0.018	-0.069	0.162
0.25	0.046	-0.181	-0.066	0.268	0.549
0.5	0.097	-0.544	-0.269	0.326	-0.754
0.707	0.124	-0.884	-0.952	-1.083	-2.027
1	0.126	-1.197	-1.826	-1.910	-0.345
2	0.053	-0.916	-1.559	-1.901	-1.500
4	0.043	-0.480	-0.954	-1.337	-1.412
8	0.042	-0.243	-0.528	-0.742	-1.104

*Relative error = $(\eta_{asymp} - \eta_{numerical})/\eta_{numerical}$
**$\eta_{asym} = \eta_{exact}$ when m = 1.0

Table 4.6. The Relative Error* (%) in the Corrected General Asymptotic Solution for the Langmuir Rate Equation

$1/(1+KC_s)$ M_T	1.00	0.75	0.50	0.25	0.00
0.125	0.019	-0.030	0.163	0.485	1.133
0.25	0.016	-0.158	0.375	1.354	0.001
0.5	-0.013	-0.729	-0.113	1.208	1.394
0.707	-0.076	-1.161	-0.849	0.128	-1.246
1	-0.215	-1.387	-1.197	0.076	1.374
2	-0.491	-1.178	-1.136	-0.324	0.545
4	-0.679	-1.068	-1.256	-1.243	-1.144
8	-0.933	-1.153	-1.337	-1.494	-1.743

*Relative error = $(\eta_{\mathrm{asymp}} - \eta_{\mathrm{numerical}})/\eta_{\mathrm{numerical}}$
**$\eta_{\mathrm{asym}} = \eta_{\mathrm{exact}}$ when $1/(1+KC_s) = 1.0$

Simplified General Moduli for the Langmuir Rate Equation

The standard general modulus in Eq. (4.3) is complex in form, and encounters division by zero at $KC_s = 0$. However, the value of M_T in Eq. (4.3) exists in the limit at $KC_s = 0$:

$$M_T = L\sqrt{\frac{\nu_o k_1}{D_e}} \,. \tag{4.23}$$

which is the Thiele modulus for first order reactions (Thiele, 1939). Two moduli that have simpler forms were found to closely approximate the standard general modulus in Eq. (4.3). The first one was transformed from a modulus used by Levenspiel (1993):

$$M_T = L\sqrt{\frac{\nu_O k_0 K / D_e}{2KC_s + 1}} = L\sqrt{\frac{\nu_O k_1 / D_e}{2KC_s + 1}} \,. \tag{4.24}$$

The second modulus was constructed to better approximate the standard general modulus in Eq. (4.3) in this study:

$$M_T = L\sqrt{\frac{\nu_O k_0 K / D_e}{2KC_s + \frac{1}{1+KC_s}}} = L\sqrt{\frac{\nu_O k_1 / D_e}{2KC_s + \frac{1}{1+KC_s}}} \tag{4.25}$$

The values of these two simpler general moduli were compared to those of the standard general modulus in Eq. (4.3) in Table 4.7.

Table 4.7. Comparisons Between Simpler M_T expressions (Eq. 4.24 and Eq. 4.25) and the Standard M_T Expression for Langmuir Rate Equation (Eq. 4.3) at Different Values of KC_s

KC_s	$\frac{M_T(Eq.4.24)}{M_T(Eq.4.3)}$	$\frac{M_T(Eq.4.25)}{M_T(Eq.4.3)}$
0.0001	1.000	1.000
0.001	1.000	1.000
0.01	0.997	1.002
0.125	0.967	1.013
0.25	0.946	1.016
0.5	0.922	1.010
0.707	0.912	1.002
1	0.905	0.991
2	0.901	0.968
5	0.917	0.953
10	0.936	0.957
100	0.984	0.986
1000	0.997	0.998
10000	1.000	1.000

It can be seen that the modulus in Eq. (4.24) approximates the standard modulus in Eq. (4.3) with up to 10% error, while the modulus in Eq. (4.25) approximates the standard modulus in Eq. (4.3) within 5%. These simpler moduli do not have the problem of division by zero at $KC_s = 0$. Of more importance, using these simpler and approximate moduli in place of the standard modulus (Eq. 4.3) does not increase the maximum error of the (uncorrected) general asymptotic solution (see Tables 4.8 and 4.9).

Table 4.8. The Relative Error* (%) in the General Asymptotic Solution for the Langmuir Rate Equation Using the Simpler Modulus in Eq. (4.24)

$1/(1+KC_s)$ M_T	1.00^{**}	0.75	0.50	0.25	0.00
0.125	0.019	-0.048	-0.175	-0.417	-0.925
0.25	0.016	-0.155	-0.647	-1.564	-3.560
0.5	-0.013	-0.190	-1.562	-4.530	-12.375
0.707	-0.076	0.216	-1.338	-5.319	-16.081
1	-0.215	1.216	0.383	-3.080	-12.392
2	-0.491	3.691	5.175	3.523	-6.018
4	-0.679	4.887	7.548	6.700	-3.156
8	-0.933	5.234	8.420	7.950	-2.274

*Relative error = $(\eta_{asymp} - \eta_{numerical})/\eta_{numerical}$

**$\eta_{asym} = \eta_{exact}$ when $1/(1+KC_s) = 1.0$

Table 4.9. The Relative Error* (%) in the General Asymptotic Solution for the Langmuir Rate Equation Using the Simpler Modulus in Eq. (4.35)

$1/(1+KC_s)$ M_T	1.00^{**}	0.75	0.50	0.25	0.00
0.125	0.019	-0.190	-0.326	-0.508	-0.925
0.25	0.016	-0.696	-1.219	-1.906	-3.560
0.5	-0.013	-1.995	-3.468	-5.650	-12.375
0.707	-0.076	-2.736	-4.474	-7.162	-16.081
1	-0.215	-3.099	-4.281	-5.861	-12.392
2	-0.491	-2.788	-2.103	-0.966	-6.018
4	-0.679	-2.562	-0.954	1.385	-3.156
8	-0.933	-2.627	-0.610	2.275	-2.274

*Relative error = $(\eta_{asymp} - \eta_{numerical})/\eta_{numerical}$

**$\eta_{asym} = \eta_{exact}$ when $1/(1+KC_s) = 1.0$

The correction function is not intended to be used in conjunction with the empirical and approximate general moduli (Eqs. 4.24 and 4.25) although the combination of the correction function and the simpler modulus in Eq. (4.25) actually gives results with less than 5% error (not shown here).

Summary and Conclusions

The uncorrected and corrected general asymptotic solutions of the effectiveness factors for the m-th order rate equations and the Langmuir rate equation are summarized in Table 4.10. The Thiele modulus approach for treating the effects of diffusion of oxidizer through a porous particle was originally developed for 1st order intrinsic reactions, and later extended to arbitrary reaction rate forms. However, comparisons with detailed numerical models show that the methods generally used for m-th order reactions lead to errors as large as 17% for spherical particles. The Langmuir rate expression, currently being considered for modeling high pressure char reactions, incurred similar errors when pore diffusion effects were treated with the standard approach. These errors arise because an exact expression relating the effectiveness factor (η) to the Thiele modulus (M_T) for first order reaction ($m = 1$) is generally used for all rate forms. Based on the pattern of error, indicating maximum errors at $M_T = 0.707$, a correction function was developed for both the m-th order rate equation and the Langmuir rate equation. This "corrected general asymptotic solution" has a maximum error of 2% over the entire range of M_T (including Zone I, Zone II and especially the transition zone). It uses explicit analytical expressions to predict the effectiveness factor, and therefore is particularly suitable for repeated use in comprehensive computer codes.

Two empirical moduli with simpler mathematical forms were found to be good approximations for the standard general modulus for the Langmuir rate equation. These two moduli avoid the problems with the standard modulus for the Langmuir rate equation (when KC_s approaches zero) without increasing the maximum error of the uncorrected general asymptotic solution. An archival paper has been accepted for publication based upon the work reported in this chapter (Hong *et al.*, 2000a).

Recommendations

The reactions considered in this study are limited to irreversible, isothermal reactions with no volume change. In addition, the Langmuir rate equation is limited to the simplest form. There exist techniques to extend solutions developed for these relatively simple reactions to reversible reactions (Schneider and Mitschka, 1966), reactions with volume change (Bischoff, 1965), and reactions described by more general Langmuir-Hinshelwood forms (Peterson, 1957; Roberts and Satterfield, 1965; Schneider and Mitschka, 1966). The corrected general asymptotic solution of the effectiveness factor (Eq. 4.20) may be applied to other reaction rate forms.

Table 4.10. Summary of the Uncorrected and Corrected General Asymptotic Solutions for Predicting the Effectiveness Factor for *m*-th Order Rate Equations and Langmuir Rate Equations

	m-th Order Rate Equation	Langmuir rate Equation
Rate Equation	$r''' = k_m C^m$	$r''' = \frac{k_1 C}{1+KC}$
Differential Equation and Boundary Conditions	$\frac{d^2C}{dr^2} + \frac{2}{r}\frac{dC}{dr} - \frac{\nu_O k_m C^m}{D_e} = 0$ $C = C_s \ at \ r = r_s$ $dC/dr = 0 \ at \ r = 0$	$\frac{d^2C}{dr^2} + \frac{2}{r}\frac{dC}{dr} - \frac{\nu_O k_1 C}{D_e(1+KC)} = 0$ $C = C_s \ at \ r = r_s$ $dC/dr = 0 \ at \ r = 0$
General Asymptotic Solution (within 17%)	$\eta = \frac{1}{M_T}\left(\frac{1}{\tanh(3M_T)} - \frac{1}{3M_T}\right)$ $M_T = \frac{r_s}{3}\sqrt{\frac{(m+1)}{2}\frac{\nu_O k_m C^{m-1}}{D_e}}$	$\eta = \frac{1}{M_T}\left(\frac{1}{\tanh(3M_T)} - \frac{1}{3M_T}\right)$ $M_T = \frac{r_s}{3}\sqrt{\frac{\nu_O k_1}{2D_e}}\frac{KC_s}{1+KC_s}[KC_s - \ln(1+KC_s)]^{-\frac{1}{2}}$ Two approximate M_T forms: $M_T = \frac{r_s}{3}\sqrt{\frac{\nu_O k_1 / D_e}{2KC_s + \frac{1}{1+KC_s}}}$ or $M_T = \frac{r_s}{3}\sqrt{\frac{\nu_O k_1 / D_e}{2KC_s + 1}}$
Thiele Modulus at First Order Extreme	$M_T = \frac{r_s}{3}\sqrt{\frac{\nu_O k_1}{D_e}}$ when m=1	$M_T = \frac{r_s}{3}\sqrt{\frac{\nu_O k_1}{D_e}}$ when KC_s=0
Thiele Modulus at Zeroth Order Extreme	$M_T = \frac{r_s}{3}\sqrt{\frac{\nu_O k_0}{2D_e C_s}}$ when m=0	$M_T = \frac{r_s}{3}\sqrt{\frac{\nu_O k_0}{2D_e C_s}}$ when KC_s=∞
Corrected General Asymptotic Solution (within 2%)	$\eta = f_c\frac{1}{M_T}\left(\frac{1}{\tanh(3M_T)} - \frac{1}{3M_T}\right)$ $M_T = \frac{r_s}{3}\sqrt{\frac{(m+1)}{2}\frac{\nu_O k_m C^{m-1}}{D_e}}$	$\eta = f_c\frac{1}{M_T}\left(\frac{1}{\tanh(3M_T)} - \frac{1}{3M_T}\right)$ $M_T = \frac{r_s}{3}\sqrt{\frac{\nu_O k_1}{2D_e}}\frac{KC_s}{1+KC_s}[KC_s - \ln(1+KC_s)]^{-\frac{1}{2}}$
Correction Function f_c	$f_c(M_T, m) = \left(1 + \frac{\sqrt{1/2}}{\frac{1}{2M_T^2} + 2M_T^2}\right)^{\frac{1}{2}(1-m)^2}$	$f_c\left(M_T, \frac{1}{1+KC_s}\right) = \left(1 + \frac{\sqrt{1/2}}{\frac{1}{2M_T^2} + 2M_T^2}\right)^{\frac{1}{2}(1-\frac{1}{1+KC_s})^2}$
m_{obs}	m	$\frac{1}{1+KC_s}$

5. Theoretical Developments

The intrinsic reaction order of char oxidation has been observed to vary within limits of zero and unity (Suuberg, 1988; Chan *et al.*, 1987) although the intrinsic reaction order is often observed to be about 0.7 in TGA experiments at atmospheric pressure (Suuberg, 1988; Reade, 1995). No theory has been available to explain or predict how the reaction order changes with experimental conditions. The global *n*-th order rate equation has been under criticism (Essenhigh, 1996) and was shown to be inadequate in modeling high pressure char oxidation. It is generally accepted that the carbon-oxygen reaction involves adsorption of reactant(s), surface reactions, and desorption of products, although the exact reaction mechanism of the carbon-oxygen reaction is still unknown. There is little doubt that an appropriate Langmuir-Hinshelwood expression, with its sound theoretical basis and more adjustable parameters, holds more potential to model char oxidation rates over wide ranges of experimental conditions than the simplistic *n*-th order rate equation. However, a complex Langmuir-Hinshelwood expression with many parameters, which are difficult to determine both experimentally and theoretically, is not a desirable engineering option. Recently, Essenhigh showed that the simple Langmuir rate equation was satisfactory in modeling the carbon-oxygen reaction rate (Essenhigh, 1988; Essenhigh, 1991; Essenhigh, 1994; Essenhigh and Mescher, 1996), although there is still an unresolved question as to a suitable explanation of the empirical *n*-th order rate equation (Essenhigh and Mescher, 1996). It was also recognized (Essehigh and Mescher,

1996) that there is a need for more careful direct investigation on the simple Langmuir rate equation and other rate expressions that are available in the literature (i.e., Temkin, Elovich, Freundlich, and dissociative Langmuir rate expressions; Essenhigh, 1981). This study does not try to theoretically prove or disprove the correctness or applicability of the simple Langmuir equation to the carbon-oxygen reaction rate. Rather, it is assumed in this study that the simple Langmuir rate equation is sufficient for describing the carbon-oxygen reaction rate, and the subsequent theoretical implications are derived.

The Observed Reaction Orders in Zone I and Zone II

It is a common practice to describe the carbon-oxygen reaction with an *m*-th order rate equation:

$$r_{in}''' = k_m C^m \tag{5.1a}$$

where C is the local oxygen concentration at a specific carbon surface. At low temperatures, pore diffusion is fast compared to kinetics, and the oxygen concentration is uniform in the particle (i.e., $C \equiv C_s$). The intrinsic reaction rate can be related to C_s (the oxygen concentration at the external surface of the particle):

$$r_{in}''' = k_m C_s^m \quad \text{in Zone I} \tag{5.1b}$$

Eq. (5.1b) can be re-written as

$$\ln(r_{in}''') = \ln(k_m) + m \ln(C_s) \tag{5.2}$$

From the above equation, it can be seen that a plot of $\ln(r_{in}''')$ vs. $\ln(C_s)$ will yield a straight line, and the slope of this line is the reaction order m. In fact, this is how the order of a reaction is usually determined from experimental data. Eq. (5.2) can be re-written as:

$$m_{obs} = \frac{d\ln[r_{in}'''(C_s)]}{d\ln(C_s)} \tag{5.3}$$

For a reaction described by a Langmuir-Hinshelwood rate equation, there is no reaction order in an explicit sense. However, when a reaction rate form is unknown, it is a common practice to determine the observed kinetic parameters (reaction order, activation energy, and pre-exponential factor) as if the reaction rate were in an *m*-th order rate form. Therefore, Eq. (5.3) can be used as a general definition of the **observed reaction order in Zone I (m_{obs})** for all reaction rate forms.

Substitution of the Langmuir rate equation (Eq. 2.17) into Eq. (5.3) gives

$$m_{obs} = \frac{d\ln\left(\frac{k_1 C_s}{1+KC_s}\right)}{d\ln(C_s)} = \frac{1}{1+KC_s}\,. \tag{5.4}$$

Note that for a Langmuir type reaction the ln(r_{in}''') vs. ln(C_s) curve is not a straight line. The slope of the curve (which is the reaction order) is dependent on the oxygen concentration and the particle temperature since K is a function of temperature.

Similarly, the **observed reaction order in Zone II (n_{obs})** can be defined as:

$$n_{obs} = \frac{d\ln[r_{obs}'''(C_s)]}{d\ln(C_s)} \tag{5.5}$$

If it is further assumed that the external surface area is negligible compared to the internal surface area, the observed reaction order in Zone II becomes (see Eq. 2.21):

$$n_{obs} = \frac{d\ln[\eta r_{in}'''(C_s)]}{d\ln(C_s)} \tag{5.6}$$

Consider a reaction described by an *m*-th order rate equation. In Zone II, the effectiveness factor is $1/M_T$, and the observed reaction rate is:

$$r'''_{obs} = \frac{1}{M_T} k_m {C_s}^m = \frac{1}{L\sqrt{\frac{(m+1)}{2}\frac{k_m {C_s}^{m-1}}{D_e}}} k_m {C_s}^m \tag{5.7}$$

Substitution of Eq. (5.7) into Eq. (5.5) gives,

$$n_{obs} = \frac{(m+1)}{2} \tag{5.8}$$

This is a classical relationship in kinetics literature (Smith, 1981). Now consider a reaction described by the Langmuir rate equation. In Zone II, the observed reaction rate is:

$$r'''_{obs} = \frac{\eta k_1 C_s}{1+KC_s} = \frac{1}{M_T}\frac{k_1 C_s}{1+KC_s} \tag{5.9}$$

In the previous chapter it has been shown that the standard general modulus for Langmuir rate equation is:

$$M_T = L\sqrt{\frac{\nu_o k_1}{2D_e}}\frac{KC_s}{1+KC_s}[KC_s - \ln(1+KC_s)]^{-\frac{1}{2}}. \tag{5.10}$$

And this standard general modulus can be approximated by

$$M_T = L\sqrt{\frac{\nu_O k_0 K/D_e}{2KC_s + \frac{1}{1+KC_s}}} = L\sqrt{\frac{\nu_O k_1/D_e}{2KC_s + \frac{1}{1+KC_s}}} \tag{5.11}$$

or

$$M_T = L\sqrt{\frac{\nu_O k_0 K/D_e}{2KC_s+1}} = L\sqrt{\frac{\nu_O k_1/D_e}{2KC_s+1}}. \tag{5.12}$$

The observed reaction order was obtained from Eqs. (5.10), (5.9), and (5.5) after tedious mathematical manipulations:

$$n_{obs} = \frac{1}{2}\frac{(KC_s)^2}{[KC_s - \ln(1+KC_s)]}\frac{1}{(1+KC_s)} \quad (5.13)$$

It can be seen that the observed reaction order in Zone II (n_{obs}) for the Langmuir rate equation is a complex function of a non-dimensional number KC_s. An important implication of Eq. (5.13) is that the value of n_{obs} ranges from 0.5 to 1 (see Table 5.1), just like the range of n_{obs} in Eq. (5.8), as shown in Figure 5.1. That is, in Zone II the observed reaction order (n_{obs}) cannot be less than 0.5 if the reaction is sufficiently described by the Langmuir rate equation, assuming the reaction rate contributed from the external surface area of the particle is negligible compared to that from the internal surface area. Similarly, the observed reaction order can be **estimated** from Eqs. (5.11), (5.9) and (5.5):

$$n_{obs} = \frac{1}{1+KC_s} + \frac{KC_s}{2KC_s + \frac{1}{1+KC_s}}[1 - \frac{1}{2(1+KC_s)^2}] \quad (5.14)$$

or from Eqs. (5.12), (5.9) and (5.5):

$$n_{obs} = \frac{1}{1+KC_s} + \frac{KC_s}{2KC_s + 1} \quad (5.15)$$

Table 5.1. The values of n_{obs} at different values of KC_s based on the standard general modulus and simpler general moduli

KC_s	0	0.125	0.25	1	4	16	64	∞
n_{obs} from (5.13)	1.00 *	0.962	0.931	0.815	0.669	0.572	0.527	0.500
n_{obs} from (5.14)	1.00	0.955	0.931	0.850	0.678	0.557	0.515	0.500
n_{obs} from (5.15)	1.00	0.989	0.967	0.833	0.644	0.544	0.512	0.500

* Note: Zero divided by zero situation. Value exists only in the limit.

The theory developed above provides a new way to estimate the kinetic parameter K in the Langmuir rate equation. By measuring the observed reaction order in

Zone I or Zone II at different oxygen concentrations, the kinetics parameter *K* in the Langmuir rate equation may be estimated.

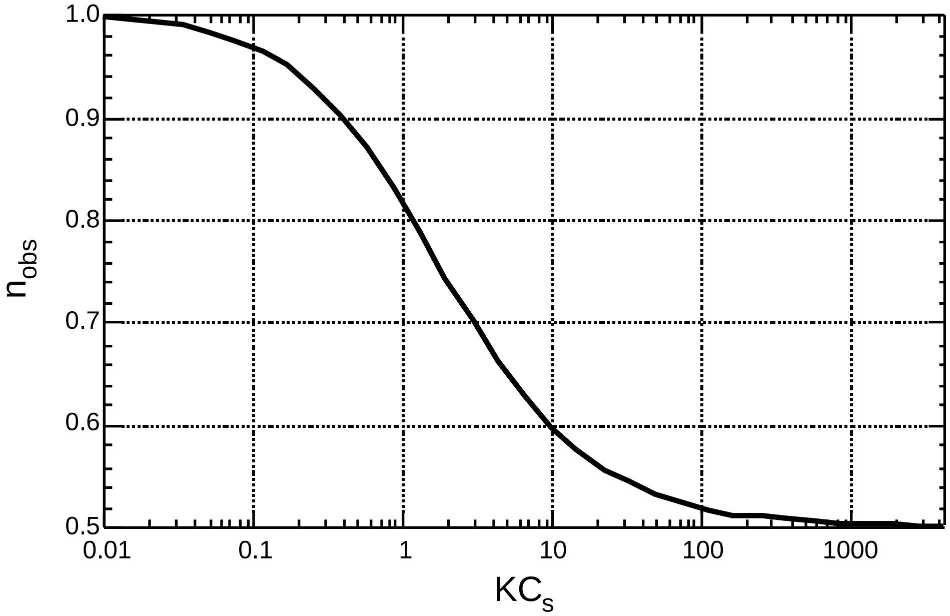

Figure 5.1. The relationship between KC_s and the observed reaction order (n_{obs}) as predicted by Eq. (5.13).

Rough Sphere Combustion

It is commonly assumed that the external surface area is negligible compared to the internal surface area. This assumption is usually valid since the internal surface area of a char particle is usually much larger than the external surface area. However, the external surface can play a role under some conditions and the rough sphere combustion phenomenon occurs. In rough sphere combustion, the reaction rate contributed from the external surface area can no longer be neglected. The observed rate corresponding to the Langmuir rate equation is (see Eq. 2.21)

$$r'''_{obs} = (\eta + \frac{S_{ext}}{S_{\text{int}}})\frac{S_{\text{int}}}{S_{tot}}\frac{k_1 C_s}{1 + KC_s} . \qquad (5.16)$$

The observed reaction order in Zone II can be less than 0.5 for rough sphere combustion due to combustion on the external surface. The effects of the external surface on the observed reaction order can be seen by substituting Eq.5.16 into Eq. 5.5. Although Eq. 5.16 was developed to explain the rough sphere combustion phenomenon, it can be used in general for porous solid combustion. However, in most cases (which are not rough sphere cases), the S_{ext}/S_{int} term in Eq. 5.16 is negligible compared to the effectiveness factor η, and the S_{int}/S_{tot} term can be well approximated by unity. In other words, Eq. 5.16 reduces to Eq. 2.25 in most cases.

Similarly, the observed rate corresponding to the *m*-th order rate equation is

$$r'''_{obs} = (\eta + \frac{S_{ext}}{S_{\text{int}}})\frac{S_{\text{int}}}{S_{tot}} k_m C_s^{\ m} . \tag{5.17}$$

The conditions favoring the rough sphere combustion are explored here. In order for rough sphere combustion to occur, S_{ext}/S_{int} must be of the order of the effectiveness factor η (see Eqs. 5.16 and 5.17). In other words, the ratio of external rate to the internal rate ($S_{ext}/S_{int}\eta$) must not be negligibly small. Note that the external surface area is proportional to $d_p^{\ 2}$, the internal surface area is proportional to $d_p^{\ 3}$ (since $S_{int} = m_p S_m = V_p \rho_p S_m$), while the effectiveness factor in Zone II is inversely proportional to d_p (see Chapter 4). Consequently, the ratio of the external rate to the internal rate ($S_{ext}/S_{int}\eta$) is independent of size. Therefore particle size is not a factor that favors rough sphere combustion. However, small particle size helps to avoid Zone III combustion and hence allows the observation of the rough sphere combustion phenomenon. Strictly speaking, Zone III combustion is rough sphere combustion (since external combustion cannot be neglected in Zone III), but does not allow the rough sphere phenomenon to be observed.

Factors that reduce the value of $S_{int}\eta$ would favor the occurrence of rough sphere combustion. These factors include:

1) Small specific surface area (typically in highly ordered carbon).

2) Factors that reduce the effective diffusivity D_e in the generalized Thiele modulus (pore constriction, blind pore and low porosity) and hence reduce the effectiveness factor.

3) Very fast kinetics, which increases the value of the general Thiele modulus and hence reduces the effectiveness factor.

Small pore size in char particles seems to fall into the second category (factors that reduce the effective diffusivity). However, small pore size is typically associated with large specific internal surface area, since for cylindrical pores the pore radius is inversely proportional to the internal surface ($r_p = 2\varepsilon V_p/S_{int}$; Smith, 1981). These two effects cancel out and therefore small pore size is not a factor that favors rough sphere combustion.

It is important to distinguish the external surface area ($\Omega\pi d^2$) from the geometric external surface area, which is simply πd^2 for spherical particles. The roughness factor Ω, accounts not only for the apparent geometric distortions from a smooth and spherical shape but also penetration of oxygen molecules within a pore before the first collision with the pore wall, which determines the Knudsen diffusion coefficient (Banin *et al.*, 1997).

Bulk Diffusion vs. Knudsen Diffusion

During the course of this study, Sun and Hurt (1999) incorporated the effectiveness factor into CBK to account for Zone I/II transition. However, *m*-th order kinetics was still used to describe the carbon-oxygen reaction and the reaction order is somewhat arbitrarily assumed to be 0.5, implying an apparent reaction order of 0.75. Transport to the particle interior was believed to occur primarily through large feeder pores in which diffusion occurs in or near molecular regime (Simons, 1983). The transport limitations to the interior through large feeder pores were the primary interest of Sun and Hurt (1999) and are described explicitly to predict the influence of particle diameter on overall rate as these transport limitation occurs over the whole particle length scale. It was believed that the effects of diffusion limitations in micropores could be absorbed into the intrinsic surface rate coefficient (Galavas, 1980). With these simplifying assumptions, the effective diffusivity for transport to the particle interior is modeled as:

$$D_e = D_{AB}\varepsilon\ f_M / \tau \tag{5.18}$$

where f_M is the fraction of the total porosity in feeder pores (that is $\varepsilon_M = f_M\varepsilon$), and f_M/τ can be treated as a single empirical parameter. This method may be sufficient for char oxidation at atmospheric pressure, but the disadvantage of this method is obvious for modeling char oxidation over wide range of total pressure: the molecular diffusivity is inversely proportional to total pressure, while Knudsen diffusivity is independent of total pressure, therefore molecular diffusion becomes more important as total pressure increases. In addition, absorbing the effects of transport limitations in micropores into the surface rate coefficient may produce "apparent" kinetics, just as absorbing the effects of internal combustion into the global *n*-th order rate coefficient k_s (see Eq. 2.16) does.

In contrast to the approach of Sun and Hurt (1999), Charpenay *et al.* (1992) neglected the molecular diffusion mechanism and used only the Knudsen diffusivity to calculate the effective diffusivity:

$$D_e = D_K \varepsilon / \tau \tag{5.19}$$

Although both groups used the tortuosity factor to convert the diffusivity into effective diffusivity, the selections of diffusion mechanism seemed somewhat arbitrary. In this study the relative importances of these two diffusion mechanisms were compared, and the situations where one of these mechanism may be neglected were explored.

In general, both bulk diffusion (also called molecular diffusion) and Knudsen diffusion may contribute to the mass transport rate within the porous structure of the char. The combined effects of these two diffusion mechanisms can be described by the combined diffusivity D (Smith, 1981):

$$D = \frac{1}{1/D_{AB} + 1/D_K} \tag{5.20}$$

The combined diffusivity can be controlled by molecular diffusion, Knudsen diffusion or both of them, depending on the ratio of the size of pore to the mean free path (Knudsen, 1950). The Knudsen diffusivity can be calculated from classical kinetic theory (Smith, 1981):

$$D_K = 9.70 \times 10^3 r_p \left(\frac{T_p}{M_A} \right)^{1/2} \tag{5.21}$$

where D_K is in cm^2/sec, r_p is the pore radius in cm, T_p is in K, and M_A is the molecular weight of oxygen. The bulk diffusivity can be calculated using a correlation by Mitchell (1980):

$$D_{O2/N2} = 1.523 \times 10^{-5} T_p^{1.67} / P \tag{5.22}$$

This correlation was derived from the Chapman-Enskog formula (Bird *et al.*, 1960; Mitchell, 1980), and is used for convenience.

When $1/D_{O2,N2} >> 1/D_K$, the sum in Eq. (5.20) will be virtually determined by $1/D_{O2,N2}$, and the Knudsen diffusion has virtually no effects on the combined diffusivity. Similarly, when $1/D_{O2,N2} << 1/D_K$, the Knudsen diffusion dominates and the molecular diffusion can be neglected. A **critical pore radius,** $r_{p,crit}$, is proposed in this study to facilitate determination of the relative importances of Knudsen and molecular diffusion. A **critical pore radius** is defined as the pore radius that makes $1/D_{O2,N2}$ exactly the same as $1/D_K$:

$$9.7 \times 10^{-5} r_{p,crit} \left(\frac{T_p}{32} \right)^{1/2} = D_K = D_{O2,N2} = 1.523 \times 10^{-8} T_p^{1.67} / P \tag{5.23}$$

Rearranging the above equation gives

$$r_{p,crit} = \frac{1.523 \times 10^{-5} \sqrt{32}}{9.7 \times 10^{-5}} T_p^{1.17} / P = 0.888 T_p^{1.17} / P \qquad (\text{Å}) \tag{5.24}$$

where $r_{p,crit}$ is in Å, T_p is in K, and P is in atm.

The critical pore radius is a function of temperature and gas pressure, and it is an important parameter in pore diffusion. When the pore radius is at least 20 times the critical pore radius, $(1/D_{O2N2})$ is at least 20 times $(1/D_K)$, and the sum of $(1/D_{O2N2})$ and $(1/D_K)$ can be approximated by $(1/D_{O2N2})$ with less than 5% error. Similarly, when the pore radius is less than 1/20 of the critical pore radius, the combined diffusivity can be approximated by the Knudsen diffusion within 5%. In summary, the diffusivity of oxygen in a pore with a radius r_p is:

$$D = D_{O2,N2}, \text{ when } r_p \geq 20r_{p,crit}$$

$$D = D_K, \text{ when } r_p \leq r_{p,crit}/20$$

$$D = 1/(1/D_{O2,N2} + 1/D_K), \text{ when } r_{p,crit}/20 \leq \mathrm{r_p} \leq 20r_{p,crit}.$$

The values of the critical pore radius were computed and shown in Table 5.2.

Table 5.2. The Values of Critical Pore Radius (Å) at Different Temperatures and Gas Pressures.

P (atm) / T_p (K)	1	5	10	15
1000	2874	575	287	192
1250	3731	746	373	249
1500	4618	924	462	308
1750	5531	1106	553	369

For example, at 1500 K and 1 atm, the critical pore radius is 4618 Å, the Knudsen diffusion cannot be neglected unless the pore radius of the char is greater than 20 × 4618 = 92360 Å = 9.236 μm. Similarly, at 1500 K and 1 atm, the molecular diffusion should not be neglected unless the pore radius is less than 4618 / 20 = 231 Å (0.023 μm). Eq. 5.20 is generally applicable and is therefore recommended.

Another way to tell whether Knudsen diffusion or molecular diffusion is important is to compare the pore radius to the mean free path of oxygen. Note that the critical pore radius is slightly different from the mean free path of oxygen molecules. According to classic kinetic theory (Bird *et al.*, 1960), the mean free path of oxygen is:

$$\lambda = \frac{1}{\sqrt{2}\pi d^2 NC} = \frac{1}{\sqrt{2}\pi N}\frac{RT_p}{P}\frac{1}{d^2} = 2.60\frac{T_p}{P} \quad (\text{Å}) \qquad (5.25)$$

where T_p is in K, P is in atm. The mean free path of oxygen is 3900 Å at temperature of 1500 K and pressure of 1 atm, slightly lower than the critical pore radius (4618 Å).

Relationship between the Effectiveness Factor and the Second Effectiveness Factor

The second effectiveness factor, according to Essenhigh (1988), is defined as

$$\varepsilon = 1 + \frac{R_{\mathrm{int}}}{R_{ext}} \tag{5.26}$$

where R_{int} and R_{ext} are internal and external reaction rates, respectively. Both R_{int} and R_{ext} are mass carbon consumption rates per unit geometric external surface area. The second effectiveness factor is calculated from the power index of the normalized density-diameter relationship:

$$\varepsilon = 1 + \alpha / 3 \tag{5.27}$$

$$\frac{\rho}{\rho_o} = \left(\frac{d}{d_o} \right)^{\alpha} \tag{5.28}$$

Comparison between Eqs. (5.27) and (5.26) gives

$$\frac{R_{\mathrm{int}}}{R_{ext}} = \frac{\alpha}{3} \tag{5.29}$$

The ratio of the internal rate to the external rate, according to the definition of the effectiveness factor, can be expressed as:

$$\frac{R_{\mathrm{int}}}{R_{ext}} = \frac{\eta S_{\mathrm{int}}}{S_{ext}} \tag{5.30}$$

If both the effectiveness factor approach and the second effectiveness factor approach are correct, they should predict the same value for R_{int}/R_{ext}. Therefore, Eqs. (5.29) and (5.30) can be used to bridge the effectiveness factor approach and the second effectiveness factor approach:

$$\frac{\alpha}{3} = \frac{\eta S_{\mathrm{int}}}{S_{ext}} \tag{5.31}$$

This relation is illustrative of how the value of α changes from Zone I to Zone II. In Zone I, η is unity, and $\alpha = 3S_{int}/S_{ext}$. S_{int}/S_{ext} is usually a large number, which gives α a large value, consistent with the values (10^4 ~10^5) reported by Essenhigh (1988). In Zone II, η could be a very small value, which could possibly bring α down to a value around 2 or 3 (Essenhigh, 1988). However, in order for α to be a small value, η has to be extremely small.

The above relation should be considered qualitative rather than quantitative since careful examination showed that the derivation of the second effectiveness factor might be based on some problematic assumptions, which are detailed as follows:

The mass change of a char particle can be written as:

$$\frac{-1}{S_g}\frac{dm}{dt} = \frac{-1}{\pi d^2}\frac{d\left(\frac{1}{6}\pi d^3 \rho\right)}{dt} = -\frac{d}{6}\left(\frac{\partial \rho}{\partial t}\right)_d - \frac{\rho}{2}\left(\frac{\partial d}{\partial t}\right)_\rho \tag{5.32}$$

Essenhigh went a step further to assume that the density change is solely due to the internal combustion, and the diameter change is solely due to the external combustion:

$$R_{\mathrm{int}} = -\frac{d}{6}\left(\frac{\partial \rho}{\partial t}\right)_d \tag{5.33}$$

$$R_{ext} = -\frac{\rho}{2}\left(\frac{\partial d}{\partial t}\right)_\rho \tag{5.34}$$

Both of these assumptions are arguable. Even if there were no reaction occurring on the external surface, the particle diameter would shrink under Zone II conditions. Due to the non-uniform distribution of oxygen concentration in the particle, the carbon consumption rate is higher near the pore mouth (but still inside a pore) than the rate deep into the pore. When pores overlap near the pore mouth, the particle diameter will shrink. Figure 5.2 illustrates how the internal combustion could decrease the particle diameter.

Mitchell *et al.* (1992) recognized that the value of the burning mode parameter (α_m) is not a quantitative estimate of the amount of internal reaction, as fragmentation and carbon densification (Hurt *et al.*, 1988) also influence the evolution of diameter and density. The burning mode parameter α_m used by Mitchell *et al.* is defined as:

$$\frac{\rho_c}{\rho_{c,o}} = \left(\frac{m_c}{m_{c,o}}\right)^{\alpha_m} \tag{5.35}$$

Note that the power index α defined in Eq. 5.28 is closely related to the burning mode parameter α_m.

In summary, the second effectiveness factor approach suffers the following problems as well as other problems mentioned in the literature review:

1. It is based on the arguable assumptions that the diameter decreases only due to external combustion and the density decreases only due to internal combustion.
2. The second effectiveness factor approach is adversely affected by other phenomena such as fragmentation and carbon densification.

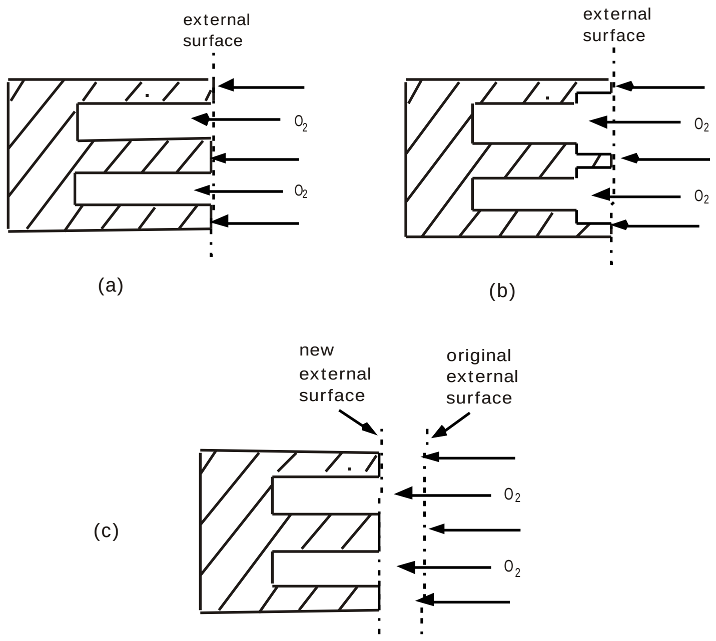

Figure 5.2. Illustration of how internal combustion can decrease the particle diameter. Oxygen penetrates only part of the pore length, and its concentration is higher near the pore mouth, therefore combustion rate is higher near the pore mouth. Actual pore shape may open toward the mouth gradually and the reaction front moves toward the particle center continuously. This figure is for illustration purposes only.

Extended Resistance Equation (ERE)

Essenhigh (1988) proposed a so-called "Extended Resistance Equation" (ERE) to represent the char oxidation rate. In this section it will be shown that the ERE is invalid except for a few special cases. Following Essenhigh's adsorption-desorption terminology and derivations, the reaction rate from the kinetics is

$$\frac{1}{r''_{obs}} = \frac{1}{\varepsilon k_a P_{os}} + \frac{1}{\varepsilon k_d} \tag{5.36}$$

From the boundary layer diffusion, the reaction rate is

$$r''_{obs} = k_D (P_{og} - P_{os}) \tag{5.37}$$

Combining Eq. (5.36) and (5.37) and eliminating P_{os} lead to a reaction rate equation in a quadratic form:

$$r''^{\,2}_{obs} - [k_D P_{og} + \varepsilon k_d + k_D k_d / k_a] r''_{obs} + (\varepsilon k_d)(k_D P_{og}) = 0 \qquad (5.38)$$

or
$$r''^{\,2}_{obs} - P r''_{obs} + Q = 0 \qquad (5.39)$$

where $P = (k_D P_{og} + \varepsilon k_d + k_D k_d / k_a)$ and $Q = (\varepsilon k_d)(k_D P_{og})$. The solution of this quadratic equation is

$$r''_{obs} = (1/2) P [1 - (1 - 4Q / P^2)^{1/2}] \qquad (5.40)$$

In order to obtain a simple form, Essenhigh went a step further and approximated the above equation by

$$r''_{obs} = Q / P \qquad (5.41)$$

Substituting Q and P back into Eq. (5.41) gives

$$\frac{1}{r''_{obs}} = \frac{1}{\varepsilon k_a P_{og}} + \frac{1}{\varepsilon k_d} + \frac{1}{k_D P_{og}} \qquad (5.42)$$

This is the "Extended Resistance Equation" (ERE) developed by Essenhigh (1988). Comparing Eq. 5.41 with Eq. 5.40 leads to

$$(1\text{-}4Q/P^2)^{1/2} = (1\text{-}\ 2Q/P^2) \qquad (5.43)$$

This is to say, the above relation was assumed by Essenhigh in simplifying Eq. 5.40 into Eq. 5.41. Eq. 5.43 can be re-written as:

$$(1\text{-}4Q/P^2) = (1\text{-}\ 2Q/P^2)^2 \qquad (5.44)$$

Let $x = 2Q/P^2$, and the above equation becomes

$$(1\text{-}2x) = (1\text{-}\ 2x + x^2) \qquad (5.45)$$

The above equation (and hence the ERE) is valid **only if**

$$2Q/P^2 = x << 1. \qquad (5.46)$$

Let's now examine what Eq. 5.46 implies. Substituting P and Q into Eq. 5.46 yields

$$\frac{2}{\left(\frac{1}{\varepsilon k_a P_{og}}+\frac{1}{\varepsilon k_d}+\frac{1}{k_D P_{og}}\right)^2 \varepsilon k_d k_D P_{og}} << 1 \tag{5.47}$$

Substituting Eq. (5.42) into Inequality (5.47) gives

$$2\left(\frac{r''_{obs}}{\varepsilon k_d}\right)\left(\frac{r''_{obs}}{k_D P_{og}}\right) << 1 \tag{5.48}$$

This means that either $r''_{obs}/\varepsilon k_d << 1$ or $r''_{obs}/k_D P_{og} << 1$ (or both) must be true in order for the ERE to be valid. In other words, in order to use the ERE, the resistance of either the boundary layer diffusion or the desorption process or both must be negligible compared to the total resistance (including adsorption, desorption and film diffusion). In many cases, both the boundary layer diffusion and the desorption process are important, and hence the use of the ERE would lead to great errors. Generally speaking, the ERE is applicable for only a few special cases.

Various Mechanisms for the Carbon-Oxygen Reaction

The mechanism of the carbon-oxygen reaction has been under investigation for decades but is by no means well understood. Different mechanisms have been proposed to describe the carbon-oxygen reaction rate. Some of these mechanisms were reviewed by Walker *et al.* (1959), Laurendeau (1978), Essenhigh (1981) and Walker *et al.* (1991).

It is generally accepted that the carbon-oxygen reaction involves adsorption of reactant(s), surface reactions, and desorption of products (Blyholder and Eyring, 1959; Laurendeau, 1978; Ahmed *et al.*, 1987; Essenhigh, 1988; Essenhigh, 1991; Du *et al.*, 1991). The chemisorption step has been determined to be first order with respect to the oxygen partial pressure (Suuberg *et al.*, 1988; Essenhigh, 1991) while the desorption step is independent of oxygen partial pressure (Essenhigh, 1991; Croiset *et al.*, 1996).

Different mechanisms led to different rate expressions. These rate expressions can be classified into two types: simple Langmuir rate equation and complex Langmuir-Hinshelwood rate expressions. The simple Langmuir rate equation has the form of

$$r_{in}''' = \frac{k_1 C}{1 + KC} \tag{5.49}$$

or equivalently,

$$\frac{1}{r_{in}'''} = \frac{1}{k_1 C} + \frac{1}{k_0} \tag{5.50}$$

The simple Langmuir rate equation requires four rate coefficients (2 pre-exponential factors and 2 activation energies). Notice that the global *n*-th order rate equation requires 3 rate coefficients (n, A, and E_{obs}). The Langmuir-Hinshelwood rate expressions are more complex (with more terms in the denominator or numerator) than the simple Langmuir rate equation. Complex Langmuir-Hinshelwood rate expressions are less desirable in engineering practice since these rate expressions require more constants, most of which are difficult to determine theoretically or experimentally. For example, Laurendeau (1978) proposed a mechanism that utilizes 10 constants (5 pre-exponential factors and 5 activation energies), and Ranish and Walker (1993) proposed a mechanism that utilizes 8 constants (4 pre-exponential factors and 4 activation energies). In the long run, complex Langmuir-Hinshelwood expression might become a viable option with experimental and theoretical developments on this reaction, but presently the simple Langmuir rate equation seems to be a better option due to its simplicity.

Laurendeau (1978) assumed steady-state for the adsorption-desorption sequence and obtained the simple, non-dissociative Langmuir rate equation (SNDL):

$$r_a'' = k_a C(1-\theta) \tag{5.51}$$

$$r_d'' = k_d \theta \tag{5.52}$$

Assuming quasi-steady state leads to:

$$r_a'' = r_d'' \tag{5.53}$$

Substituting Eqs (5.51) and (5.52) into Eq. (5.53) leads to:

$$\theta = \frac{KC}{1+KC} \tag{5.54}$$

where $K = k_a/k_d$. Substituting Eq. (5.54) into Eq. (5.52) gives:

$$r'' = \frac{k_d KC}{1+KC} = \frac{k_a C}{1+KC} \tag{5.55}$$

Or equivalently,

$$\frac{1}{r''} = \frac{1}{k_a C} + \frac{1}{k_d} \tag{5.56}$$

The parameters k_a and k_d were used exclusively by Essenhigh (1988). However, this mechanism is in conflict with some experimental observations (see the discussion regarding the graphite flake oxidation data and the rough sphere combustion data in Chapter 7). Therefore, k_a and k_d are not used in this study. Instead, k_1 and k_0 are used in place of k_a and k_d since several different mechanisms lead to expressions that can be simplified to the same form as the SNDL. For example, Laurendeau noticed that in case of surface migration control, the reaction rate becomes:

$$r'' = k_c \theta = \frac{k_c KC}{1+KC} \tag{5.57}$$

Farrauto and Batholomew (1997) proposed a three-step mechanism (adsorption of reactant, surface reaction, and desorption of product) and derived two expressions that can be simplified to the SNDL form based on two totally different assumptions: reaction control and desorption control. Since all four mechanisms can be described by the simple Langmuir rate equation, the physical meaning of k_1, k_0, and K depend on the mechanism leading to the SNDL. Therefore, it is more appropriate to k_1 and k_0 rather than k_a and k_d. Although the Langmuir rate equation is used in this study to model the carbon-oxygen reaction without specifying a mechanism, its application implies that the mechanism of this reaction necessarily involves adsorption and desorption of reactant(s) and product(s).

Constant Fractional Reaction Order Issue

Suuberg *et al.* (1988) carried out a detailed study on the reaction order and activation energy of char oxidation using phenol-formaldehyde resin chars with low impurity levels. It was observed that the reaction order varied in a narrow range (0.68±0.08) with burnout, char heat treatment temperature and oxidation temperature (573-673 K). The oxygen partial pressure examined was 0.5-101 kPa. The activation energy was observed to be about 130-150 kJ/mol (31 to 36 kcal/mol). Reade *et al.* (1995) and Reade (1996) determined the reaction orders and activation energies at atmospheric pressure for 7 different types of chars using a TGA. The reaction orders were observed to be about 0.7, and the activation energies were about 31-35 kcal/mol, consistent with the data by Suuberg and coworkers.

These experiments raised a question for the theoretical validity of the Langmuir rate equation. In both of the above studies, the reaction order seems to be independent of oxygen partial pressure. This contradicts the theoretical prediction of reaction order, which says the reaction order should decrease with increasing oxygen partial pressure (see Eq. 5.4). There are several possibilities for this difference:

First, the reaction order is often obtained by plotting ln(reaction rate at a certain temperature) vs. ln(oxygen partial pressure) and then finding the average slope of the curve. Due to the logarithm operation and the averaging process, the subtle change of reaction order is often hard to observe. This will be further illustrated by the graphite oxidation data (Ranish and Walker, 1993) in Chapter 7.

Second, both of the above studies used TGA to measure the reaction order. In TGA experiments, the gas temperature is measured and controlled. The particle temperature is assumed to be the same as the gas temperature. However, local heating of the particles is possible due to the highly exothermic nature of the char oxidation reaction. Here local heating means the particle temperature is higher than the gas temperature by a margin that makes a considerable difference in kinetics. As oxygen partial pressure increases, the reaction rate increases, thus making the local heating more severe and causing the particle temperature to increase, which causes the reaction rate to increase further. The result of local heating is over-estimation of the reaction order at higher oxygen partial pressure. According to Eq. 5.4, the true reaction order decreases with oxygen partial pressure. Thus local heating disguises the true reaction orders and serves to “stabilize” the observed reaction orders.

The third possibility is that the Langmuir rate equation is insufficient to model the carbon-oxygen reaction. Firstly, the wide variation of ASA poses a great challenge to the applicability of the Langmuir rate equation. Secondly, the Langmuir rate equation assumes a homogeneous, non-interacting surface, thus implying constant values of E_a and E_d. However, for a non-homogenous surface, the most active sites are filled first. For an interacting surface, filling of nearby sites creates repulsion forces, thus inhibiting adsorption and promoting desorption. The Temkin isotherm (Laurendeau, 1978) might be required to describe the adsorption-desorption processes of char oxidation.

In summary, the constant fractional order observed in TGA experiments at atmospheric pressure does not prove or disprove the Langmuir rate equation. The Langmuir rate equation is assumed to sufficiently describe the carbon-oxygen reaction in this study and is evaluated by comparison with experimental data.

6. High Pressure Char Oxidation Model

A new High Pressure Carbon Burnout Kinetics model (HP-CBK) was developed in this study. The HP-CBK model was based on the Carbon Burnout Kinetics model (CBK) developed by Hurt *et al.* (1998b). The intended purpose of the HP-CBK model is to describe char oxidation over wide ranges of experimental conditions (from atmospheric to elevated pressures, from low to high temperatures). The CBK model is described briefly in the first part of this chapter. The HP-CBK model differs from the CBK model in several aspects, which are detailed in the second part of this chapter.

CBK Model

The main component of the CBK model is the single-film char oxidation submodel. Some submodels (e.g., thermal annealing and ash film prohibition) and treatments (e.g., statistical treatment of properties) are available in CBK for treating near-extinction behaviors of char oxidation. These submodels were included, but were not investigated in detail in this study due to lack of detailed high pressure experimental data during late burnout.

Single-Film Char Oxidation Submodel

The single-film char oxidation model, developed by other investigators (Mitchell *et al.*, 1992; Hurt *et al.* 1998) and summarized here to set a foundation for the HP-CBK model, consists of four aspects:

1) global *n*-th order kinetics;

2) film diffusion in the particle boundary layer;

3) heat generation and transfer;

4) mode of burning expressions.

The kinetics of this submodel are simplistic. This submodel assumes that the particle is isothermal. Oxygen is assumed to be the sole oxidizer and the global *n*-th order rate equation is used to represent char oxidation rates:

$$q_{rxn} = k_s P_s^n \tag{6.1}$$

where k_s is a temperature-dependent rate coefficient, n is the apparent reaction order, and P_s is the partial pressure of oxygen at the particle surface. The global rate coefficient, k_s, implicitly includes the combined effects of pore diffusion, internal surface area, and intrinsic surface reactivity. This rate coefficient is described by an Arrhenius equation:

$$k_s = A\, exp(-E/RT_p) \tag{6.2}$$

Both CO and CO_2 are considered primary products of the heterogeneous char oxidation reactions. The CO/CO_2 product ratio (MR) is assumed to depend on particle temperature and is expressed as:

$$MR = \frac{moles\ of\ CO}{moles\ of\ CO_2} = A_c\, exp(-E_c\,/RT_p) \tag{6.3}$$

The fraction of the carbon content of the particle converted to CO_2 is denoted as ψ and determined from the CO/CO_2 product ratio (MR):

$$\psi = 1/(1 + MR). \tag{6.4}$$

The mass diffusion outside the particle is (Frank-Kamenetskii, 1969):

$$q_{diff} = \frac{k_D P}{\gamma} \ln\left(\frac{1 - \gamma P_s / P}{1 - \gamma P_g / P}\right) \quad \text{when } \gamma \neq 0 \tag{6.5a}$$

$$q_{diff} = k_D (P_{og} - P_{os}) \quad \text{when } \gamma = 0 \tag{6.5b}$$

where the mass transfer coefficient is given by:

$$k_D = \frac{M_c D_{ox} Sh}{d_p R' T_m \nu_o} \tag{6.6}$$

$$\nu_o = 0.5(1 + \psi) \tag{6.7}$$

$$\gamma = \frac{\psi - 1}{\psi + 1} \tag{6.8}$$

This assumes, of course, that oxygen is the only oxidizer and that pyrolysis reactions have been completed. Slightly different and iterative forms can be used to account for these effects, such as those in PCGC-3 (Smoot and Smith, 1985; Smith *et al.*, 1994). The quasi-steady state assumption leads to

$$q_{diff} = q_{rxn} \tag{6.9}$$

If the particle temperature is known or guessed, Eqs. (6.9), (6.1) and (6.5) can be used to determine the value of P_s. Numerically, a value is guessed for P_s, Eqs. (6.1) and (6.5) are used to compute q_{rxn} and q_{diff}, and then the difference $\Delta q_1 = (q_{rxn} - q_{diff})$ is driven to zero by changing the value of P_s using the Newton-Raphson method. This procedure for computing P_s is referred to in this study as the P_s loop.

An energy balance is used to relate the particle temperature to the reaction rate:

$$-\frac{mC_{p,p}}{S_g}\frac{dT_p}{dt}+q_{heat}\Delta H=-\frac{Nu\lambda}{d_p}\frac{\kappa}{(1-e^{\kappa})}(T_p-T_g)+\varepsilon\sigma(T_p{}^4-T_w{}^4) \quad (6.10)$$

where

$$\kappa=\frac{\gamma\ C_{p,g}d_p\nu_o q_{heat}}{M_C\lambda Nu} \quad (6.11)$$

and

$$\Delta H=\frac{1}{M_C}\left[(1-\psi)\Delta H_{CO}+\psi\Delta H_{CO2}\right] \quad (6.12)$$

where ΔH_{CO} and ΔH_{CO2} are the heats of reaction per mole carbon for the reactions C + 0.5 O_2 = CO and C + O_2 = CO_2, respectively. In some cases T_p is measured or controlled (e.g., fixed bed combustion) and the energy balance step can be skipped. The procedure for solving the energy balance equation is:

1. guess a value for T_p;
2. go through the P_s loop and compute the converged value of reaction rate (denoted as q_{ps} here): $q_{ps} = q_{rxn} = q_{diff}$;
3. compute the value of q_{heat} from the energy equation (6.10);
4. calculate the difference between the value of q_{ps} from the P_s loop and q_{heat} from the energy equation;
5. Guess a new value for T_p using Newton-Raphson method so that the difference $\Delta q = (q - q_{heat})$ is zero. Notice that this new T_p changes the value of q from the P_s loop.

6. Return to step 2 and repeat the process until the P_s loop and the energy balance are both converged. That is, $\Delta q_1 = (q_{rxn} - q_{diff}) = 0$ and at the same time $\Delta q_2 = (q - q_{heat}) = 0$.

A set of equations was derived to describe the evolution of particle size and density during combustion. The char particle is assumed to consist of two components: a combustible component whose density changes with burnout and a non-combustible inorganic component whose density is constant. The apparent density is defined as:

$$\rho_p = \frac{\text{total weight of particle}}{\text{volume of particle}} = \frac{m_c + m_a}{V_p} \tag{6.13}$$

where the particle volume includes the voids between the solid matrix. Rewriting this equation in terms of (a) the apparent densities of the combustible material and the ash, and (b) the volumes they occupy yields:

$$\rho_p = \frac{m_c}{V_p} + \frac{m_a}{V_p} = \frac{v_c}{V_p}\frac{m_c}{v_c} + \frac{v_a}{V_p}\frac{m_a}{v_a} = \frac{v_c}{V_p}\rho_c + \frac{v_a}{V_p}\rho_a \tag{6.14}$$

The weights of the combustible material and ash in the particle can be expressed as:

$$m_a = x_a V_p \rho_p = v_a \rho_a \tag{6.15}$$

$$m_c = (1 - x_a) V_p \rho_p = v_c \rho_c \tag{6.16}$$

Utilizing Eqs. (6.15) and (6.16) to eliminate v_a and v_c from Eq. (6.14) yielded the following relationship for apparent density of the coal char particle:

$$\frac{1}{\rho_p} = \frac{x_a}{\rho_a} + \frac{(1 - x_a)}{\rho_c} \tag{6.17}$$

The change of apparent carbon density is related to burnout by:

$$\frac{\rho_c}{\rho_{c,o}} = \left(\frac{m_c}{m_{c,o}}\right)^{\alpha} \tag{6.18}$$

where α is the empirical burning mode parameter (Mitchell *et al.*, 1992; Hurt *et al.*, 1998). The values of α were calculated from high temperature char oxidation data (Mitchell *et al.*, 1992) for ten U.S. coals and were found to vary only modestly from char to char, and a mean value of 0.2 can be taken as an estimate for an unknown char. After calculating a new ρ_c, Eq. (6.17) can be used to calculate the value of ρ_p, after which geometric considerations lead to:

$$\frac{d_p}{d_{p,o}} = \left[\left(\frac{m}{m_o}\right)\left(\frac{\rho_{p,o}}{\rho_p}\right)\right]^{1/3} \tag{6.19}$$

Statistical Kinetics and Properties

The CBK model accommodates statistical distribution of particle sizes (d_p), single particle reactivites (represented by the global pre-exponential factor A) and apparent carbon densities (ρ_c) in order to better describe the late stages of char oxidation (Hurt *et al.*, 1996). The number fraction of particles in the incremental parameter space [$d(d_p)dAd\rho_c$] is given by $F(d_p, A, \rho_c)d(d_p)dAd\rho_c$, where $F(d_p, A, \rho_c)$ is the joint distribution frequency function. Captive particle imaging results (Hurt *et al.*, 1996) further suggested that the distribution functions of size, reactivity and carbon density were independent from each other, so that $F(d_p, A, \rho_c)$ can be expressed as the products of these functions:

$$F(d_p, A, \rho_c) = F_d(d_p)\, F_A(A)\, F_\rho(\rho_c) \tag{6.20}$$

The size distribution function can be measured directly. The reactivity distribution function $F_A(A)$ is modeled as a gamma distribution function (Hurt *et al.*, 1996):

$$F_A(A) = \frac{e^{-\beta A}}{\Gamma(A)} A^{\alpha-1}\beta^{\alpha} \tag{6.21}$$

where α and β are the distribution parameters and Γ(A) is the gamma function. The gamma distribution has the following properties:

$$A_{mean} = \alpha / \beta \tag{6.22}$$

$$\sigma_A = \sqrt{\alpha} / \beta \tag{6.23}$$

More recent work (Hurt *et al.*, 1998) suggests that a correlation can be used generally:

$$\sigma_A / A_{mean} = 0.325 \tag{6.24}$$

Eqs. (6.22) through (6.24) suggest that α is a constant value 9.47. When A_{mean} is specified, β can be readily calculated from $\beta = \alpha/A_{mean} = 9.47/A_{mean}$.

The distribution of the initial carbon density determines the amount of carbon to be consumed in the complete burnout process. Recent measurements on a U.S. lignite using a unique electrodynamic balance technique (Hurt *et al.*, 1996) yielded an approximate Gaussian distribution of carbon densities with a standard deviation given by:

$$\sigma_\rho / \rho_{c,o,mean} = 0.3 \tag{6.25}$$

The mean values ($\rho_{c,o,mean}$) for ten U.S. coal chars are available (Mitchell *et al.*, 1992). Statistical kinetics and properties seem to play an important role in certain cases. However, incorporating statistical kinetics and properties could dramatically increase the required computer time to predict the carbon burnout. For example, a typical full calculation uses a 7 × 7 × 7 matrix to represent the distributions in size, reactivity, and carbon density, thus lengthening the time required for burnout prediction by a factor of 343 times. The developers of CBK later abandoned the use of statistical treatments of kinetics and properties in the latest version (called CBK8), probably due to computational cost considerations (Niksa and Hurt, 1999).

Thermal Annealing Submodel

The thermal annealing submodel is a variation of the distributed activation energy formulation proposed by Suuberg (1991) and demonstrated on phenol-formaldehyde carbons. The thermal annealing model assumes that the intrinsic reactivity is proportional to the total number of active sites. The active sites are assumed to have identical oxidation kinetics, but to anneal at different rates. The number of active sites for a given type is assumed to be annealed by a first order thermal process:

$$\frac{d(N_E / N_0)}{dt} = -(N_E / N_0) A_d e^{(-E_d / RT_p)} \tag{6.26}$$

where N_E is the number of active sites that share a common annealing activation energy E_d, N_0 is the total number of active sites, and A_d and E_d are the empirical kinetic parameters. All active sites are assumed to share a common pre-exponential factor for annealing, A_d, but to distributed with respect to E_d:

$$d(N_E / N_0) = f_E(t, E_d) dE_d \tag{6.27}$$

$$\frac{N(t)}{N_0} = \int_0^{\infty} f_E(t, E_d) dE_d \tag{6.28}$$

At time zero the function f_E is assumed to be a normalized log-normal distribution in E_d and integration of Eq. (6.28) yields a value of unity. In Zone I,

$$\frac{A(t)}{A_0} = \frac{N(t)}{N_0} = \left[\int_0^\infty f_E(t, E_d)\,dE_d\right] \tag{6.29}$$

In Zone II, classical Thiele theory leads to (Hurt *et al.*, 1998):

$$\frac{A(t)}{A_0} = \left[\frac{N(t)}{N_0}\right]^{1/2} = \left[\int_0^\infty f_E(t, E_d)\,dE_d\right]^{1/2} \tag{6.30}$$

The Ash Encapsulation Submodel

Mineral matter inhibits combustion in the late stages by one of several physical mechanisms. First, an ash film can pose an additional resistance to oxygen transport to the reacting surface; second, the existence of the inert ash layer outside the particle increases the diameter of the particle, reducing the global rate expressed on an external area basis.

The ash encapsulation submodel assumes the presence of a porous ash film surrounding a carbon-rich core. The core region is assumed to have a constant local mass fraction of mineral matter equal to the overall mineral mass fraction in the unreacted char. This assumption of “shrinking core” is obviously not realistic for Zone I combustion. Therefore, this ash encapsulation submodel is not ideally suited for modeling char oxidation under Zone I conditions, which is recognized by Niksa and Hurt (1999).

The detailed description of the ash encapsulation submodel can be found elsewhere (Hurt *et al.*, 1998)

HP-CBK Model Development

The HP-CBK differs from the CBK model in several aspects. First, the HP-CBK uses intrinsic Langmuir kinetics instead of global *n*-th order kinetics. Second, a pore structure model is incorporated in order to model the effective diffusivity inside the particle, which is required by the use of intrinsic kinetics. Third, new correlations are used for thermal and transport properties to accommodate high pressure situations. Last, general correlations are used for the Nusselt number and the Sherwood number in order to model char oxidation for both small and large particles.

Kinetics

The CBK model uses the global *n*-th order rate equation to represent the chemical kinetics (see Eq. 6.1). One weakness of this approach is that global kinetic parameters (A and E) cannot be extrapolated from low temperature (Zone I) to typical boiler temperature (Zone II) or vice versa. In addition, the reaction order is often observed to vary under different conditions, with limits of zero and unity.

In order to model reaction rates over wide ranges of temperature and total gas pressure, it is necessary to use intrinsic kinetics with appropriate treatment of the pore diffusion effects. The HP-CBK model utilizes the intrinsic kinetics and allows users to choose either the Langmuir rate equation or the *m*-th order rate equation to describe char oxidation kinetics (as discussed in Chapter 5):

$$q_{rxn} = \left(\eta + \frac{S_{ext}}{S_{\mathrm{int}}} \right) \frac{S_{\mathrm{int}}}{S_{tot}} \frac{k_{1p} P_s}{1 + K_p P_s} \frac{d_p M_C}{6} \tag{6.31}$$

$$q_{rxn} = \left(\eta + \frac{S_{ext}}{S_{\mathrm{int}}} \right) \frac{S_{\mathrm{int}}}{S_{tot}} k_{mp} P_s^m \frac{d_p M_C}{6} \tag{6.32}$$

where $k_{1p} = k_1/(RT_p)$, $K_p = K/(RT_p)$, and $k_{mp} = k_m/(RT)^m$. The $d_p/6$ term (which is V_p/S_g) in the above equation converts the reaction rate from a volumetric basis into external area basis, and M_C (molecular weight of carbon) converts the molar rate into mass rate.

The effectiveness factors for the *m*-th order and Langmuir rate equations are calculated based on the theoretical and numerical work detailed in Chapters 4 and 5:

$$\eta = f_c \frac{1}{M_T}\left(\frac{1}{\tanh(3M_T)} - \frac{1}{3M_T}\right) \tag{6.33}$$

$$f_c(M_T, m_{obs}) = \left(1 + \frac{\sqrt{1/2}}{\frac{1}{2M_T{}^2} + 2M_T{}^2}\right)^{\frac{1}{2}(1-m_{obs})^2} \tag{6.34}$$

where $m_{obs} = m$ for the *m*-th order rate equation;

$m_{obs} = 1/(1+K_pP_s)$ for the Langmuir rate equation;

$$M_T = L\sqrt{\frac{(m+1)}{2}\frac{\nu_o k_{mp} RTP_s{}^{m-1}}{D_e}} \quad \text{for the } m\text{-th order rate equation; and} \tag{6.35}$$

$$M_T = L\sqrt{\frac{\nu_o k_{1p} RT/D_e}{2K_pP_s + \frac{1}{1+K_pP_s}}} \quad \text{for the Langmuir rate equation.} \tag{6.36}$$

During the course of this project, Sun and Hurt (1999) incorporated the intrinsic *m*-th order kinetics in conjunction with the effectiveness factor approach into the newest version of CBK model (CBK8). In CBK8, the intrinsic reaction order is (somewhat arbitrarily) assumed to be 0.5, which makes the apparent reaction order 0.75 in Zone II.

Effective Diffusivity

The major obstacle to rigorous description of the transition between Zone I and Zone II is the treatment of pore diffusion through the complex pore structures of char. According to Smith (1981), the optimum model would include a realistic representation of the geometry of the voids (with tractable mathematics) that can be described in terms of easily measurable physical properties of the char. These properties include the surface area, porosity, density (true density or apparent density), and the distribution of void volume according to size.

In general, both molecular and Knudsen diffusion may contribute to the mass transport rate within the porous structure of the char. The combined effects of these two diffusion mechanisms can be described by the combined diffusivity D (Smith, 1981):

$$D = \frac{1}{1/D_{AB} + 1/D_K} \tag{6.37}$$

The Knudsen diffusivity can be calculated from classical kinetic theory (Smith, 1981):

$$D_K = 9.70 \times 10^3 r_p \left(\frac{T_p}{M_A} \right)^{1/2} \tag{6.38}$$

where D_K is in cm^2/sec, r_p is the pore radius in cm, T_p is in K, and M_A is the molecular weight of oxygen. The bulk diffusivity can be calculated using a correlation by Mitchell (1980):

$$D_{O2/N2} = 1.523 \times 10^{-5} T_p^{1.67} / P \tag{6.39}$$

Pore structure models are used to convert the diffusivity to the effective diffusivity. By using the effective diffusivity, the measurable diffusion flux can be based on the geometric external surface area rather than the total cross-sectional area of holes on the external surface (Smith, 1981). In addition, the effective diffusivity takes into account the deviation of the actual diffusion path from ideal cylindrical pore, such as “zigzag”, constrictions, overlaps, and other effects.

Two pore structure models are often used in converting diffusivity into effective diffusivity: the parallel pore model and the random pore model. The parallel pore model (Wheeler, 1951) uses the porosity and a “tortuosity factor” to correlate the effective diffusivity to the diffusivity:

$$D_e = \frac{\varepsilon}{\tau} D \tag{6.40}$$

where ε is the porosity, and τ is the tortuosity factor.

The random pore model was originally developed for catalytic pellets containing a bi-disperse pore system. The details of the development of this model are given elsewhere (Wakao and Smith, 1962). The resultant expressions for the effective diffusivity may be written:

$$D_e = \varepsilon_M^2 D_M + \frac{\left(\varepsilon - \varepsilon_M\right)^2 (1 + 3\varepsilon_M)}{1 - \varepsilon_M} D_\mu \tag{6.41}$$

$$D_M = \frac{1}{1/D_{AB} + 1/(D_K)_M} \tag{6.42}$$

$$D_\mu = \frac{1}{1/D_{AB} + 1/(D_K)_\mu} \tag{6.43}$$

$$(D_K)_M = 9.70 \times 10^3 r_{p,1} \left(\frac{T}{32}\right)^{1/2} \tag{6.44}$$

$$(D_K)_\mu = 9.70 \times 10^3 r_{p,2} \left(\frac{T}{32}\right)^{1/2} \tag{6.45}$$

where r_{p1} and r_{p2} are the average macro-pore and the average micro-pore radii, respectively. The random pore model has four parameters: ε (porosity), ε_M (macro-porosity), r_{p1} and r_{p2}. The porosity of a char can be determined by its apparent density and true density (see Eq. A.1 in Appendix).

Notice that the random pore model can also be applied to mono-disperse systems. For chars containing only macropores, $\varepsilon = \varepsilon_M$, and Eq. (6.41) becomes:

$$D_e = D_M \varepsilon_M^2 \qquad (6.46)$$

Similarly, for chars containing only micropores, the effective diffusivity is

$$D_e = D_\mu \varepsilon_\mu^2 \qquad (6.47)$$

Comparison of these last two equations with Eq. (6.40) leads to:

$$\tau = \frac{1}{\varepsilon} \qquad (6.48)$$

The random pore model does not require the empirical tortuosity factor, and accommodates the parallel pore model when the pore structure is assumed to be mono-disperse. Due to these advantages, the random pore model was selected in this study as the working model for calculating effective diffusivity in char oxidation modeling.

Estimating S_{ext}/S_{int} Using Pore Structure Model

The ratio of the external surface area to the internal surface area (S_{ext}/S_{int}) is an important parameter in modeling rough sphere combustion. The *in situ* value of S_{int} is often unknown, thus making it necessary to estimate or assume a value for S_{ext}/S_{int} (Banin *et al.*, 1997). However, an arbitrarily assumed value of S_{ext}/S_{int} would affect the kinetic parameters reduced from experimental data. It is therefore desirable to eliminate this arbitrariness in estimating S_{ext}/S_{int}. A pore structure model can be used to calculate the value of S_{int}/S_{ext}.

1. Mono-Disperse Pore Structure Model

Suppose that the pores in a char particle have the same radius r_p and length L. The number of pores in the particle can be calculated

$$N = \varepsilon V_p/(\pi r_p^2 L) \tag{6.49}$$

The internal surface area can be approximated by (Smith, 1981).

$$S_{int} = N 2\pi r_p L = 2\varepsilon V_p/r_p \tag{6.50}$$

Therefore the ratio of internal surface area to external surface area is

$$S_{int}/S_{ext} = (2\varepsilon V_p/r_p)/(S_g\Omega) = \varepsilon d_p/(3r_p\Omega) \tag{6.51}$$

where Ω is the roughness factor, accounting not only for the roughness of solid surface, which increases the surface area of a solid surface, but also for the penetration of oxygen within a pore before the first collision with the pore wall. The roughness is taken as 5 in the HP-CBK model (the reason for taking this value will be detailed in Chapter 7). The selection of this value will be justified in the next chapter. It should be noted that the external surface usually does not play a significant role except in some special cases (e.g., very fast kinetics, low internal surface area, and low porosity).

2. Bi-disperse Pore Structure Model

Similarly, the bi-dispersed pore structure model can be used to estimate the S_{int}/S_{ext} ratio:

$$S_{int}/S_{ext} = (\varepsilon_M/r_{p1} + \varepsilon_\mu/r_{p2})\, d_p/(3\Omega) \tag{6.52}$$

where r_{p1} is the macro-pore radius, r_{p2} is the micro-pore radius, ε_M is the macro porosity, ε_μ is the micro porosity, and Ω is the roughness factor.

Thermodynamic and Transport Properties

CBK model uses the following correlations for thermal conductivities (cal/cm/sec/K) and molar heat capacities (cal/mol/K) of nitrogen and oxygen (Mitchell *et al.* 1992):

$$\lambda_{N2} = 7.6893\times 10^{-7} T_m^{0.7722} \tag{6.53}$$

$$\lambda_{O2} = 7.1352\times 10^{-7} T_m^{0.7968} \tag{6.54}$$

$$\begin{aligned} C_{pN2} = {} & 7.7099 - 5.5039\times 10^{-3} T_m + 13.1214\times 10^{-6} T_m^2 - 11.68\times 10^{-9} T_m^3 \\ & + 5.2340\times 10^{-12} T_m^4 - 1.1732\times 10^{-15} T_m^5 - 0.1039\times 10^{-18} T_m^6 \end{aligned} \tag{6.55}$$

$$\begin{aligned} C_{pO2} = {} & 7.3611 - 5.3696\times 10^{-3} T_m + 20.542\times 10^{-6} T_m^2 - 25.865\times 10^{-9} T_m^3 \\ & + 15.946\times 10^{-12} T_m^4 - 4.8589\times 10^{-15} T_m^5 - 0.5862\times 10^{-18} T_m^6 \end{aligned} \tag{6.56}$$

In the CBK model the thermal conductivity of a gas mixture is assumed to be the linear combination of the thermal conductivities of the component gases (mainly nitrogen and oxygen):

$$\lambda = (1 - P_{O2})\lambda_{N2} + P_{O2}\lambda_{O2} \tag{6.57}$$

Similarly, the molar heat capacity of a gas mixture is

$$C_P = (1 - P_{O2})C_{P,N2} + P_{O2}C_{P,O2} \tag{6.58}$$

Eq. (6.53) to (6.56) are adopted in the HP-CBK model. However, Eq. (6.57) and (6.58) will undoubtedly fail at high pressures since the partial pressure of oxygen is often greater than 1 atm. These equations are modified to:

$$\lambda = (1 - P_{O2} / P)\lambda_{N2} + (P_{O2} / P)\lambda_{O2} \tag{6.59}$$

$$C_P = (1 - P_{O2} / P)C_{P,N2} + (P_{O2} / P)C_{P,O2} \tag{6.60}$$

Range of Reynolds Number

The CBK model was originally developed for pulverized-size char combustion in entrained flow reactor, and therefore assumed both the Nusselt number and the Sherwood numbers to be 2 since the Reynolds number is usually very small for entrained-flow pulverized char combustion. In order to model combustion of larger char particles, the CBK model was modified. The following correlations are used to calculate the Nusselt number and the Sherwood number (Ranz and Marshall, 1952; Bird *et al.*, 1960) :

$$\frac{h_m d_p}{k_f} = Nu = 2.0 + 0.60\mathrm{Re}^{1/2}\,\mathrm{Pr}^{1/3} \tag{6.61}$$

$$\frac{k_{xm} d_p}{C_f D_{ABf}} = Sh = 2.0 + 0.60\mathrm{Re}^{1/2}\,Sc^{1/3} \tag{6.62}$$

Frossling (1938) first gave a correlation of the form of Eq. (6.61), with a coefficient of 0.552 instead of 0.6 in the last term. Values between 0.6 to 0.7 were also used for the coefficient in the last term of Eq. (6.62) in coal combustion literature (Field, 1967; Mulcahy and Smith, 1969). However, the value shown in Eqs. (6.61) and (6.62) are used in this study since they have been used more widely.

7. Model Evaluation and Discussion

The HP-CBK model, using the Langmuir rate equation, the effectiveness factor and the random pore model, was evaluated by comparison with five sets of pressure-dependent reactivity data: 1) graphite flake data (Ranish and Walker, 1993); 2) rough sphere combustion data (Banin *et al.*, 1997a); 3) large particle oxidation data (Mathias, 1996); 4) pulverized char drop-tube data (Monson, 1992); and 5) TGA and FFB data from this study.

Proper values have to be assigned to the kinetic and pore structure parameters in order for the HP-CBK model to predict the char oxidation rates in agreement with experimental data. An optimization model, *StepIt* (Chandler, 1999) was used to adjust the kinetic parameters (A_{1p}, E_{1p}, A_p, and E_p) and pore structure parameters (r_{p1}, r_{p2} and ε_M) within pre-set ranges to best fit the experimental data. The optimum values of the parameters were used in the HP-CBK model. The HP-CBK model was then evaluated by comparing the model calculations to experimental data. In this sense the HP-CBK model **unifies and explains** experimental data with one different set of parameters for each set of data, rather than **predicts** the reaction rates. This is still a substantial contribution, since little is known about high-pressure char oxidation. The correlations between kinetic parameters (activation energies and pre-exponential factors) and measurable char properties are not yet possible, since experimental data at high pressures and temperatures are so limited. However, it is thought that the approach used in the HP-CBK model is unique and promising, and may eventually yield coal-general correlations.

Graphite Flake Data

Ranish and Walker (1993) measured the oxidation rates of some highly crystalline graphite flakes in pure oxygen at pressures between 1 and 64 atm and temperatures between 733 and 842 K. They observed that the reaction order decreased from 0.83 to 0.69 as the reaction temperature increased from 733 to 813 K. This observation contradicts the prediction of Essenhigh (1988), which suggested that the reaction order should increase with increased temperature at constant oxygen pressure.

The graphite flakes used in these experiments had a very low reactivity. Under the conditions of these experiments, boundary layer diffusion resistance can be safely neglected. Since these graphite flakes were non-porous, pore diffusion did not occur. The reaction temperatures were controlled, and therefore heat transfer between gas and the graphite flakes does not need to be considered. For all the above reasons, these data are free from the complications of mass and heat transfer, and are ideal for testing kinetic expressions.

The Langmuir rate equation was applied to these rate data and seemed to agree well with these rate data at three temperatures over the entire range of oxygen pressure (see Figure 7.1). The Langmuir rate equation also captures the change of observed reaction order with temperature. Note that the reaction orders (the *m*'s in Figure 7.1) are the averaged slopes of the lines in Figure 7.1. Since the graphite flakes used in these experiments are non-porous, the rate equation can be expressed in a slightly different form. The best-fit kinetic parameters from this study are in the following equation:

$$r'_{in} = \frac{k'_{1p} P_{O2}}{1 + K_p P_{O2}} = \frac{6.29 \times 10^8 e^{-51,100/RT} P_{O2}}{1 + 13.4 e^{-10,100/RT} P_{O2}} \tag{7.1}$$

where r'_{in} is in mol C/(gC remaining)/sec, R is the gas constant (1.987 cal/mol/K), and T is the reaction temperature in K, P_{O2} is the oxygen partial pressure in atm.

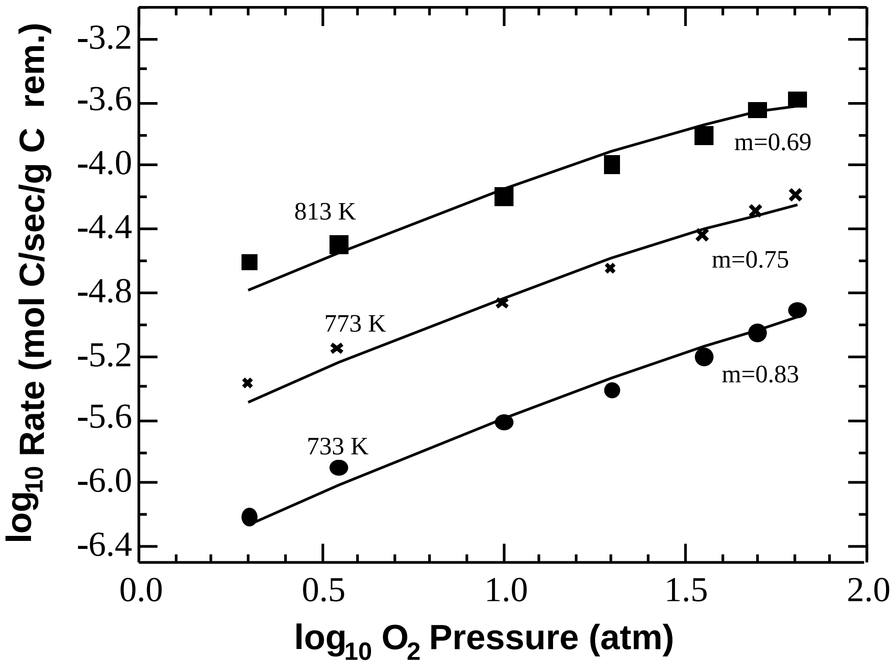

Figure 7.1. Comparison of predictions of carbon reactivity with graphite flake data (Ranish and Walker, 1993) obtained as a function of P_{O2} and T_p. Symbols represent measured data. Curves represent predictions from a single Langmuir rate expression (Eq. 7.1).

One important observation in these experiments was that the reaction order decreased with temperature over the same range of oxygen pressure. In order to allow the reaction order to decrease with temperature, the activation energy of K_p must be positive (see Eqs. 5.4 and 5.13). From Eq. 7.1 and the definition of k_0 (the ratio of k_{1p} to K_p), E_0 = (51.1-10.1) = 41.0 kcal/mol, which is less than E_{1p} (51.1 kcal/mol). It is commonly believed that the activation energy of adsorption is smaller than that of desorption (Essenhigh, 1988; Du *et al.*, 1991). Based on the adsorption-desorption interpretation (see Chapter 2), E_{1p} and E_0 are the activation energies of adsorption and desorption, respectively. The above finding indicates that either the adsorption-desorption interpretation of the Langmuir rate equation or the belief that the activation energy of adsorption is smaller than that of desorption is not true. The understanding from this project is: 1) the mechanism of the carbon-oxygen reaction is not well understood and the adsorption-desorption interpretation of the Langmuir rate equation may not be true; 2) impurities can affect the activation energies of different processes in the carbon-oxygen reaction to different extents. Keeping these two points in mind, it is no surprise that E_{1p} can be less than, equal to, or greater than E_0.

Rough Sphere Combustion Data

Banin *et al.* (1997a) measured the temperatures and relative sizes of char particles in shock tube experiments. The gas temperature was varied between 1200 and 1800 K and the total gas pressure was about 8 atm. The mole fraction of oxygen in the mixture was varied from 0 to 100%. The char was made from Gottelborn coal (a high volatile bituminous coal) and ground to a mean size of 5 μm. The particle temperature and relative size measurements were based on two-wavelength infrared pyrometry and the reaction rate of char was based on the energy balance assuming CO was the sole primary product (this is a reasonable assumption since particle temperatures are between 1480 and 2850 K). For consistency with the rate data reduction, this assumption (that CO was the sole primary product) was adopted in this study.

Banin *et al.* (1997a) calculated the reaction orders from the char oxidation rate data and gave a 3-dimensinal representation of the reaction order as a function of the particle temperature and oxygen partial pressure. From this plot, the reaction order decreases as temperature increases, again suggesting that the activation energy of K is positive (equivalently, E_{1p} is greater than E_0).

Another important observation from that plot is that at high temperature and high oxygen partial pressure, the measured reaction order is less than 0.5. There are two possible explanations: 1) the combustion occurs in Zone I or in the transition zone from Zone I to Zone II, but not in Zone II, if the external combustion rate is assumed to be negligible compared to the internal combustion rate; 2) combustion occurs in Zone II and the external combustion rate cannot be neglected compared to the internal combustion rate. The latter is the so-called rough sphere combustion hypothesis. On the external surface area the combustion rate is not affected by internal diffusion and therefore allows true kinetics and a reaction order below 0.5. Numerical calculations in this study showed that the first explanation was inadequate to simultaneously explain the observed rates and the reaction orders, and the rough sphere combustion hypothesis was examined quantitatively.

Banin *et al.* used a simple Langmuir rate equation to describe the intrinsic reaction rates and a microscopic pore structure model to account for the pore growth. It was shown that the reaction rate was virtually constant over the whole range of burnout except in the initial stage, which lasted only a short period of time. Since microscopic pore structure models require extensive computational efforts, it is desirable to use a macroscopic pore structure model and an effectiveness factor to model the char oxidation rates. Further, since the pore growth did not play a significant role in determining the reaction rate as a function of burnout (or time), the potential benefit of using microscopic pore structure models was not realized. Therefore, the values of porosity, reactivity and pore size are assumed to be spatially uniform (a necessary assumption in order to use the effectiveness factor approach) and temporally constant (not a necessary assumption to use the effectiveness factor approach, but used for simplicity).

Results and Discussion

The following Langmuir rate equation was used in the HP-CBK model:

$$r_{in}''' = \frac{2.26\times 10^{11} e^{-46{,}500/RT} P_{O2}}{1 + 1.67\times 10^{4} e^{-18{,}800/RT} P_{O2}} \tag{7.2}$$

This means that E_{1p} = 46.5 kcal/mol, and E_0 = (46.5 - 18.8) = 27.7 kcal/mol. The observed reaction rate is:

$$q_{rxn} = r_{obs}''' \frac{V_p}{S_g} M_C = \left(\eta + \frac{S_{ext}}{S_{\text{int}}}\right)\frac{S_{\text{int}}}{S_{tot}} r_{in}''' \frac{d_p M_C}{6} \tag{7.3}$$

A mono-disperse pore structure model was used to calculate the effective diffusivity D_e and to estimate the value of S_{ext}/S_{int} (as discussed in Chapter 6). The parameters related to the pore structure model are in Table 7.1.

Table 7.1. Pore Structure Parameters in Modeling the Data by Banin *et al*.

Roughness factor = 5 (Pre-set)   Porosity = 0.5 (Pre-set)
Pore diameter = 10.8 Å (Adjusted)

The value of the roughness factor was pre-set to be 5, which seemed high compared to the value of 2.5 used by Banin *et al.* (1997). Following the argument of Banin *et al.* (1997), the roughness factor accounts not only for the increased surface area due to surface roughness, but also for penetration of oxygen molecules within a pore before the first collision with the pore wall. The latter mechanism means internal diffusion does not play any role up to a distance equal to about the pore diameter. Figure 7.2 illustrates how this latter mechanism makes one unit of void surface area equivalent to 4 units of solid surface area.

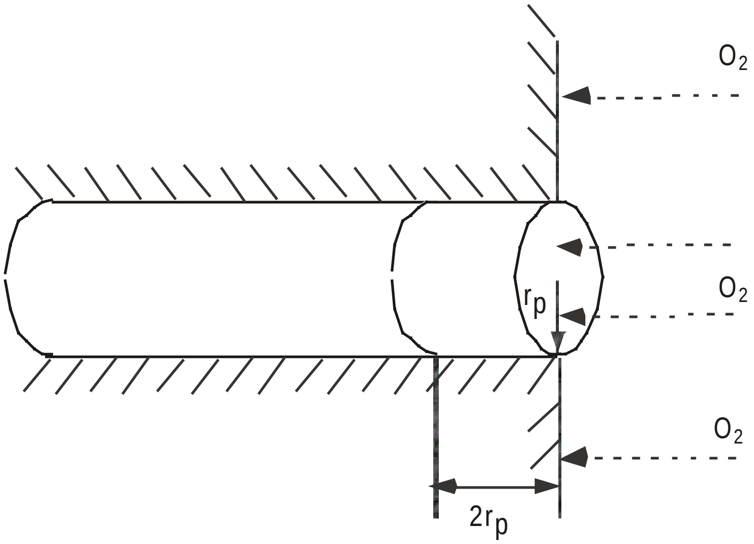

Figure 7.2. Schematic of a pore connected to the surface of a char particle. One unit of void area is equivalent to 4 units of solid area since internal diffusion does not play any role up to a distance equal to about the pore diameter.

The void area of a pore mouth is πr_p^2, while the internal pore wall that is not affected by internal diffusion and must be counted as external surface area is $2\pi r_p \cdot 2r_p = 4\pi r_p^2$. Assuming that the surface roughness increases the surface area by a factor of 2, the overall roughness factor can be calculated from the porosity of the particle: $2[(1-\varepsilon) + 4\varepsilon]$

= 2[1 + 3ε] = 2(1 + 3 × 0.5) = 5. Although the value of the overall roughness factor is pre-set somewhat arbitrarily, it was found that the choice of this value is critical to allow the reaction order to span the wide range (0.3 to 0.8) observed in experiments. For example, if the overall roughness factor is pre-set to 2.5 as used by Banin *et al.* (1997), the reaction order would not span the whole range from 0.3 to 0.8 (such as 0.4 – 0.65) no matter how the kinetic parameters and other pore structure parameters are adjusted.

Table 7.2. Results of Calculations of Reaction Rate and Reaction Order

Oxygen Pressure (atm)	Measured T_p (K)	Reaction rate (kg/m^2/sec)		Error (%)	Calculated Reaction Order
		Measured	Calculated		
8.3	2850	14	14.6	4.1	0.33
8.2	2000	4.7	4.9	4.3	0.51
8.0	1480	1.1	1.1	-1.0	0.71
4.7	2140	4.5	4.6	1.0	0.51
4.3	1725	1.6	1.7	6.2	0.68
4.0	2680	9.5	8.2	-14.0	0.38
2.3	1640	0.8	0.8	-1.1	0.80
1.9	1900	1.7	1.5	-12.0	0.71
1.3	2550	2.9	3.2	11.0	0.60

This work is considered an improvement to the original work of Banin *et al.* in several aspects: 1) This work uses the analytical expressions to predict the effectiveness factor for the Langmuir rate equation instead of numerically solving the oxygen concentration profile in the particle, which requires much more computational time. 2) This work quantitatively explains the “rough sphere combustion phenomenon” and also explains how the observed reaction order changes with temperature and oxygen partial pressure. 3) The original work requires a parameter containing the ratio of internal surface area to external surface area:

$$\chi = \frac{S_{\text{int}}}{S_{ext}} \sqrt{D_e \frac{r_p}{a^2} \frac{2M_C}{M_{O2}}} \tag{7.4}$$

This work uses the pore structure parameter to estimate the ratio of external surface area to internal surface area and thus uses less adjustable parameters than the original work. 4) This work sets the porosity as 0.5, which seems more realistic than the value of 0.1 used in the original work. 5) This work predicted the reaction rates within 14% error (see Appendix B for definition of error) while the original work predicted the rates with error as high as 27%.

Large Particle Oxidation Data

The variation of mass with time was measured (Mathias, 1996) for mostly 8-mm diameter Pittsburgh char particles in the High-Pressure Controlled Profile (HPCP) drop-tube reactor (Monson *et al.*, 1995) using a Cantilever Balance Attachment (CBA; Bateman *et al.*, 1995).

The HPCP reactor (see Figure 7.3) uses a series of electrical heaters to maintain the wall temperature profile of the furnace. Oxidizing gas is preheated electrically to desired temperature before going into the furnace. The reactor has the following demonstrated capabilities: total pressure from 1 to 15 atm, gas temperature up to 1700 K, controllable temperature profile along the reaction tube length, particle residence time from 30 to 1000 ms, variable gas compositions of inert and oxidizing gases, and optical access ports for *in situ* diagnostics. Detailed descriptions of the HPCP reactor are available elsewhere (Monson, 1992; Monson and Germane, 1993; Monson *et al.*, 1995).

The HPCP reactor was originally built to quantify the oxidation rates of small particles injected into the hot gas flow, and was later modified to study reactivity of large particles by removing the injection probe and replacing the probe with a type-S thermocouple (located 1.2 cm above the particle) to measure the gas temperature. The CBA is attached to one of the optical access port to allow horizontal introduction of the large particle into the hot oxidizing gas flow. The CBA consists of a 0-30 g force transducer, a 3.2-mm ceramic cantilever rod and a stainless steel wire mesh basket secured to the end of the rod. The mass of the burning char particle was recorded by videotaping the readout of the force transducer. Description of the CBA can also be found in literature (Bateman, 1993; Bateman *et al.*, 1995; Mathias, 1996).

The chars were prepared from Pittsburgh coal (VM 39%; moisture 0.74%; and ash 11.2%) in nitrogen at a gas temperature of 1050 K, a gas velocity of 0.32 m/sec, a gas pressure of 0.85 atm and a residence time of 32 seconds. Mass release due to pyrolysis was around 45% on a raw coal basis (e.g., typically a 0.11-g char particle was produced from a 0.2 g coal particle). Most of the char particles used in the oxidation experiments had an initial mass of 0.11g (corresponding to an initial diameter of 8 mm), except in the two conditions designed to study the effects of size.

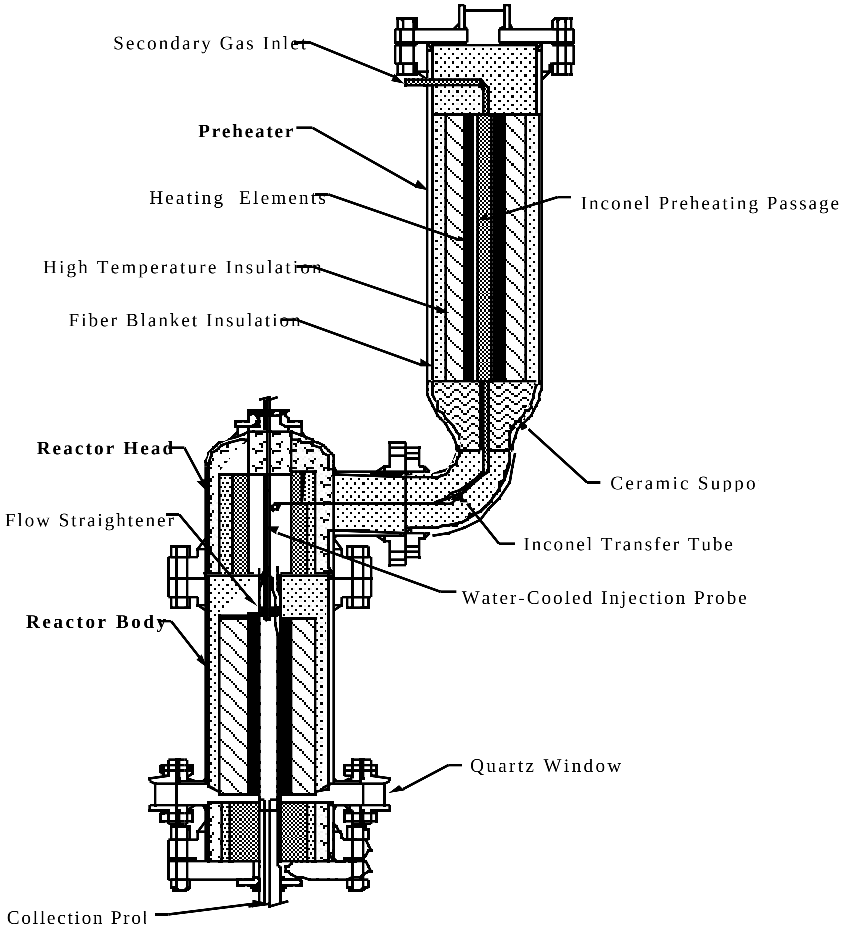

Figure 7.3. Schematic of High Pressure Controlled-Profile (HPCP) drop-tube reactor.

A baseline condition was selected and a parametric set of experiments was conducted by varying one (sometimes two) of the six parameters (V_g, P_{O2}, P_{tot}, m_o, x_{O2}, T_g), as shown in Table 7.3. The parametric set consists of a suite of 13 conditions. Five experiments were performed at each of these 13 conditions to reduce random errors and to determine the repeatability.

Table 7.3. Conditions of the Large Particle Experiments

	P_{tot} (atm)	P_{O2} (atm)	V_g (m/s)	T_g (K)	d_{po} (mm)	x_∞
Base	0.85	0.18	0.32	1050	8.00	21%
1	*		0.08			
2			1.28			
3	0.85	0.12				14%
4	0.85	0.06				7%
5	3	0.63				21%
6	5	1.05				21%
7	3	0.21				7%
8	5	0.21				4.2%
9					6.35	
10					9.16	
11				1200		
12†				825		

* A blank cell means that the value is maintained at the baseline condition;
† Condition excluded due to prolonged heating-up period.

The particle center temperatures were measured for three conditions (base condition, and conditions 11 and 12) using a type-S thermocouple inserted in a small hole drilled approximately to the center of the particle and attached to the particle with a small amount of epoxy. For all of these three conditions, the temperature profiles all show a characteristic drop near the end of combustion (at about 85% daf burnout). This drop of temperature is consistent with the near-extinction behavior observed by Hurt and Davis (1994). The main interest of this study is the reaction rates before the near-extinction stage, and therefore average reactivities were determined for the 10-70% burnout region (the reaction rates before 10% burnout were also discarded since the particles were still heating up at early burnout). In addition, the temperature profile of condition 12 (T_g = 825 K) showed that the particle was heating up continuously until the near-extinction behavior began. This prolonged heating period is due to the very low gas temperature and the large size of the particle, and makes this condition different from all other conditions. Therefore, this one condition was excluded in this study.

The particle reaction rates were originally reported as normalized mass rates (*dU/dt*) vs. burnout (*B*). The unburned fraction (*U*) and burnout (*B*) are related by:

$$B = 1 - U \tag{7.5}$$

Notice that both U and B are on a dry ash-free basis.

The normalized mass rates (dU/dt) were converted to mass rates per unit external surface area as follows: 1) For each experimental condition, three values were obtained from the dU/dt curve at B = 20, 40, and 60%, respectively. 2) The mass release rates (*dm/dt*) were calculated from the normalized mass release rates (*dU/dt*) by:

$$\frac{dm}{dt} = m_{co}\frac{d(m/m_{co})}{dt} = m_{co}\frac{dU}{dt} \tag{7.6}$$

where m_{co} is the initial mass of the carbonaceous material in the char. Notice that there was 11.2% ash in the Pittsburgh coal. For the baseline condition, the coal particle had an initial mass of 0.2 g and thus had 0.0224 g ash. After devolatilization the char had a mass of 0.11 g and the mass of ash was assumed to be unchanged (0.0224 g). The initial mass of carbonaceous material could be obtained by subtraction: m_{co} = 0.11 – 0.0224 = 0.0876 g. 3) The values of diameter at different burnouts were estimated assuming that the particle density remains constant with burnout. This assumption is supported by the measurements by Mathias (1996). The diameter can be calculated from

$$(d/d_o)^3 = (m + m_{ao})/(m_o + m_{ao}) \tag{7.7}$$

where m_{ao} is the initial mass of ash. 4) The mass fluxes at the external surface were calculated from the mass release rates (*dm/dt*) and the external surface area (πd_p^2). It was found that for each condition the reaction rates based on the external surface area are almost identical at burnouts of 20, 40 and 60%, indicating a constant burning rate between 10 – 70% burnout. For each condition, the reaction rates at these three burnouts were averaged to yield a **characteristic reactivity**, which was used in model validation.

The values of χ factor were calculated for all of the conditions assuming the CO/CO_2 product ratio can be estimated using an empirical Arrhenius correlation adopted from Hurt and Mitchell (1992b):

$$CO/CO_2 = 4.0\times10^4 \exp(-30000/1.987/T_p). \tag{7.8}$$

According to this correlation, 87% carbon is converted to CO_2 and 13% to CO at 1200 K. This CO/CO_2 correlation was chosen so that the particle temperatures predicted by the HP-CBK model matched the limited number of measured particle center temperatures. It was found that the values of χ factor ranged from 0.2 – 0.7, indicating that combustion did not occur in Zone III (i.e., reaction was not limited by film diffusion). If the CO/CO_2 product ratio is chosen so that more carbon is converted to CO, the values of χ factor would be even smaller and farther away from Zone III conditions. It was therefore concluded that these reaction rates are not controlled by boundary layer diffusion, and hence chemical kinetics and pore diffusion have to be considered in modeling these data.

The HP-CBK model was used to predict the characteristic reactivities at all 12 conditions of the Mathias experiments with a single set of kinetic and pore structure parameters. The particle sizes used in the HP-CBK model were those at 40% burnout since the characterisic reactivities represent the averaged reactivities over 10 - 70% burnout. The particle temperatures were calculated from energy balance (see Eq. 6.10), taking into account convection, radiation and heat generation from reaction (Mitchell *et al.*, 1992).

Kinetic parameters (A_{1p}, E_{1p}, A_p and E_p) and pore structure parameters (r_{p1}, r_{p2} and ε_M) were adjusted to minimize the difference between the predictions and the data. Three observations were made:

1) The best fit used an intrinsic Langmuir rate equation that reduced to a zero-th order reaction;
2) The diffusivity contributed from micropores can be neglected compared to the diffusivity contributed from macropores.
3) Macropores are large enough so that Knudsen diffusivity can be neglected compared to molecular diffusivity.

The first finding means that K_pP_{os} is much greater than 1 so that the Langmuir rate equation reduced to a zero-th order rate equation:

$$r_{in}'' = \frac{k_{1p}P_{os}}{1+K_pP_{os}} \approx \frac{k_{1p}P_{os}}{K_pP_{os}} = \frac{k_{1p}}{K_p} = k_0 = A_0e^{-(E_0/RT)} \tag{7.9}$$

Therefore the absolute values of k_{1p} and K_p could not be determined but their ratio $k_{1p}/K_p = k_0$ was determined. The intrinsic zero-th order kinetics implied an apparent order of 0.5 in Zone II, which is repeatedly observed (Smith, 1982) or assumed (Mitchell *et al.*, 1992) for high temperature char oxidation:

$$r_{obs}''' = \eta k_0 = \frac{1}{M_T}k_0 = \frac{6}{d_p}\sqrt{\frac{2D_eP_{os}}{\nu_O k_0 RT}}k_0 = \frac{6}{d_p}\sqrt{\frac{2D_ek_0}{\nu_O RT}}P_{os}^{1/2} \tag{7.10}$$

$$q_{obs} = r_{obs}'''\frac{d_pM_c}{6} = 12\sqrt{\frac{2D_ek_0}{\nu_O RT}}P_{os}^{1/2} \tag{7.11}$$

The second and third findings mean that the effective diffusivity is only determined by the macro-porosity (ε_M):

$$D_e = \varepsilon_M^2 D_{O2,\ N2} = 1.523 \times 10^{-5} T_p^{1.67} \varepsilon_M^2 / P \tag{7.12}$$

These three findings greatly simplified the model and reduced the number of adjustable parameters to three: A_0, E_0, and ε_M. The best-fit kinetic and pore structure parameters are listed in Table 7.4. By using this set of parameters, the HP-CBK model was able to quantitatively explain the effects of all six experimental variables: total pressure, oxygen partial pressure, oxygen mole fraction, gas velocity, gas temperature, and particle size with a standard deviation of 14% and a maximum error of 22% (see Appendix B). The resulting comparison of the HP-CBK model to the experimental data is shown in Figure 4.

Table 7.4. Parameters Used in Modeling the Data by Mathias.

A_0 = 0.75 mol/cm^3/sec E_0 = 18.2 kcal/mol
Porosity = 0.65 (Calculated and Pre-set)
Macroporosity ε_M = 0.28

The activation energy E_0 seems low compared the values observed for pulverized char oxidation. However, these char particles were prepared from large coal particles and might differ from the char prepared from small particles in reactivity and pore structure.

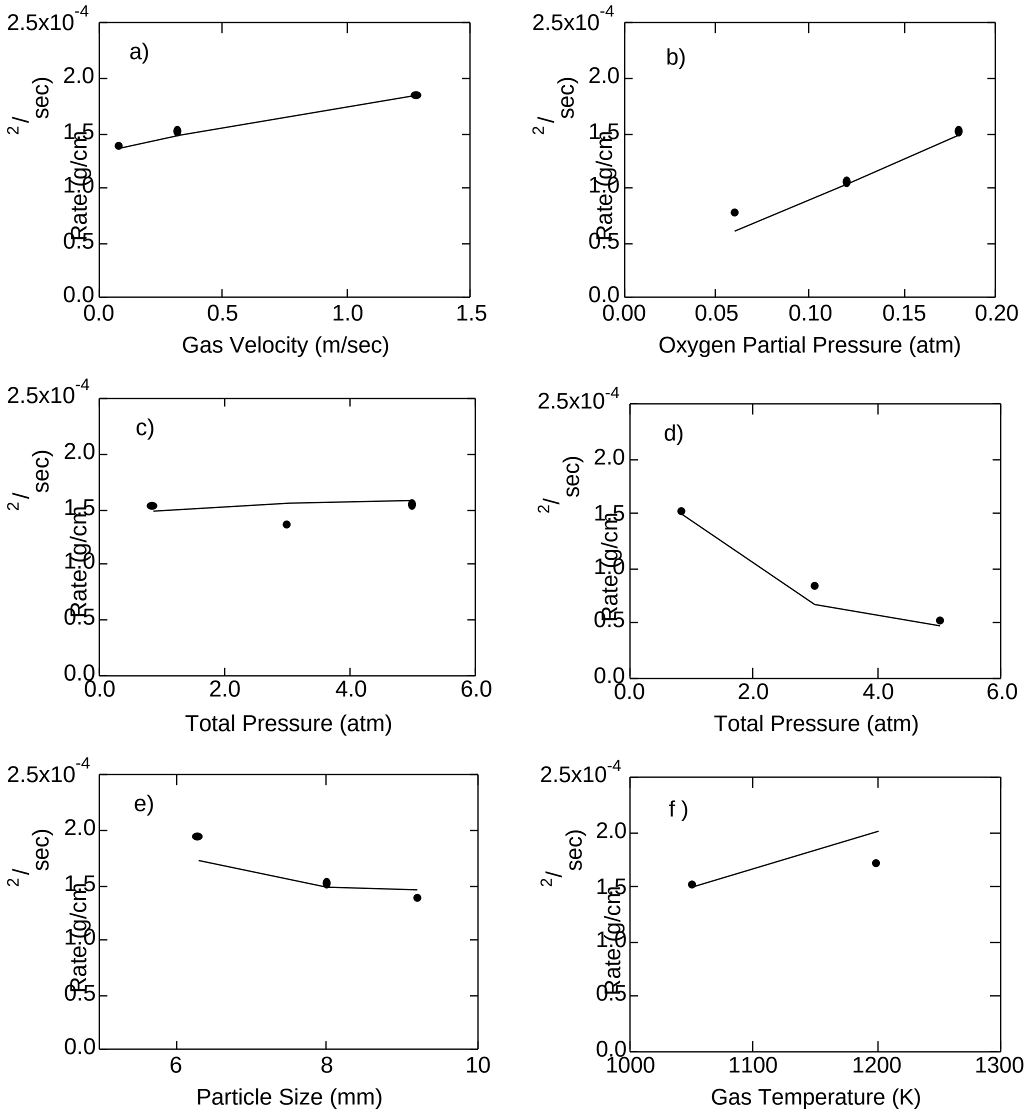

Figure 7.4. Comparison of the HP-CBK predictions of reaction rate with large coal char particle data (Mathias, 1992) as a function of a) V_g, b) P_{O2} (P_{tot} = 0.85 atm), c) P_{tot} (x_{O2} = 21%), d) P_{tot} (P_{O2} = 0.18 atm), e) d_p, f) T_g.

Pulverized Char Drop-Tube Data

Monson (1992) conducted char oxidation experiments on a 70-μm Utah coal char at total pressures of 1, 5, 10, and 15 atm. Chars were prepared in the HPCP furnace in a nitrogen environment at atmospheric pressure, wall and gas temperatures of 1500 K, and a residence time of 300 ms. In the char oxidation experiments, reactor temperatures were varied between 1000 and 1500 K, with 5% to 21% oxygen in the bulk gas, resulting in average particle temperatures up to and 2100 K and burnout from 15% to 96% (daf).

Approach

Two injection probes, one cooled and the other uncooled, were used during the tests. Because of the large heat loss and the greater particle dispersion associated with the cooled probe, only the experiments using the uncooled probe were considered in this study. In addition, the majority of the experiments used a reaction length between 6.5 – 12.5 cm while a few experiments used reaction length as short as 4 cm. Although the particles were pre-heated in the uncooled probe, there existed a short transient period in which ignition and momentum transfer (between the particle and the secondary gas) occurred. For experiments using a very short reaction length, this transition period may affect the accurate calculation of reaction rates. Therefore, the experiments with a reaction length shorter than 6 cm were not considered in this study. After the above screening, 45 experiments were modeled in this study (see Table 5).

Table 7.5. The Experimental Conditions and Measurements by Monson (1992).

RL	P	X_{O2}	$T_g(0)$	$V_p(0)$	B	T_3	T_2	T_1
7.5	0.97	10	1145	0.94	38.2	1169	1196	1150
9.5	0.96	10	1145	1.00	49.2	1165	1199	1147
6.5	0.95	21	1145	1.10	75.3	1174	1195	1151
7.5	0.95	21	1145	1.13	63.0	1171	1194	1152
10.5	0.95	21	1145	1.19	70.3	1171	1194	1152
10.5	0.94	21	1145	1.12	73.6	1163	1205	1141
10.5	0.92	21	1145	1.11	78.1	1168	1205	1140
10.5	0.92	21	1145	1.07	68.4	1168	1205	1140
10.5	0.91	21	1145	1.08	74.1	1168	1205	1140
6.5	0.93	21	1469	1.23	68.4	1529	1533	1444
8.0	0.93	21	1469	0.96	86.7	1528	1525	1448
9.5	0.93	21	1469	1.00	89.5	1526	1520	1454
11.5	1.01	10	1469	0.94	85.8	1522	1523	1458
10.5	0.96	21	1145	1.05	83.4	1165	1200	1146
9.5	5.26	10	1336	0.90	91.5	1475	1415	1298
8.5	5.12	10	1131	1.11	46.6	1187	1214	1122
11.5	5.15	10	1131	1.00	59.8	1183	1223	1122
14.5	5.15	10	1131	1.02	66.0	1183	1223	1122
6.5	5.21	21	1131	1.21	80.0	1205	1200	1103
8.0	5.32	21	1131	1.16	74.1	1202	1190	1107
9.5	5.38	21	1131	1.29	87.4	1200	1190	1107
8.5	5.30	4.2	1336	0.71	55.0	1469	1424	1313
12.5	5.00	4.0	1336	0.78	58.4	1453	1441	1332
11.5	5.26	10	1336	0.85	85.2	1468	1427	1310
6.5	5.25	21	1336	1.01	84.8	1490	1428	1283
8.0	5.33	21	1336	1.00	90.7	1485	1408	1279
9.5	5.31	21	1336	0.98	96.1	1480	1406	1285
6.5	9.86	5	1006	0.49	41.7	1071	580	755
9.5	9.75	5	1006	0.49	45.6	1071	603	766
6.5	9.84	10	1006	0.52	51.8	1073	884	747
6.5	10.4	10	1006	0.53	66.9	1087	853	751
6.5	10.4	10	1006	0.49	60.2	1085	855	751
6.5	10.4	10	1006	0.53	65.7	1088	858	753
6.5	10.4	10	1006	0.52	69.3	1086	855	750
8.5	9.79	10	1006	0.65	78.6	1071	910	760
6.5	9.87	21	1006	0.73	87.5	1042	757	714
8.5	10.2	10	1173	0.63	82.6	1208	652	810
10.5	9.95	10	1173	0.70	90.2	1216	782	822
7.5	10.1	21	1173	0.60	96.9	1230	945	817

* RL: reaction length L in cm; P: total pressure in atm; X_{O2}: oxygen mole fraction in bulk gas; $T_g(0)$: gas temperature (K) at the collection point; $V_g(0)$: the final velocity (m/sec) measured immediately before the particles were collected; B: daf burnout; T_1, T_2 and T_3: wall temperatures (K) at x = 1.3, 6.4 and 16.5 cm, respectively.

Table 7.5. (continued)

RL	P	X_{O2}	$T_g(0)$	$V_p(0)$	B	T_3	T_2	T_1
6.5	15.4	5	987	0.24	23.4	987	714	635
8.5	15.5	5	987	0.25	43	987	712	642
6.5	15.3	10	987	0.25	70.2	1002	730	635
6.5	15.4	21	987	0.29	73	980	710	631
8.5	15.3	21	987	0.34	92.8	988	710	641
8.5	15.1	10	987	0.3	80.7	1009	730	660

* RL: reaction length L in cm; P: total pressure in atm; X_{O2}: oxygen mole fraction in bulk gas; $T_g(0)$: gas temperature (K) at the collection point; $V_g(0)$: the final velocity (m/sec) measured immediately before the particles were collected; B: daf burnout; T_1, T_2 and T_3: wall temperatures (K) at x = 1.3, 6.4 and 16.5 cm, respectively.

In these experiments, the temperatures and velocities of the particles were measured using a two-color pyrometer (Monson, 1992; Cope, 1994; Tichenor *et al.* 1992) immediately before the particles entered the collection probe. The reported particle temperatures seem unreasonably high, and do not permit balancing of the particle energy equation. It is likely that many of the actual particle temperatures were below the temperature measurement threshold, and only a few non-representative particles were measured. Such errors were shown for other char oxidation experiments with low gas temperatures by Fletcher and Hardesty (1992). Therefore, the measured particle temperatures were not used. Instead, a CO/CO_2 product ratio was assumed and the particle temperatures were calculated by the model. The carbon burnout (daf) of the collected particles was determined following the contents of three tracers (ash, Ti and Al). For each test, burnout values were calculated using each of the tracers. In almost every case the three values agreed within a few percent, promoting confidence in the determination of burnout.

The burnout and particle velocity data were used to validate the model. It was assumed that the particle velocities are always equal to the local gas velocities. This assumption is commonly accepted for entrained-flow, pulverized-char combustion. Gas velocity is proportional to gas temperature. The final velocities of particles measured by Monson (1992) were used to calculate the gas velocity (and hence particle velocity) at any location between the injection point ($x = L$) and the collection point ($x = 0$):

$$V_p(x) = V_g(x) = V_g(0)\frac{T_g(x)}{T_g(0)} \tag{7.13}$$

where x is the distance from the collection point.

The wall temperatures in the HPCP furnace were not uniform. Three thermocouple were used by Monson (1992) to measure the wall temperatures at three locations: $x_1 = 1.3$ cm, $x_2 = 6.4$ cm, and $x_3 = 16.5$ cm. Non-uniform wall temperatures were correlated using a quadratic equation:

$$T_w(x) = ax^2 + bx + c \tag{7.14}$$

where $$a = \frac{\frac{T_1 - T_2}{x_1 - x_2} - \frac{T_1 - T_3}{x_1 - x_3}}{x_2 - x_3}$$

$$b = \frac{T_1 - T_2}{x_1 - x_2} - a(x_1 + x_2)$$

$$c = T_1 - ax_1^2 - bx_1$$

where T_1, T_2 and T_3 are wall temperatures at axial locations x_1, x_2 and x_3, respectively. These wall temperature data were from Monson's experimental records, and to the author's knowledge have never been published before. These wall temperature profiles were used directly in the HP-CBK model. A burning char particle interacts with the non-uniform wall temperatures through radiative heat transfer. In order to simplify the calculation of radiative heat transfer, it was assumed that the wall temperature at the same height of the particle might be considered the average wall temperature that the particle interacted with. The errors incurred by using this assumption are thought to be small.

The measured centerline gas temperature profiles varied mainly with total pressures (Monson and Germane, 1993). It was observed that the gas temperature drop between the injection point and the collection point increased with total pressure. For a certain total pressure, the temperature profiles showed similar patterns. Therefore, the temperature profiles were approximated by (see Figure 7.5):

For $P = 10$ and 15 atm: $T_g(x) = -0.5(x-20)^2 + 200 + T_g(0)$

For $P = 5$ atm: $T_g(x) = -0.4(x-20)^2 + 160 + T_g(0)$ when $x < 10$

$T_g(x) = T_g(0) + 120$ when $x \geq 10$

For $P = 1$ atm: $T_g(x) = -0.35(x-20)^2 + 140 + T_g(0)$ when $x < 5$

$T_g(x) = T_g(0) + 61.3$ when $x \geq 5$

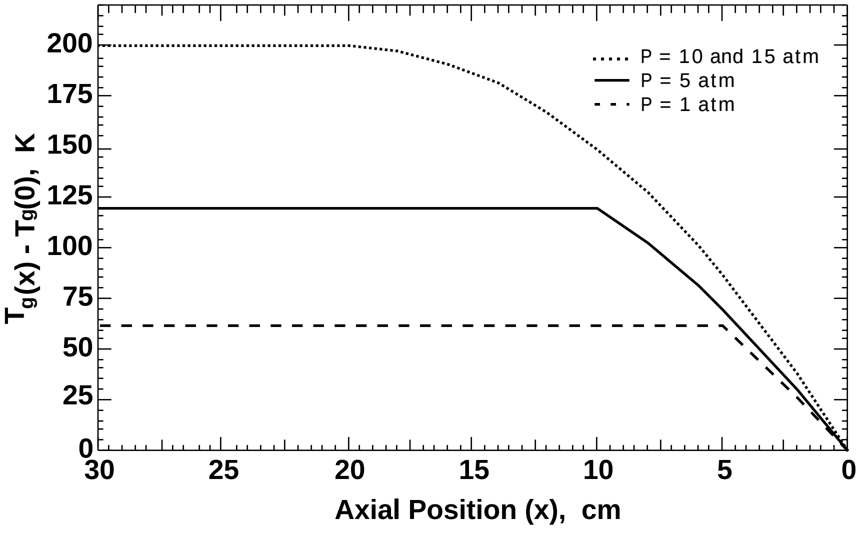

Figure 7.5. The gas temperature profiles for different total pressures were approximated by step-functions (quadratic equations near the collection point and straight lines far away from the collection point).

The HP-CBK was used to predict the burnouts for all the experiments conducted at 1, 5, 10 and 15 atm, using the above-mentioned gas temperature and wall temperature profiles. The experiments conducted at 15 atm had extremely low wall temperatures (e.g., 631 K) and low gas temperatures (e.g., 987 K), and hence were not considered due to ignition problems. Ignition problems were also observed by other researchers. For example, Field (1969) observed that a 38-μm char sample was not ignited at low gas temperature and wall temperature (< 1230 K).

Results

In minimizing the standard deviation of model predictions, two observations were made: 1) The Langmuir rate equation reduced to the zero-th order equation, implying an apparent reaction order of 0.5 in Zone II; and 2) The diffusivity contributed from micropores can be neglected compared to that from the macropores.

The kinetic and pore structure parameters used in this study are listed in Table 7.6. The best-fit calculations of burnouts from the HP-CBK are compared with the experimental measurements in Figures 7.6 and 7.7. The HP-CBK model was able to predict particle burnouts with a standard deviation of 14% and a maximum error of 36%.

Table 7.6. Parameters Used in Modeling the Data by Monson (1992).

A_0 = 2.42 × 10^3 mol/cm^3/sec	E_0 = 21.7 kcal/mol
Total Porosity ε = 0.5 (Pre-set)	Macro-porosity ε_M = 0.25
Macro-pore radius r_{p1} = 2000 Å (Pre-set)	

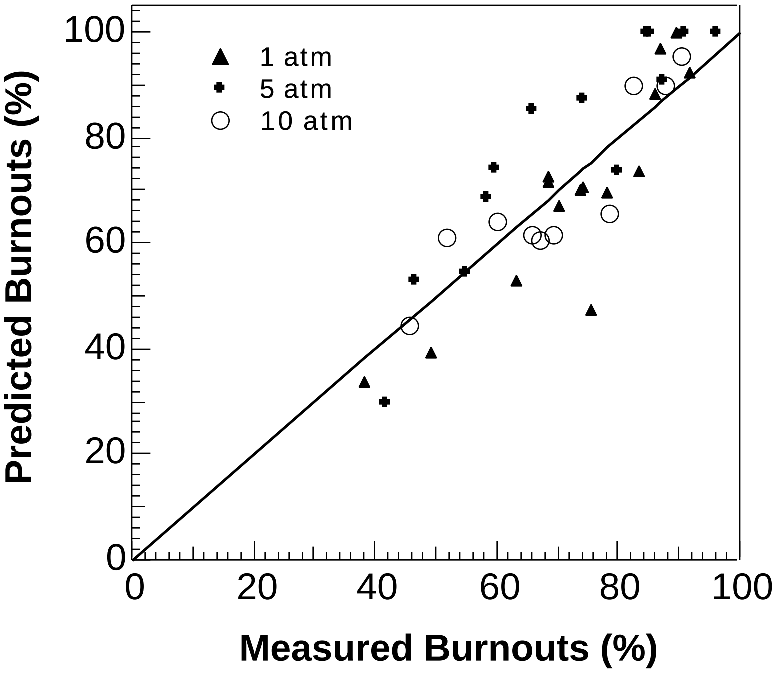

Figure 7.6. Comparison of HP-CBK predictions of carbon burnouts with pulverized coal char data (Monson, 1992) at total pressures of 1, 5, and 10 atm.

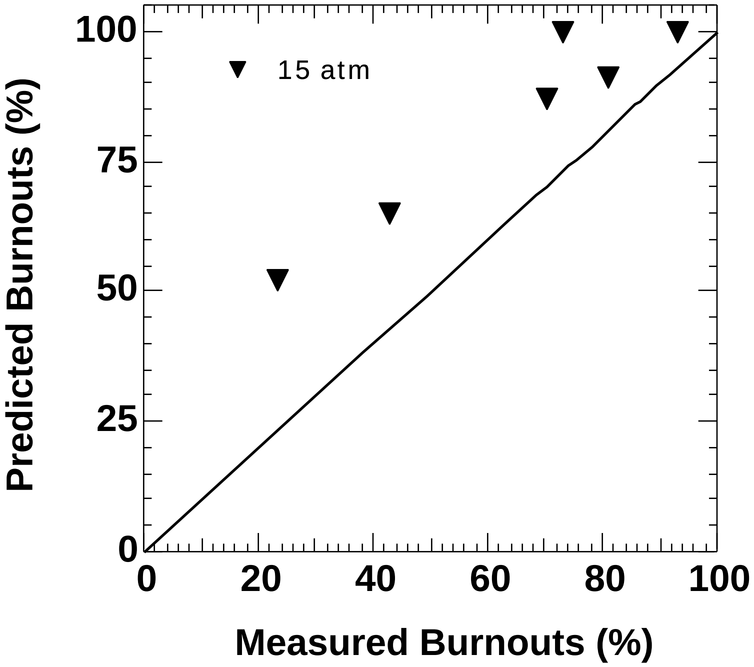

Figure 7.7. Comparison of HP-CBK predictions of carbon burnouts with pulverized coal char data (Monson, 1992) at a total pressure of 15 atm.

TGA and FFB Data-This Study

The reactivities of a south African coal char (Koonfontain) were studied in this project at atmospheric pressure using a thermogravimetric analyzer (TGA) and the flat-flame burner (FFB) at this laboratory as reported in the appendix. Koonfontain coal particles (with a mean diameter of 60 μm) were injected into the FFB from the bottom and devolatilized within the first inch in the burner. In the fuel-lean flames (methane fuel-lean, condition #2, and CO fuel-lean, condition #4), the resulted char continued to react with oxygen in the gas. The char particles were collected at 1, 2, 4, and 6” above the flame and the mass releases of these partially oxidized char particles were measured. The high temperature reactivities were calculated from these mass releases. The TGA reactivities were also measured for these partially oxidized chars at a gas temperature of 823 K (550 °C). The HP-CBK model was used to unify the low temperature TGA rate data and the high temperature FFB rate data.

The TGA reactivities are a function of burnout. The effects of burnout on reactivities were not the main interest of this project and were not explored in detail. Therefore, average TGA reactivities were used in this comparison with the HP-CBK model. The centerline gas temperatures were not uniform in the FFB. However, between two adjacent collection points the gas temperatures vary in a narrow range and may be approximated by an average temperature.

The high temperature reaction rates between 4 and 6” were (somewhat arbitrarily) selected to evaluate the HP-CBK model. The rate data and experimental conditions are listed in Table 7.7.

Table 7.7. Rate Data and Experimental Conditions

	Condition #2	Condition #4
Description of condition	Methane fuel-lean, 8% post-flame oxygen	CO fuel-lean, 9.6% post-flame oxygen
FFB reactivity between 4” and 6”	1.10×10^{-3} $g_C/cm^2/sec$	1.18×10^{-3} $g_C/cm^2/sec$
Average gas temperature between 4” and 6”	1743 K	1743 K
Average TGA reactivity of the chars collected at 4” above the flame	1.14×10^{-3} $g_C/g_{C\ remaining}/sec$ (3.39×10^{-7} $g_C/cm^2/sec$)*	0.27×10^{-3} $g_C/g_{C\ remaining}/sec$ (7.21×10^{-8} $g_C/cm^2/sec$)*
TGA conditions	823 K, 10% oxygen, 0.85 atm	823 K, 10% oxygen, 0.85 atm
Char particle diameters	62 μm	60 μm
Char density	0.377 g/cm^3	0.367 g/cm^3
N_2 BET surface area	71.6 m^2/g	49.2 m^2/g

* Reaction rates based on the external surface area were calculated from the TGA rates based on the mass of carbon remaining.

In modeling the data by Monson (1992) and Mathias (1996) it was found that the micro-pores made insignificant contributions to the effective diffusivity. Therefore, two parameters related to pore structures are required: the macro-porosity (ε_M) and average radius of macro-pores (r_{p1}). The macro-porosity was estimated as 0.3. The N_2 BET surface areas were assumed to represent the surface area contributed by macro-pores (in this study, pores are classified into only two categories: macro-pores and micro-pores; pores with a diameter greater than 20 Å are considered here to be macro-pores) and were used to estimate the average pore radius:

$$r_{p1} = \frac{2\varepsilon_M}{\rho_p S_m} \tag{7.15}$$

This equation can be derived as follows: Suppose that there are N_p pores (with average pore diameter r_{p1}) in a single particle, the number of pores (N_p) can be obtained from considerations of the volume of a single pore and the total void volume:

$$N_p = \frac{\varepsilon_M V_p}{V_{pore}} \tag{7.16}$$

where V_p is the volume of the single particle, V_{pore} is the volume of a single pore. The specific internal surface area of this single particle is then:

$$S_m = \frac{S_{in}}{m} = \frac{N_p S_{pore}}{\rho_p V_p} = \frac{\varepsilon_M V_p}{V_{pore}} \frac{S_{pore}}{\rho_p V_p} = \frac{S_{pore}}{V_{pore}} \frac{\varepsilon_M}{\rho_p} = \frac{2}{r_{p1}} \frac{\varepsilon_M}{\rho_p} \tag{7.17}$$

Eq. 7.15 can be easily obtained by re-arranging Eq. 7.17.

Conditions #2 and #4 differed mainly in the post-flame steam concentrations. The effects of steam were not explored in detail in this project. Therefore two sets of kinetic parameters (A_{1p}, E_{1p}, A_p, and E_p) are required for the chars made in condition #2 and those made in #4. This means there are four adjustable parameters to fit two data points (one TGA rate and one high temperature rate) for either case #2 or case #4. Unfortunately, additional measurements at different temperatures and oxygen concentration were not possible. For such an under-constrained problem, multiple solutions exist.

Reade *et al.* (1995) and Reade (1996) measured the reaction order and activation energy of various chars using a TGA at atmospheric pressure. They consistently observed a reaction order of about 0.7 and an activation energy of about 34 kcal/mol. Although the reaction orders and activation energies were not measured for the Koonfontain chars in this study, it is illustrative to assume that the observations of Reade (1996) hold true for the Koonfontain chars in this study. For the Koonfontain chars made under condition #2, it is required that four parameters be found within the following constraints:

1) the observed reaction order is 0.7 at a gas temperature of 823 K, an oxygen mole fraction of 10%, and a total pressure of 0.85 atm;

2) the observed activation energy is 34 kcal/mol at a gas temperature of 823 K, an oxygen mole fraction of 10%, and a total pressure of 0.85 atm;

3) the reaction rate is 3.39×10^{-7} $g_C/cm^2/sec$ at a gas temperature of 823 K, an oxygen mole fraction of 10%, and a total pressure of 0.85 atm;

4) the reaction rate is 1.10×10^{-3} $g_C/cm^2/sec$ at a gas temperature of 1743 K, an oxygen mole fraction of 8%, and a total pressure of 0.85 atm.

According to the theoretical developments in Chapter 5, the first constraint can be written as:

$$\frac{1}{1 + A_p e^{-E_p / RT} P_{os}} = m_{obs} \ (= 0.7) \tag{7.18}$$

where P_{os} is 0.085 atm (10% of 0.85 atm). The second constraint is:

$$-R \frac{d \ln(q)}{d(1/T)} = E_{obs} \quad (= 34 \text{ kcal/mol}) \tag{7.19}$$

Strictly speaking, E_{obs} is equal to $-R\, d[\ln(k)]/d[\ln(1/T)]$. However, in many TGA experiments P_{os} is maintained at a constant level and therefore the above equation can be used. The third constraint is:

$$q = \frac{A_{1p} e^{-E_{1p} / RT} P_{os}}{1 + A_p e^{-E_p / RT} P_{os}} \frac{M_C d_p}{6} \ (= 3.39 \times 10^{-7} \text{ g}_C/\text{cm}^2/\text{sec}) \tag{7.20}$$

The fourth constrained is:

$$q = \eta \frac{A_{1p} e^{-E_{1p}/RT} P_{os}}{1 + A_p e^{-E_p/RT} P_{os}} \frac{M_C d_p}{6} \quad (= 1.10 \times 10^{-3}\ g_C/cm^2/sec) \qquad (7.21)$$

The effectiveness factor η and the oxygen partial pressure at the external surface P_{os} must be determined iteratively by the HP-CBK model. Eqs. 7.18 through 7.21 were used to solve for the four kinetic parameters: A_{1p}, E_{1p}, A_p, and E_p.

For the Koonfontain chars made under condition #4, the constraint equations were similar to Eqs. 7.18 through 7.21 except that the observed activation energy was assumed as 37 kcal/mol instead of 34 kcal/mol, since a higher E_{obs} was required to unify the TGA rate and the FFB rate.

Results

In an attempt to simplify Eq. 7.19, it was found that the observed activation energy (E_{obs}) under TGA conditions is related to E_{1p}, E_p and the observed reaction order as follows:

$$E_{obs} = E_{1p} - (1 - m_{obs}) E_p = E_{1p} - \frac{K_p P_{os}}{1 + K_p P_{os}} E_p \qquad (7.22)$$

This equation can be obtained by substituting Eq. 7.20 into Eq. 7.19. This equation may have significant theoretical implications. The best-fit kinetic and pore structure parameters used in the HP-CBK model are listed in Table 7.8. Since there are only two rate data measurements for each flame condition (one TGA data point and one FFB data point), the HP-CBK model was able to fit exactly both of these sets of rate data.

Two different sets of kinetic parameters are required to model the rate data for Koonfontain chars #2 and #4 since these two chars were made in different environments and differed in density, N_2 BET surface area, and TGA reactivities. The values of E (8.50

kcal/mol for char #2 and 7.0 kcal/mol for char #4) compared well with the value (10.1 kcal/mol) observed for graphite flakes (Ranish and Walker, 1993). The values of E_0 (28.1 kcal/mol for char #2 and 32.1 kcal/mol for char #4) compared well with the value (27.7 kcal/mol) observed for the rough sphere combustion data (Banin *et al.*, 1997). For both char #2 and char #4, the Langmuir rate equations reduced to zero-th order rate equation at high temperatures (e.g., at a gas temperature of 1900 K), consistent with the observations in modeling the data by Monson (1992) and those by Mathias (1996). At a gas temperature of 1743 K (corresponding to a particle temperature of 1672 K for char #2 and 1676 K for char #4), the observed reaction order (n_{obs}) was about 0.6, implying an intrinsic order (m_{obs}) of about 0.2 (see Chapter 5).

Table 7.8. Parameters Used in Modeling the TGA and FFB Data (This Study)

For Condition #2 (methane fuel-lean, with 8% post-flame oxygen)
$A_{1p} = 2.34 \times 10^6$ mol/cm^3/sec/atm $E_{1p} = 36.6$ kcal/mol
$A_p = 9.11 \times 10^2$ atm^{-1} $E_p = 8.50$ kcal/mol
($A_0 = A_{1p}/A_p = 2.57 \times 10^3$ mol/cm^3/sec $E_0 = E_{1p} - E_p = 28.1$ kcal/mol)
Macro-porosity $\varepsilon_M = 0.3$ (Assumed)
Macro-pore radius $r_{p1} = 22$ Å (Calculated from Eq. 7.15)

For Condition #4 (CO fuel-lean, with 9.6% post-flame oxygen)
$A_{1p} = 2.44 \times 10^6$ mol/cm^3/sec/atm $E_{1p} = 39.1$ kcal/mol
$A_p = 3.64 \times 10^2$ atm^{-1} $E_p = 7.0$ kcal/mol
($A_0 = A_{1p}/A_p = 6.70 \times 10^3$ mol/cm^3/sec $E_0 = E_{1p} - E_p = 32.1$ kcal/mol)
Macro-porosity $\varepsilon_M = 0.3$ (Assumed)
Macro-pore radius $r_{p1} = 33$ Å (Calculated from Eq. 7.15)

The HP-CBK model unified the TGA reactivity and the high temperature reactivity, and quantitatively explained the reaction orders ($m_{obs} = 0.7$ at 823 K and

$m_{obs} = 0$ at high temperatures) and activation energy, although the values of reaction order and activation energy were assumed rather than measured. In the future, the measured values of reaction order and activation energy of these chars may become available, and more extensive comparisons will become possible.

A global n-th order rate equation is inadequate to unify reaction rates in both Zone I (TGA data) and Zone II (FFB data). Although an intrinsic m-th order rate equation has the possibility to unify the rates in both Zone I and Zone II, it cannot explain the change of reaction order with temperature, such as those observed by Ranish and Walker (1993). Assuming a constant reaction order of 0.7 would yield an apparent reaction order of 0.85 in Zone II, which is not commonly observed at high temperatures.

Summary

The HP-CBK model theoretically could use up to 7 adjustable parameters (E_{1p}, A_{1p}, E_p, A_p, r_{p1}, r_{p2} and ε_M). Compared to the n-th order rate equation, which has three parameters (A, E_{obs}, and n), the HP-CBK model has more adjustable parameters. However, in many cases the number of adjustable parameters were reduced. For example, for non-porous graphite flakes, no pore structure parameters (r_{p1}, r_{p2} and ε_M) were needed. In some cases, the Langmuir rate equation reduced to a zero-th order rate equation, and E_0 (which is equal to E_{1p}-E_p) and A_0 (which is equal to A_{1p}/A_p) were required as input parameters instead of E_{1p}, A_{1p}, E_p, and A_p. The curve-fitted parameters and assumptions used for each set of data are listed in Table 7.9.

The global n-th order rate equation has obvious difficulties: it cannot be extrapolated between Zone I and Zone II; it insufficiently describes the effects of total pressure on reaction rates; and it insufficiently reflects the change of reaction order (which means it insufficiently models reaction rates as a function of oxygen partial pressure). The use of the intrinsic Langmuir rate equation eliminates these difficulties. The increase of adjustable parameters is a cost for all these advantages. In addition, as understanding of the pore structures of chars grows, the uncertainties with pore structure parameters will reduce over time.

Table 7.9. Parameters and Assumptions (If Any) Used in the HP-CBK Model

Data Set Parameters	Ranish and Walker (1993)	Banin *et al*. (1997)	Mathias (1996)	Monson (1992)	This study (Conditions #2)
A_{1p}	6.29×10^{8} mol C/(gC remaining)/sec/ atm	2.26×10^{11} mol/cm^3/sec/ atm	N/I	N/I	2.34×10^{6} mol/cm^3/sec/ atm
E_{1p} (kcal/mol)	51.1	46.5	N/I	N/I	36.6
A_p (atm^{-1})	13.4	1.67×10^{4}	N/I	N/I	9.11×10^{4}
E_p (kcal/mol)	10.1	18.8	N/I	N/I	8.5
$A_0 = A_{1p}/A_p$	N/I	N/I	0.75 mol/cm^3/sec	2.42×10^{3} mol/cm^3/sec	
$E_0 = E_{1p} - E_p$ (kcal/mol)	N/I	N/I	18.2	21.7	
r_{p1}	N/A (non-porous)	N/A (mono-disperse)	Large enough so that Knuden diffusion can be neglected.	200 nm (Pre-set)	Calculated
r_{p2}	N/A (non-porous)	1.08 nm	*	*	Effects assumed negligible.
ε_M	N/A (non-porous)	N/A (mono-disperse)	0.28	0.25	0.3 (assumed)
Total number of adjustables	4	5	3	3	4
CO/CO$_2$ ratio	N/A**	CO is the only product†	‡	‡	‡

Note: N/A stands for "Not applicable"; N/I stands for "Not independent".
* Effects of micropores are negligible.
** No CO/CO$_2$ ratio is needed since particle temperatures are known.
† Particle temperatures are between 1480 and 2850 K. CO can be assumed as the only product with little error at such high temperatures.
‡ $4.0 \times 10^{4} \exp(-30000/1.987/T_p)$

Currently the correlations between the kinetic parameters and measurable char properties have not been established. In order to use the HP-CBK model to predict char oxidation rates at high temperatures and high pressures for a new char, the following experimental data is required:

1) high pressure TGA reactivities at different total pressures (e.g., 1, 3 and 10 atm) at different (at least 2) temperatures. These data can be used to determine the kinetic parameters (A_{1p}, E_{1p}, A_p and E_p) for the Langmuir rate equation.
2) porosity, N_2 BET surface area and CO_2 surface area of the char. These data can be used to estimate pore structure parameters.

However, additional high temperature reactivity data as a function of coal type are needed for complete verification of the model.

8. Summary and Conclusions

The objective of this project was to develop a model that can be used to explain and unify char oxidation rates over wide ranges of experimental conditions, including temperature, total pressure, oxygen mole fraction and particle size. A secondary objective of this work was to explore how the apparent reaction order of char oxidation changes with experimental conditions. The theoretical challenge in carbonaceous solid combustion, known as the rough sphere combustion phenomenon, was also explored. The accomplishments are summarized and conclusions are drawn below.

Analytical Solutions of the Effectiveness Factors

Bischoff (1965) proposed a so-called "general asymptotic solution" for predicting the effectiveness factor for an arbitrary rate form. Based on the work of Bischoff, a general modulus (Eq. 2.30) was obtained in this study for the Langmuir rate equation. This is the first time that the general modulus for the Langmuir rate equation has been applied to char oxidation.

The asymptotic solutions of the effectiveness factors for both the Langmuir rate equation and the *m*-th order rate equation were examined by comparison with numerical solutions. It was found that the general asymptotic solutions lead to errors as high as 17% in the intermediate range of the Thiele modulus. A correction function was developed to improve the accuracy of the general asymptotic solutions. The corrected general asymptotic solutions predict the effectiveness factors within 2% for both rate forms. In addition, two simplified moduli were found for the Langmuir rate equation. These empirical moduli are more computationally robust than the theoretically-derived modulus.

Theoretical Developments

The Observed Reaction Order in Zone I and Zone II

The reaction order was observed to vary with experimental conditions (temperature and oxygen partial pressure) with limits of zero and unity. The Langmuir rate equation was used to quantitatively predict how the observed reaction order would change in Zone I and Zone II assuming the Langmuir rate equation was adequate for describing the char oxidation rates (see Eqs. 5.4 and 5.13). The Langmuir rate equation allows the observed reaction order to change between zero and unity in Zone I, and to change between 0.5 and unity in Zone II if external combustion is negligible compared to internal combustion (see Table 5.1).

Rough Sphere Combustion

Under some conditions, the reaction rate of char oxidation is influenced by both pore diffusion and kinetics (Zone II combustion), while the reaction order is observed to be less than 0.5, which contradicts the conventional three-zone theory. This phenomenon is called rough sphere combustion. Rough sphere combustion occurs when the reaction rate contributed from the external surface area cannot be neglected compared to the rate contributed from the internal surface area. The apparent reaction order can be less than

0.5 due to the contribution from the external surface area. Rough sphere combustion is favored by factors that reduce the product of the internal surface area and the effectiveness factor. These factors include:

1) Small specific surface area (typically in highly ordered carbon).
2) Factors that reduce the effective diffusivity (D_e) and hence reduce the effectiveness factor (η), such as pore constriction, blind pores and low porosity. Small pore size can reduce the effective diffusivity but is often associated with larger internal surface area, and therefore is excluded from this category.
3) Very fast kinetics, which increases the value of the general Thiele modulus and hence reduces the effectiveness factor.

Knudsen Diffusion and Molecular Diffusion

In modeling pore diffusion, Knudsen diffusion and molecular diffusion are used to calculate the effective diffusivity. It is well known that molecular diffusion can be neglected for very small pores and Knudsen diffusion can be neglected in very large pores. It is desirable to quantitatively define the threshold pore sizes for these simplifications. The concept of a “critical pore size” was proposed in this project and the mathematical expression was given for this critical pore size. At the critical pore size, the Knudsen diffusivity is equal to the molecular diffusivity. When the pore size is at least 20 times larger than the critical pore size, Knudsen diffusion can be neglected. When the pore size is at least 20 times smaller than the critical pore size, molecular diffusion can be neglected. In most char oxidation cases, both diffusion mechanisms have to be considered.

Second Effectiveness Factor and ERE

Essenhigh (1988) proposed a so-called “second effectiveness factor” to account for the internal combustion of char oxidation in conjunction with the Langmuir rate equation. This method has theoretical and practical difficulties (see Chapters 2 and 5). The effectiveness factor approach developed in this project can potentially overcome all these difficulties.

Essenhigh (1988) also proposed a "Extended Resistance Equation" (ERE) to represent the char oxidation rates. The ERE takes into account boundary layer diffusion, adsorption, desorption and internal combustion (pore diffusion effects) while retaining a simple form. However, it was shown in Chapter 5 that the ERE is mathematically invalid except for some special cases (e.g., when the Langmuir kinetics reduces to first order, or when the film diffusion resistance can be neglected). The approach used in this project overcomes this difficulty with minimal computational efforts.

Mechanisms

Although the adsorption-desorption mechanism (Essenhigh, 1988) is commonly assumed when the Langmuir rate equation is used, many different mechanisms lead to expressions that can be simplified to the Langmuir rate equation. The approach of this project is general and independent of specific mechanisms. Therefore, k_1 and k_0 (two rate constants) are used in this project instead of k_a (adsorption rate constant) and k_d (desorption rate constant).

It is commonly believed that the activation energy of adsorption is lower than that of desorption. Based on this belief and the adsorption-desorption interpretation of the

Langmuir rate equation, the reaction order should increase with temperature. However, some experiments showed that the reaction order of the char-oxygen reaction decreased with increased particle temperature at constant oxygen concentration (Ranish and Walker, 1993; Banin *et al.*, 1997a). These observations indicated that either the adsorption-desorption interpretation of the Langmuir rate equation or the belief that E_a is less than E_d is not true.

The understanding from this project is: 1) the mechanism of the Langmuir rate equation is not well understood, and the adsorption-desorption interpretation may not be true; 2) impurities can affect the activation energies of different processes to different extents. Keeping these two points in mind, it is no surprise that E_1 (E_a is not used since the mechanism is not known) can be less than, equal to, or greater than E_0.

Observed Activation Energy in Zone I

An expression (Eq. 7.22) was developed to relate the observed activation energy to the activation energies of k_{1p} and K_p under Zone I conditions, provided that the oxygen partial pressure at the external surface of the particle (P_{os}) is constant.

HP-CBK Model

The High Pressure Carbon Burnout Kinetics model (HP-CBK) was developed in this project. This new model was based on the CBK model developed by Hurt *et al.* (1998b). The HP-CBK was shown to be satisfactory in modeling char oxidation at both atmospheric and elevated pressures. The HP-CBK model used: 1) intrinsic Langmuir kinetics rather than global *n*-th order kinetics; 2) the analytical solution of the effectiveness factor for the Langmuir rate equation with a correction function to improve its accuracy; 3) a pore structure model for calculation of the effective diffusivity, taking into account both Knudsen diffusion and molecular diffusion; and 4) general correlations for Nusselt and Sherwood numbers, which allowed the HP-CBK model to be used for both entrained-flow pulverized char oxidation and large-particle combustion in fixed beds.

The HP-CBK model was evaluated by comparison with five sets of high-pressure experimental data: 1) graphite flake oxidation data (Ranish and Walker, 1993); 2) rough sphere combustion data (Banin *et al.*, 1997a); 3) large-particle oxidation data (Mathias, 1996); 4) pulverized-char drop-tube data (Monson, 1992), and 5) TGA and FFB data from this study.

Results showed that the HP-CBK model was able to quantitatively explain: 1) the effects of temperature, total gas pressure, oxygen mole fraction, particle size and gas velocity on reaction rates; 2) the change of reaction order with temperature and oxygen partial pressure observed by Ranish and Walker (1993) and by Banin *et al.* (1997); 3) the reaction order (typically about 0.7) and activation energy (typically 34 kcal/mol) observed in TGA experiments (Reade, 1996); and 4) the apparent reaction order of 0.5 typically observed at high temperatures, implying a true order of zero (Smith, 1982). Therefore, the Langmuir rate equation, when used with the appropriate effectiveness factor, seems to be satisfactory for modeling char oxidation over wide ranges of experimental conditions.

In modeling the data by Mathias (1996) and those by Monson (1992), it was found that the Langmuir rate equation reduced to an intrinsic zero-th order equation for both cases. The intrinsic zero-th order equation implies an apparent order of 0.5 in Zone

II, in agreement with many observations (Smith, 1982; Mitchell *et al.*, 1992). This suggests that an *intrinsic* m-th order ($m = 0$) is adequate for modeling char oxidation rates as a function of total pressure **at high temperatures**, although a *global* n-th order rate equation has been shown to be inadequate for that task. However, an intrinsic m-th order rate equation is inadequate for modeling char oxidation over a wide range of particle temperature since the intrinsic reaction order is typically non-zero **at low temperatures** and may change with temperature (Ranish and Walker, 1993).

In the specific cases examined in this study, micropores can be neglected compared to macropores in modeling the effective diffusivity in the porous char matrix, in agreement with the experimental observation (reactivity correlates well with feeder-pore surface area, but not with micro-pore surface area; see Appendix).

Principal Conclusions

The principal conclusions drawn from this study are listed below:

1) The HP-CBK model, which uses the Langmuir rate equation and a corrected general asymptotic solution of the effectiveness factor and has three to five adjustable parameters depending on the data set, satisfactorily explains char oxidation rates over wide ranges of experimental conditions (including total pressure, temperature, oxygen mole fraction and particle size) for the following data sets:
   - graphite flake oxidation data (P = 2 to 64 atm; pure oxygen; T_p = 733 to 814 K)
   - entrained flow data (67 μm; P = 1, 5 and 10 atm; T_g = 1006 to 1469 K)
   - large particle data (ca. 6 to 9 mm; P = 1, 3 and 5 atm; T_g = 825 to 1250 K)
   - small particle data (5 μm; P = 8 atm; T_p = 1480 to 2850 K)
   - extrapolation of atmospheric TGA data to high temperature rate data

2) The effectiveness factor approach developed in this study overcomes the theoretical and practical difficulties encountered when using the “second effectiveness factor” approach proposed by Essenhigh (1988).

3) The “Extended Resistance Equation” (ERE), developed to avoid iteration (Essenhigh, 1988), was shown in this study to work only for a few special cases. The iterative approach used in this study solves this problem with minimal computational efforts.

4) The correction function developed in this study reduces the error of the general asymptotic solution of the effectiveness factor from up to 17% to less than 2%.

9. Recommendations

The predictive capability of a model is believed to rely on the fundamental understandings of the physical and chemical processes in char oxidation. The following ideas are recommended for future work in improving the char oxidation model:

- Only a limited number of high-pressure char oxidation data are available. Additional data sets would be very valuable in order to explore the applicability of this model.
- More theoretical and experimental studies should be conducted to better understand the mechanism of the carbon-oxygen reaction. Other Langmuir-Hinshelwood rate expressions may better describe the kinetics of char oxidation and therefore should be explored. However, care should be taken to minimize the number of unknown rate coefficients.
- The accurate modeling of the effective diffusivity is important in order to predict char oxidation rates. More studies are recommended for pore structure and its evolution with burnout. Pore structure models based on measurable properties (N_2 and/or CO_2 surface areas, porosity, etc.) are recommended.
- Work should be conducted to establish correlations between kinetic parameters (E_{1p}, A_{1p}, E_0, A_0) to measurable properties (coal rank, H and O content of coal and char, CaO surface area, etc.).

- The CO/CO_2 product ratio is a major uncertainty in char oxidation modeling. It likely depends on the total gas pressure and the oxygen partial pressure. More work should be conducted to address this issue.

References

Ahmed, S., M. H. Back and J. M. Roscoe, “A Kinetic Model for the Low Temperature Oxidation of Carbon: I,” *Combustion and Flame*, **70**, 1 (1987).

Aris, R., *The Mathematical Theory of Diffusion and Reaction in Permeable Catalysts,* Clarendon Press, Oxford, UK (1975).

Arthur, J. R., “Reaction Between Carbon and Oxygen,” *Trans. Faraday Soc.*, **47**, 164 (1951).

Balzhiser, R. E. and K. E. Yeager, "Coal-Fired Power Plants for the Future", *Scientific American*, **9**, 100 (1987).

Banin V., R. Moors and B. Veefkind, “Kinetic Study of High-Pressure Pulverized Coal Char Combustion: Experiments and Modeling”, Fuel **76**, 945 (1997a).

Banin, V. E., F. A. C. M. Commissaris, J. H. J. Moors and A. Veefkind, "Kinetic Study of Pulverized Coal Combustion at High Pressure Using a Shock Tube", *Combustion and Flame*, **108**, 1 (1997b).

Bar-Ziv, E., D. B. Jones, R. E. Spjut, D. R. Dudek, A. F. Sarofim and J. P. Longwell, "Measurement of Combustion Kinetic of a Single Char Particle in an Electrodynamic Thermogravimetric Analyser", *Combustion and Flame*, **75**, 81 (1989).

Bateman, K. J., “Millimeter Sized Coal Particle Combustion at Elevated Pressures”, M.S. Thesis, Brigham Young University (1993).

Bateman, K. J., G. J. Germane, L. D. Smoot and C. N. Eatough, “A Facility for High-Pressure Measurement of Reaction Rates of Millimeter-Sized Coal,” *Energy and Fuels*, **9**, 295 (1995).

Bird, R. B., W. R. Stewart and E. N. Lightfoot, *Transport Phenomena*, John Wiley and Sons, New York (1960).

Bischoff, K. B., “Effectiveness Factor for General Reaction Rate Forms,” *A.I.Ch.E Journal,* **11**, 351 (1965).

Blyholder G. and H. Eyring, “Kinetics of Graphite Oxidation. II,” *J. Phys. Chem.*, **63**, 1004 (1959).

Carberry, J. J., *Chemical and Catalytic Reaction Engineering*, McGraw Hill, New York (1976).

Chan, M. L., K. N. Moody, J. R. Mullins and A. Williams, “Low Temperature Oxidation of Soot,” *Fuel*, **66**, 1695 (1987).

Chandler, J. P., Personal Communication to T. H. Fletcher, 1999.

Charpenay, S., M. A. Serio and P. R. Solomon, “The Prediction of Coal Char Reactivity Under Combustion Conditions,” *24th Symposium (International) on Combustion*, The Combustion Institute**,** Pittsburgh, PA, 1189 (1992).

Cope, R. F., C. R. Monson, G. J. Germane and W. C. Hecker, “Improved Diameter, Velocity, and Temperature Measurements for Char Particles in Drop-Tube Reactors,” *Energy and Fuels*, **8**, 925 (1994)

Cope, R. F., “Effects of Minerals on the Oxidation Rates of Beulah Zap Lignite Char,” Ph.D. Dissertation, Brigham Young University (1995).

Croiset, E., C. Mallet, J.-P. Rouan and J.-R. Richard, "The Influence of Pressure on Char Combustion Kinetics", *26th Symposium (International) on Combustion;* The Combustion Institute, Pittsburgh, PA, 3095 (1996).

Du, Z., A. F. Sarofim, J. P. Longwell and C. A. Mims, "Kinetic Measurement and Modeling of Carbon Oxidation", *Energy and Fuels*, **5**, 214 (1991).

Essenhigh, R. H., R. Froberg and J. B. Howard, “Combustion Behavior of Small Particles,” *Ind. Eng. Chem.*, **57** (9), 32 (1965).

Essenhigh, R. H. *Chemistry of Coal Utilization (Chapter 19)*; 2nd Suppl., M. A. Elliott, Ed.; Wiley, New York (1981).

Essenhigh, R. H., "An Integration Path for the Carbon-Oxygen Reaction with Internal Reaction", *22nd Symposium (International) on Combustion;* The Combustion Institute, Pittsburgh, PA, 89 (1988).

Essenhigh, R. H., "Rate Equation for the Carbon-Oxygen Reaction: An Evaluation of the Langmuir Adsorption Isotherm at Atmospheric Pressure", *Energy and Fuel*, **5**, 41 (1991).

Essenhigh, R. H. and A. M. Mescher, “Influence of Pressure on the Combustion Rate of Carbon,” *26th Symposium (International) on Combustion;* The Combustion Institute, Pittsburgh, PA, 3085 (1996).

Essenhigh, R. H., D. Fortsch and H. E. Klimesh, “Combustion Characteristics of Carbon: Influence of the Zone I – Zone II Transition on Burnout in Pulverized Coal Flames,” Energy and Fuels, **13**, 955 (1999).

Field, M. A., D. W. Gill, B. B. Morgan and P. G. W. Hawksley, *Combustion of Pulverized Coal*, BCURA, Leatherhead, England (1967).

Field, M. A., “Rate of Combustion of Sized-Graded Fractions of Char From A Low-Rank Coal between 1200 K and 2000 K,” *Combustion and Flame*, **13**, 237 (1969).

Fiveland, W. A. and A. S. Jamaluddin, “An Efficient Method for Predicting Unburned Carbon in Boilers,” *Combustion Science and Technology*, **81**, 147 (1992).

Fogler, H. S., *Elements of Chemical Reaction Engineering*, PTR Prentice Hall, Englewood Cliffs, New Jersey (1992).

Frank-Kamenetskii, D. A., *Diffusion and Heat Transfer in Chemical Kinetics*, Plenum Press, New York (1969)

Froment, G. F. and K. B. Bischoff, *Chemical Reactor Analysis and Design*ed, John Wiley and Sons, New York (1979).

Gale, T. K., T. H. Fletcher and C. H. Bartholomew, “Effects of Pyrolysis Conditions on Internal Surface Areas and Densities of Coal Chars Prepared at High Heating Rates in Reactive and Nonreactive Atmospheres,” *Energy and Fuels***,** **9**, 513 (1995).

Gray, D., J. G. Cogoli and R. H. Essenhigh, "Problems in Pulverized Coal and Char Combustion", *Advances in Chemistry Series*, **132**, 72 (1976).

Gunn, D. J., “Diffusion and Chemical Reaction in Catalysis and Adsorption,” *Chemical Engineering Science,* **22**, 1439 (1967).

Hill, C. G. J., *An Introduction to Chemical Engineering Kinetics and Reactor Design*, John Wiley ad Sons, New York (1977).

Hong, J., W. C. Hecker and T. H. Fletcher, “Improving the Accuracy of Predicting Effectiveness Factors for *m*-th Order and Langmuir Rate Equations in Spherical Coordinates,” *Energy and Fuels*, in press (2000a).

Hong, J, W. C. Hecker and T. H. Fletcher, “Modeling High Pressure Char Oxidation Using Langmuir Kinetics with an Effectiveness Factors,” In review, *28th Symposium (International) on Combustion,* The Combustion Institute, Pittsburgh, PA (2000b).

Hurt, R. H., D. R. Dudek, J. P. Longwell, A. F. Sarofim, “The Phenomenon of Gasification-Induced Carbon Densification and its Influence on Pore Structure Evolution,” *Carbon*, **26**, 433 (1988).

Hurt, R. H. and R. E. Mitchell, "On the Combustion of Heterogeneous Char Particle Population," *24th Symposium (International) on Combustion*, The Combustion Institute, Pittsburgh, PA, 1233 (1992a).

Hurt, R. H. and R. E. Mitchell, "Unified High Temperature Char Combustion Kinetics for a Suite of Coals of Various Rank," *24th Symposium (International) on Combustion*, The Combustion Institute, Pittsburgh, PA, 1243 (1992b).

Hurt, R. H., K. A. Davis, "Near-Extinction and Final Burnout in Coal Combustion", *25th Symposium (International) on Combustion*, The Combustion Institute, Pittsburgh, PA, 561-568 (1994).

Hurt, R. H., K. A. Davis, N. Y. C. Yang and J. R. Gibbins, "Residual Carbon from Pulverized-Coal-Fired Boilers: Particle Size Distribution and Combustion Reactivity", *Western States Sections/The Combustion Institute, 1994 Spring Meeting*, 91 (1994).

Hurt, R. H., M. M. Lunden, E. G. Brehob and A. J. Maloney, "Statistical Kinetics for Pulverized Coal Combustion," *26th Symposium (International) on Combustion*, The Combustion Institute, Pittsburgh, PA, 3169 (1996).

Hurt, R. H., "Structure, Properties, and Reactivity of Solid Fuels," *27th Symposium (International) on Combustion*, The Combustion Institute, Pittsburgh, PA, 2887 (1998a).

Hurt, R. H., J. K. Sun and M. Lunden, "A Kinetics Model of Carbon Burnout in Pulverized Coal Combustion," *Combustion and Flame* **113**, 181 (1998b).

Knudsen, M, *The Kinetic Theory of Gases: Some Modern Aspects*, John Wiley and Sons, New York (1950).

Laurendeau, N. M., "Heterogeneous Kinetics of Coal Char Gasification and Combustion," *Progress in Energy and Combustion Science,* **4**, 221 (1978).

Levenspiel, O., *The Chemical Reactor Omnibook*, OSU Book Stores, Inc., Corvallis, Oregon (1993).

Levenspiel, O., *Chemical Reaction Engineering (*3rd ed.), John Wiley and Sons, New York (1999).

Luss, D. and N. R. Amundson, "On a Conjecture of Aris: Proof and Remarks," *A.I.Ch.E. Journal*, **13**, 759 (1967).

Ma, J., "Soot formation during coal pyrolysis," Ph. D. Dissertation, Brigham Young University (1996)

Mehta, B. N. and R. Aris , “Communication on the Theory of Diffusion and Reaction-VII: The Isothermal p-th Order Reaction,” *Chemical Engineering Science,* **26**, 1699 (1971).

Mathias, J. A., "High Pressure Oxidation Rates for Large Particles,” Master Thesis, Brigham Young University (1996).

Mitchell, R. E., “A Theoretical Model of Chemically reacting Recirculating Flows,” Sandia Technical Report, SAND79-8236, Sandia National Laboratory, Livermore, CA (1980).

Mitchell, R. E., R. H. Hurt, L. L. Baxter and D. R. Hardesty, “Compilation of Sandia Coal Char Combustion Data and Kinetics Analyses: Milestone Report,” Sandia Technical Report, SAND92-8208, Sandia National Laboratory, Livermore, CA (1992).

Monson, C. R., “Char Oxidation at Elevated Pressures,” Ph.D. Dissertation, Brigham Young University (1992).

Monson, C. R. and J. G. Germane, “A High-Pressure Drop-Tube Facility for Coal Combustion Studies,” *Energy and Fuels,* **7**, 928 (1993).

Monson, C. R., G. J. Germane, A. U. Blackham and L. D. Smoot, “Char Oxidation at Elevated Pressure”, *Combustion and Flame,* **100**, 669 (1995).

Mulcahy, M. F. R. and I. W. Smith, “Kinetics of Combustion of Pulverized Fuel: A Review of Theory and Experiment,” *Reviews of Pure and Applied Chemistry,* **19**, 81 (1969).

Niksa, S. and R. H. Hurt, “Predicting the Complete Combustion Histories of Individual Particles of Any Coal Type,” *Proceeding of the Tenth International Conference on Coal Science*, **1**, 487 (1999).

Patankar, S. V., *Numerical Heat Transfer and Fluid Flow*, Taylor and Francis, New York (1980).

Peterson, E. E., “Reaction of Porous Solids,” *A.I.Ch.E. Journal,* **3**, 443 (1957).

Ranish, J. M. and P. L. Walker, Jr., “High Pressure Studies of the Carbon-Oxygen Reaction”, *Carbon*, **31**, 1, 135 (1993).

Ranz, W. E. and W. R. Marshall, Jr., “Evaporation from Drops,” *Chem. Eng. Prog.,* **48**, 141, 173 (1952).

Reade, W. C., K. W. Morris, and W. C. Hecker, “Modeling the Effects of Burnout on High-Temperature Char Oxidation,” *Coal Science and Technology*, **24,** 639 (1995)

Reade, W., "An Improved Method for Predicting High-Temperature Char Oxidation Rates," M.S. Thesis, Brigham Young University (1996)

Roberts, G. W. and C. N. Satterfield, "Effectiveness Factor for Porous Catalysts," *Ind. Eng. Chem. Fundamentals,* **4**, 288 (1965).

Rosa, J. O. M., T. V. Carcia and J. A. O. Tapia, "Evaluation of Isothermal Effectiveness Factor for Nonlinear Kinetics Using an Approximate Method," *Ind. Eng. Chem. Res.*, **37**, 3780 (1998).

Schneider, P. and P. Mitschka, "Effect of Internal Diffusion on Catalytic Reactions," *Chemical Engineering Science*, **21**, 455 (1966).

Simons, G. A., "The Role of Pore Structure in Coal Pyrolysis and Gasification," *Prog. Energy Combust. Sci.*, **9**, 269 (1983).

Smith, I. W., "The Combustion of Coal Char: A Review", *11th Symposium (International) on Combustion*, The Combustion Institute, Pittsburgh, PA, 1045 (1982).

Smith, J. M., *Chemical Engineering Kinetics*, McGraw Hill, New York (1981).

Smith, K. L., L. D. Smoot, T. H. Fletcher and R. J. Pugmire, *The Structure and Reaction Processes of Coal*, Plenum Press, New York (1994).

Smoot, L. D. and P. J. Smith, *Coal Combustion and Gasification*, Plenum Press, New York and London (1985).

Sun, J. K. and R. Hurt, "Mechanism of Extinction and Near-Extinction in Solid Fuel Combustion," In review, 28th *Symposium (International) on Combustion*, The Combustion Institute, Pittsburgh, PA (1999)

Suuberg, E. M., M. Wojtowicz and J. M. Calo, "Reaction Order for Low Temperature Oxidation of Carbon," *22nd Symposium (International) on Combustion*, The Combustion Institute, Pittsburgh, PA, 79 (1988).

Suuberg, E. M., *Fundamental Issues in Control of Carbon Gasification Reactivity*, Kluwer Academic Publishers, Dordrecht (1991).

Szekely, J. and J. W. Evans, "A Structural Model for Gas-Solid Reactions with a Moving Boundary - I", *Chemical Engineering Science*, **25**, 1901 (1970).

Szekely, J. and J. W. Evans, "A Structural Model for Gas-Solid Reactions with a Moving Boundary - II: The Effect of Grain Size, Porosity and Temperature on the Reaction of Porous Pellets", *Chemical Engineering Science*, **26**, 1901 (1971).

Szekely, J. and M. Propster, "A Structural Model for Gas Solid Reactions with a Moving Boundary - VI: The Effect of Grain Size Distribution on the Conversion of Porous Solids", *Chemical Engineering Science*, **30**, 1049 (1975).

Thiele, E. W., "Relation between Catalytic Activity and Size of Particle," *Ind. Eng. Chem.*, **31**, 916 (1939).

Thring, M. W. and R. H. Essenhigh, "Thermodynamics and Kinetics of Combustion of Solid Fuels," *Chemistry of Coal Utilization*, H. H. Lowry (Ed), Supplementary volume, p.892, Wiley, New York (1963).

Tognotti, L., J. P. Longwell and A. F. Sarofim, "The Products of the High Temperature Oxidation of a Single Char Particle in an Electrodynamic Balance," *23rd Symposium (International) on Combustion*, The Combustion Institute, Pittsburgh, PA, 1207 (1990).

Tseng, H. P. and T. F. Edgar, "Combustion Behavior of Bituminous and Anthracite Coal Char between 425 and 900 °C," *Fuel*, **64**, 373 (1985).

Tyson, S. and T. Blackstock, *Unburned Carbonaceous Material on Utility Fly Ash Conference*, U.S. DOE PETC, Pittsburgh (1995).

Villadsen, F. and M. L. Michelsen, *Solution of Differential Equation Models by Polynomial Approximation*, Prentice-Hall, Englewood Cliffs (1978).

Walker, P. L. Jr., F. J. Rusinko and L. G. Austin, "Gas Reactions of Carbon", *Advances in Catalysis*, **11**, 133 (1959).

Wakao, N and J. M. Smith, "Diffusion in Catalyst Pellets," *Chem. Eng. Sci.*, **17**, 825 (1962).

Wedel, S. and D. Luss, "A Rational Approximation of the Effectiveness Factor," *Chem. Eng. Commum.*, **7**, 245 (1980).

Wheeler, A., *Advances in Catalysis*, Academic Press, Inc., New York (1951).

White, W. E., C. H. Bartholomew, W. C. Hecker and D. M. Smith, *Adsorption Sci. Technol.*, **7**, 180 (1991).

Appendices

Appendix A: Experiments

Introduction

The properties of char are dependent on preparation conditions, such as temperature, heating rate, and oxygen and steam concentrations. In particular, questions have arisen in the literature regarding the comparison of high temperature char oxidation rates obtained in flat-flame burner experiments versus rates obtained in drop tube and other reactors. The purpose of this experimental work is to explore how steam and oxygen concentrations affect the properties of char, such as N_2 surface area, CO_2 surface area, apparent density, true density, and most important of all, TGA reactivity and high temperature reactivity. The work in this appendix was performed in a one-year contract (No. DE-AC21-93MC30040) with U.S. Department of Energy (DOE) and the Advanced Fuel Research (AFR). This work appears in the appendix to preserve the modeling focus in the main text of this dissertation.

Chars were prepared in a flat-flame reactor under four different conditions, varying post-flame steam and oxygen concentrations. To determine the effects of ambient steam concentration on the char properties, chars were produced in the post-flame products of: 1) a flame using CH_4 as the principal fuel, and 2) a flame using CO as the principal fuel. The post-flame steam concentration was reduced substantially when CO was used as the principal fuel. To determine the effects of ambient oxygen concentration on char properties, chars were produced under both fuel-lean and fuel-rich flat-flame conditions for both fuels (CO and CH_4), hence four separate reactor conditions were used.

Two South African coals, Koonfontain and Middleburg, were selected to study the effects of steam and oxygen concentration in the preparation environment on char properties. These two coals were pulverized and sieved to 45-75 μm at BYU. In addition, chars from two Chinese coals (Yang Quan and Han Cheng), a South American coal (Cerrejon), and an American coal (Pittsburgh) were prepared under the methane fuel-lean condition. These additional coals were pulverized and sieved by the Vortec Corporation before they were received at BYU.

Experimental Technique

Flat-Flame Burner Considerations

Char oxidation experiments have been performed in flat-flame burners by many investigators, since this kind of reactor permits chars to be prepared at the high heating rates (~10^5 K/s) and high temperatures (1500 to 2000 K) typical of industrial pulverized coal-fired boilers (Ma, 1996). A schematic of the BYU flat-flame burner and the particle collection and separation system are shown in Figure A.1. Flat-flame burner (FFB) experiments are generally performed using a $CH_4/H_2/O_2/H_2$ flame. The H_2 is added to stabilize the flame structure, and the flow rates of all species are also adjusted to obtain the desired gas temperature profile, post-flame oxygen concentration, and velocity. Flame stability is essential, since acoustic waves can affect particle combustion, and non-uniform gas temperature profiles can also adversely affect results. For example, at excessively fuel-rich conditions, additional hydrogen can destabilize the flame, either by detaching the flame from the burner base, or by making noise (acoustic oscillations), which may be destructive to the facility, annoying to operators, and causing enhanced particle oxidation rates due to pulsed combustion effects. Without hydrogen, CO flames are never flat, since the OH radical is essential to rapid combustion of CO. Dilution nitrogen is added into the fuel to lower the post-flame gas temperature and to increase the total flow rate (and thus increase velocity of particles and reduce the residence time).

Reactor Conditions

The CH_4 fuel-rich operating condition for the flat-flame burner was taken from the condition used by Ma (1996). The total flow rate for this case was about 50 slpm. The maximum post-flame gas temperature along the reactor centerline was reported to be about 1650 K, and the equivalence ratio was about 1.5.

To study the effects of oxygen on char properties, fuel-lean conditions were used while maintaining similar total flow rates and post-flame temperature profiles along the centerline of the quartz tower. Under these conditions, complete devolatilization occurred before the one inch sampling height. The post-flame gas temperatures were measured at reaction lengths of 0.25, 0.50, 0.75 and 1 inch along the centerline of the quartz tower using a type B thermocouple with a silica-coated bead of 0.7 mm diameter. The average of these four temperatures was kept as close as possible to that of the fuel-rich CH_4 condition. Since the total flow rate and the temperature profile of the gas were maintained, the velocity and residence time of the particles were also close to those obtained for the fuel-rich CH_4 condition.

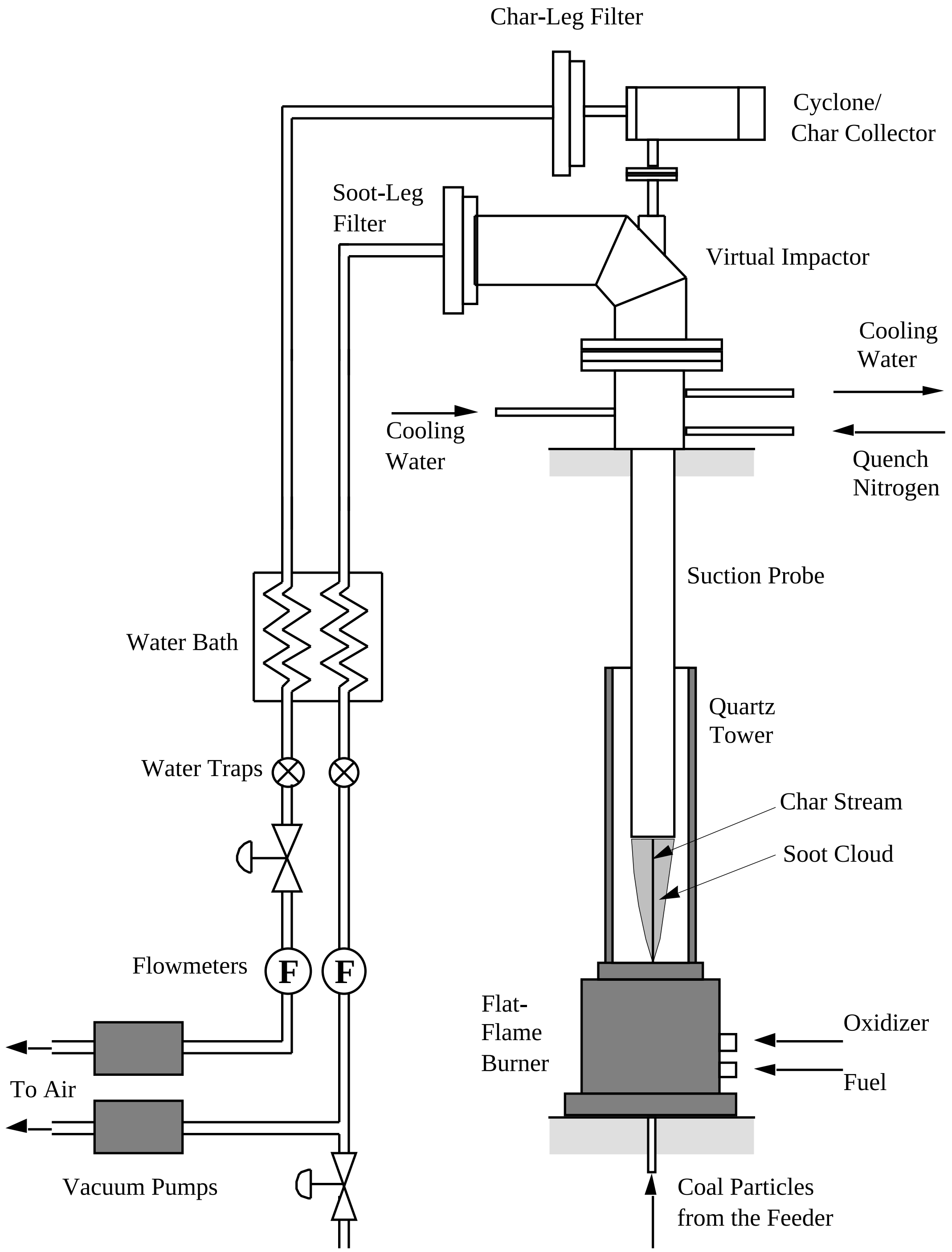

Figure A.1. Schematic of the flat-flame burner and the particle collection and separation system.

To study the effects of steam, CO was used in the place of methane, while again maintaining the total flow rate and temperature profile in the first inch after the injection. Typical methane flames produce 16-25 mole-% steam in the post-flame gases. CO is an ideal alternative fuel to reduce steam in the post-flame gases, but as mentioned above, some hydrogen is necessary to stabilize the CO flame. Therefore, a total absence of steam in the post-flame gases was not possible. However, by using CO as the fuel, the steam concentration was reduced from about 17 mole-% to less than 1 mole-%.

The four different char preparation conditions are described in Table A.1, and the measured temperature profiles for these conditions are given in Table A.2.

Table A.1. Reactor Conditions Used

Condition number	#1	#2	#3*	#4
Condition name	CH_4 fuel-rich	CH_4 fuel-lean	CO fuel-rich	CO fuel-lean
CH_4 (slpm)	4.84	1.52	0	0
CO (slpm)	0	0	16.9	6.41
H_2 (slpm)	2.79	4.63	0.37	2
N_2 (slpm)	5.41	0	6.46	0
Air (slpm)	38.6	43.7	21.0	40.7
Total flow rate (slpm)	51.6	49.9	44.8	49.1
Quench nitrogen (slpm)	65	65	65	65
Carrier nitrogen (slpm)	0.037	0.037	0.037	0.037
Equivalence ratio	1.37	0.58	1.96	0.49
Post-flame H_2O (mole-%)	17.1	16.1	0.69	4.45
Post-flame O_2 (mole-%)†	0	8.0	0	9.6

* Flow rates in condition #3 were measured with rotameters while those in other conditions were measured with mass flow meters.

† Post-flame H_2O and O_2 mole fractions were calculated using EDWRDS code at 1600 K.

Table A.2. Measured Centerline Reactor Temperatures

Condition number	#1	#2	#3	#4
Condition name	CH_4 fuel-rich	CH_4 fuel-lean	CO fuel-rich	CO fuel-lean
Height Above Burner	Gas Temperature Profile (K)*			
0.25	1542	1677	1650	1718
0.50	1637	1628	1687	1670
0.75	1640	1608	1703	1647
1.00	1644	1592	1696	1630

* Measured along reactor centerline, corrected for radiation loss.

Procedures and Apparatus

Char Preparation

Coal particles were injected through the flame, reacted, captured by a suction probe at a certain distance away from the injection point, quenched by nitrogen in the probe tip, and separated from the soot and the gas in a virtual impactor and cyclone system. The distance between the injection point and the suction probe (called the reaction length or sampling height) was set to one inch for most of the experiments, corresponding to a residence time of 14 ms. Studies of Koonfontain char were also made at the methane fuel-lean condition at increased residence times by sampling at heights of 2, 4, and 6 inches (corresponding to about 25, 44, and 63 ms, respectively).

The particle residence time as a function of sampling height was measured for several different coals with a high-speed video camera by Ma (1996). The residence time was found to be dependent on the gas temperature profile and the total flow rate through the reactor, but almost independent on the coal type. The total flow rate and gas temperature profile were therefore kept very similar from one reactor condition to another in order to achieve similar particle residence times. In this project the particle residence times at heights of 1, 2, 4, and 6” are taken as 14, 25, 44, and 63 ms respectively, which are the values measured by Ma (1996).

Proximate and Ultimate Analysis

ASTM standard procedures were followed for the moisture, ash and volatile measurements in the proximate analysis. Volatile content measurements were only performed for the parent coals, since complete devolatilization was achieved in the chars. Moisture and ash contents were measured for chars and the their parent coals before the ICP tracer analysis was performed in order to obtain the mass release of the chars.

CHNS data were measured on a dry basis, then converted to dry ash free (daf) basis using the ash contents measured in the proximate analysis. Oxygen concentrations (daf) were calculated by difference: O% = 100% - (C% + H% + N% + S%). A Leco CHNS analyzer (model 932) was used to perform the CHNS analysis.

Internal Surface Area

Nitrogen BET multi-point surface area and carbon dioxide surface area (0°C) were measured for all chars using a Micromeritics Gemini 2360 instrument.

TGA Reactivity

The reactivities of chars were measured in a Perkin Elmer thermogravimetric analyzer (model 7) at 550 °C in a gas flow of 10% oxygen and 90% nitrogen.

Bulk Density and True Density

To obtain the bulk density of a coal or char, the coal or char sample was weighed using a microbalance and put into a graduated cylinder, which was then tapped until the volume of the sample did not change. The bulk density (also called tap density) is the weight of the sample divided by the volume displaced by the sample, where the volume includes micro- and macro-pores and inter-particle voids. Apparent densities were calculated from the bulk density, ρ_b, by:

$$\rho_{app} = \frac{\rho_b}{1 - \varepsilon_{bv}} \tag{A.1}$$

where ε_{bv} is the fraction of inter-particle void volume in the char bed, usually taken as 0.45 (White *et al.*, 1995). True densities were measured in a Quanta Chrome helium micro-pycnometer (model MPY-2).

High Temperature Reactivity

The temperature profiles at the centerline of the FFB tower were measured for conditions #2 and #4 at extended sampling heights. These two measured temperature profiles were very similar at each sampling height. The difference between the two temperature profiles at any reaction height was usually about 7 K, and never greater than 50 K. Some of the differences observed in the measured temperature profiles were due to (a) the uncertainty of the thermocouple bead position (vertical and horizontal), and (b) the non-steady heat-up effects of the tower.

Koonfontain chars were collected at heights of 1”, 2”, 4”, and 6” under these two conditions. The daf mass release data for these chars were determined by ICP tracer analysis. The char reactivities (in gram C/gram C remaining/second) between 1” and 2”, 2” and 4”, 4” and 6” were calculated. These reactivities were then converted to reactivities based on external surface area using apparent densities calculated from the tap densities of these chars. Several assumption are made during the conversion of reactivities: 1) The sizes of the original coal particles range from 45 to 75 μm. The distribution of particle size is neglected and the diameter of coal particle is taken as the arithmetic mean of the lower and upper limits, 60 μm. 2) Fragmentation of coal or char particle during devolatilization or char oxidation is neglected. 3) In the calculation of the χ factor (actual reaction rate/the maximum possible rate dictated by diffusion), CO is assumed as the only surface product of the carbon-oxygen reaction, and the Sherwood number is taken as 2. 4) The average diameters of chars are calculated using the following equation:

$$\frac{m}{m_o} = \frac{\rho}{\rho_o}\left(\frac{d}{d_o}\right)^3 \tag{A.2}$$

where m, ρ and d are the mass (including moisture and ash), apparent density and average diameter of a char, respectively, while m_o, ρ_o and d_o are the mass (including moisture and ash), apparent density and average diameter of its parent coal, respectively.

Results

The results of proximate and ICP tracer analysis are listed in Tables A.3-A.6. The results of elemental analysis are listed in Tables A.7-A.9. Bulk densities, true densities, and surface areas are listed in Table A.10.

Table A.3. Proximate Analysis for All Coals

Coal	Moisture (wt% as received)	Ash (wt% dry)	Volatiles (wt% dry)
Koonfontain	0.82	12.24	25.79
Middleburg	0.86	8.79	33.67
Han Cheng	0.41	29.79	15.21
Yang Quan	4.39	10.73	36.78
Pittsburgh	1.28	11.01	37.64
Cerrejon	2.11	6.81	38.58

Table A.4. Moisture, Ash and ICP Mass Release Data for Koonfontain and Middleburg Chars at the 1" Sampling Height (14 ms)

	Koonfontain				Middleburg			
Reactor condition	#1	#2	#3	#4	#1	#2	#3	#4
Sampling height	1”	1”	1”	1”	1”	1”	1”	1”
Moisture (wt% as rec'd)	0.24	0.17	0.36	0.16	0.89	0.20	0.54	0.30
Ash (wt% dry)	18.91	20.52	18.69	20.63	16.02	16.64	15.66	17.25
Mass release (daf) for different tracers								
Ti	40.77	47.12	40.75	47.75	49.89	52.02	48.39	53.60
Si	42.35	47.35	40.48	48.80	48.33	50.62	46.88	52.59
Al	41.61	46.68	39.97	47.88	49.32	51.83	47.10	52.94
ash	40.19	45.97	39.32	46.35	49.51	51.76	48.13	53.80
Mass balance*	46.5	49.0	43.7	49.2	54.3	54.1	51.9	55.0

* Mass balance means the mass release of the char is calculated from the amount of char collected and the amount of coal fed.

Table A.5. Moisture, Ash and ICP Mass Release Data for Koonfontain Chars at Greater Sampling Heights

Name of coal	Koonfontain					
Reactor condition	#2	#2	#2	#4	#4	#4
Sampling height	2”	4”	6”	2”	4”	6”
Residence time (ms)	25	44	63	25	44	63
Moisture (wt% as rec'd)	0.483	0.176	0.465	0.317	0.548	0.478
Ash (wt% dry)	20.55	21.72	23.18	20.95	23.94	26.24
Mass release (daf) for different tracers						
Ti	49.19	51.16	53.95	49.65	57.65	61.95
Si	69.54†	70.86†	73.01†	49.32	58.27	62.07
Al	47.04	50.76	54.38	48.13	57.87	61.99
ash	45.76	49.45	53.51	48.11	56.32	61.35
Mass balance*				50.7	58.7	64.3

† Suspect data

* Mass balance means the mass release is based on the amount of coal fed and the amount of char collected in the experiment.

Table A.6. Moisture, Ash and ICP Mass Release Data for Four Chars Prepared under CH_4 Fuel-lean Condition (at the 1" sampling height)

Name of coal	Cerrejon	Yan Quan	Pittsburgh	Han Cheng
Moisture (wt% as rec'd)	0.27	0.40	0.39	0.00
Ash (wt% dry)	14.03	23.41	23.86	36.68
Mass release (daf) for different tracers				
Ti	56.52	62.80	61.84	28.98*
Si	57.23	63.63	62.17	20.90*
Al	58.15	62.55	63.53	28.86*
ash	55.18	60.66	60.49	27.38*
Mass balance	61.5	63.7	77.0	66.3

* Suspect data

Table A.7. Elemental Analyses of Middleburg Coal and Chars (1" sampling height)

		C%	H%	N%	S%	Sum	O%(dif)	H/C
Coal	dry	75.33	4.92	1.643	0.501	82.4		0.784
	daf	82.59	5.40	1.80	0.55	90.3	9.66	
Char 1	dry	78.88	1.39	1.568	0.309	82.1		0.214
	daf	93.93	1.58	1.79	0.35	93.6	6.40	
Char 2	dry	79.84	0.80	1.501	0.310	82.4		0.120
	daf	95.77	0.96	1.80	0.37	98.9	1.10	
Char 3	dry	78.58	1.78	1.652	0.306	82.3		0.272
	daf	93.17	2.11	1.96	0.36	97.6	2.39	
Char 4	dry	80.56	0.63	1.535	0.271	83.0		0.094
	daf	97.36	0.76	1.85	0.33	100.3	-0.30*	

*Negative value for oxygen concentration by difference due to errors in CHNS and ash analyses.

Table A.8. Elemental Analyses of Koonfontain Coal and Chars (1" sampling height)

		C%	H%	N%	S%	Sum	O%(dif)	C/H
Coal	dry	72.02	4.27	1.83	0.56	78.7		0.712
	daf	82.07	4.86	2.09	0.64	89.7	10.35	
Char 1	dry	75.26	1.47	1.60	0.33	78.7		0.234
	daf	92.81	1.81	1.98	0.41	97.0	2.99	
Char 2	dry	80.07	0.58	1.52	0.28	82.7		0.087
	daf	100					*	
Char 3	dry	76.23	1.85	1.74	0.31	80.1		0.291
	daf	93.75	2.28	2.14	0.39	98.6	1.55	
Char 4	dry	78.29	0.55	1.51	0.29	80.6		0.084
	daf	98.65					*	

***** Negative **%**O.

Table A.9. Elemental Analyses of Four Coals and Their Chars Prepared at CH_4 Fuel-lean Condition

		C%	H%	N%	S%	Sum	O%(dif)	C/H
Yan Quan coal	dry	70.42	4.75	1.24	0.573			0.810
	daf	78.89	5.32	1.39	0.642	86.24	13.76	
Yuan Quan char #2	dry	83.86	0.99	1.19	1.16			0.142
	daf						*	
Cerrejon coal	dry	75.73	5.21	1.64	1.14			0.825
	daf	81.26	5.59	1.76	1.22	89.83	10.17	
Cerrejon char #2	dry	85.97	0.69	1.69	0.70			0.096
	daf						*	
Han Cheng coal	dry	59.83	3.13	1.16	2.34			0.629
	daf	85.21	4.46	1.65	3.34	94.66	5.34	
Han Cheng char #2	dry	62.46	0.50	1.00	0.77	64.73		0.096
	daf						*	
Pittsburgh coal	dry	72.09	4.87	1.55	5.29			0.810
	daf	81.01	5.48	1.76	5.94	94.17	5.83	
Pittsburgh char #2	dry	71.80	0.63	1.35	4.24			0.105
	daf	94.30	0.825	1.77	5.56	102.5	*	

* Negative %O by difference.

Table A.10. Densities, Surface Areas and Calculated Average Diameters of Coals and Chars

	Bulk density (g/cm^3)	True density (g/cm^3)	N_2 BET multi-point surface area	CO_2 surface area	Calculated average diameters
Koonfontain coal	0.768	1.49			60
Char #1 @1"	0.453	1.98	238.5	378.5	61.73
Char #2 @1"	0.429	1.99	89.4	301.9/290.2**	60.98
Char #3 @1"	0.427	1.72	231.2	372.2	62.96
Char #4 @1"	0.424	2.07	79.4	313.1	61.03
Middleburg coal	0.624	1.38			60
Char #1 @1"	0.432	1.87	147.2	306.8	55.40
Char #2 @1"	0.400	1.84	64.9/71.2	239.3/248.3	56.16
Char #3 @1"	0.418	1.68	176.3	306.9	56.48
Char #4 @1"	0.400	1.89	86.3/75.4	255.0/252.7	55.64
Han Cheng char #2	0.443	1.91	26.5	94.0	
Yang Quan char #2	0.265	1.61	107.7	332.7	
Pittsburgh char #2	0.427	1.78	67.4	242.9	
Cerrejon char #2	0.377	1.48	60.8	254.3	
Koonfontain char #2 @2”	*	*	61.3	233.4	61.11
Koonfontain char #2 @4”	0.377	1.82	61.7	221.2	62.42
Koonfontain char #2 @6”	0.377	1.57	83.6/79.5	216.2	61.35
Koonfontain char #4 @2”	0.418	*	58.8	220.2	60.96
Koonfontain char #4 @4”	0.368	1.58	49.0	184.7	60.58
Koonfontain char #4 @6”	0.365	1.52	49.4	179.5	59.18

* Not available.
**83.6/79.5 means values of two replicates with different samples. This notation applies to all other cells in this table.

Discussion

The effects of oxygen concentration in the char preparation environment can be identified by comparing the properties of char #2 (CH_4, fuel-rich) with those of char #1 (CH_4, fuel-lean), and by comparing properties of char #4 (CO, fuel-rich) with those of char #3 (CO, fuel-lean). Similarly, the effects of steam concentration in the preparation environment can be identified by comparing the properties of char #3 (CO, fuel-lean) with those of char #1 (CH_4, fuel-lean) and by comparing the properties of char #4 (CO, fuel-rich) with those of char #2 (CH_4, fuel-rich). Note that in these four conditions the temperature profile of the post-flame gases and the residence time of the particles are kept relatively constant from condition to condition.

Mass Release

The mass release of char is commonly normalized by the original mass of the coal on a dry, ash-free (daf) basis. The mass release is determined by assuming mass conservation of one of the following elements or material: Al, Ti, Si, and ash. It can also be determined by overall mass balance, i.e., by the amount of char collected and the amount of coal fed in the experiment. In this project the mass release of a char is determined using all five of these methods. In most cases, these five methods produced relatively consistent values of mass release. In this analysis, the average values of the mass releases based on Ti and Al conservation were used for the calculation of the high temperature reactivity of Koonfontain chars made under conditions #2 and #4, since the mass releases based on Si were sometimes subject to question.

The mass release data from Table A.4 are plotted in Figure A.2. It can be seen that for both Koonfontain and Middleburg coals, the mass release of char #2 (CH_4, fuel-lean) is higher than that of char #1 (CH_4, fuel-rich), and the mass release of char #4 (CO, fuel-lean) is higher than that of char #3 (CO, fuel-lean). In other words, the presence of oxygen in the preparation environments increases the mass release of the char, as expected due to the initiation of char oxidation in the fuel-lean reactor conditions.

The decrease of steam concentration did not seem to affect mass release of chars in fuel-lean conditions (#3 vs. #1), but seemed to decrease mass release slightly in fuel-rich conditions (#4 vs. #2).

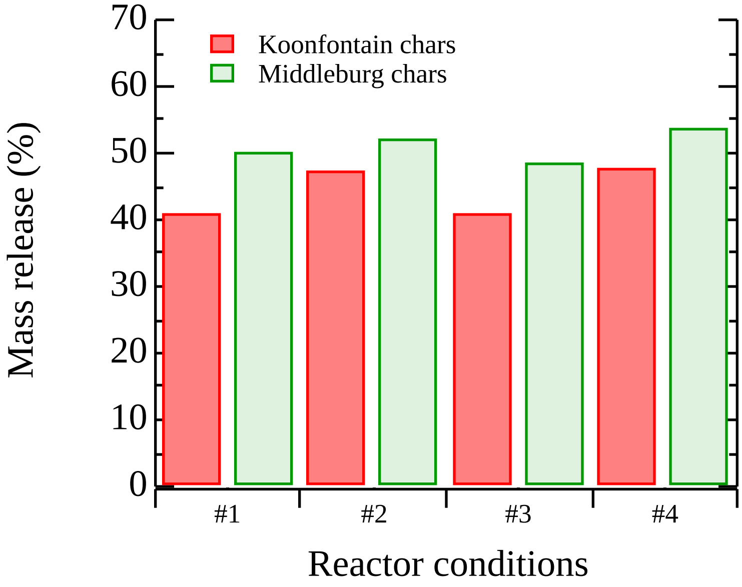

Figure A.2. Mass releases of the Koonfontain and Middleburg chars prepared at four different reactor conditions.

Tap Densities and True Densities

The bulk densities in Table A.10 were converted to apparent densities using Eq. A.1 (White *et al.*, 1991) and shown in Figure A.3. It can be seen that the presence of oxygen in the char preparation environment slightly decreases the bulk densities of both Koonfontain and Middleburg chars (#2 vs. #1, #4 vs. #3), and that steam also has only a slight effect on the bulk density of either Koonfontain or Middleburg chars (#1 vs. #3, #2 vs. #4).

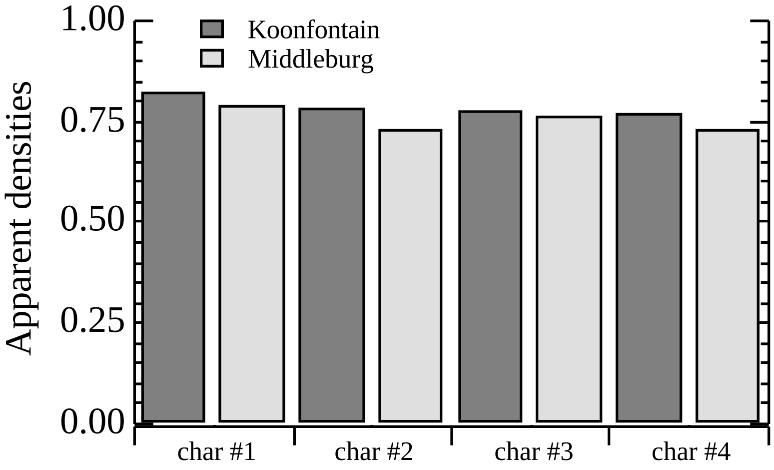

Figure A.3. The apparent densities of Koonfontain and Middleburg chars prepared at four different conditions and collected at 1”.

The true densities of both Koonfontain and Middleburg chars in condition #3 are lower than in the other conditions (see Table A.10). The reason for this decrease is not clear. Part of this disagreement may be due to the unstable readings of the pycnometer used in this project, but the fact that both coals showed the same relative behavior seems more than coincidental.

N_2 BET Surface Area and CO_2 Surface Area

The N_2 BET surface areas and CO_2 surface areas of the Koonfontain and Middleburg chars (see Table A.10) are plotted in Figures A.4 and A.5. These figures show that the presence of oxygen in the char preparation environment (#2 vs. #1, #4 vs. #3) reduces both N_2 BET surface area and CO_2 surface area of each char for both coals, and that the reduction of the N_2 BET surface area is much more marked than that of CO_2 surface area. This implies that the presence of O_2 affects the pores of intermediate size (mesopores) rather than those of small size (micropores). The effect of the reduced steam concentration on N_2 BET surface area and CO_2 surface area is not obvious, except that the Middleburg char #3 has a 20% higher N_2 BET surface area than the Middleburg char #1.

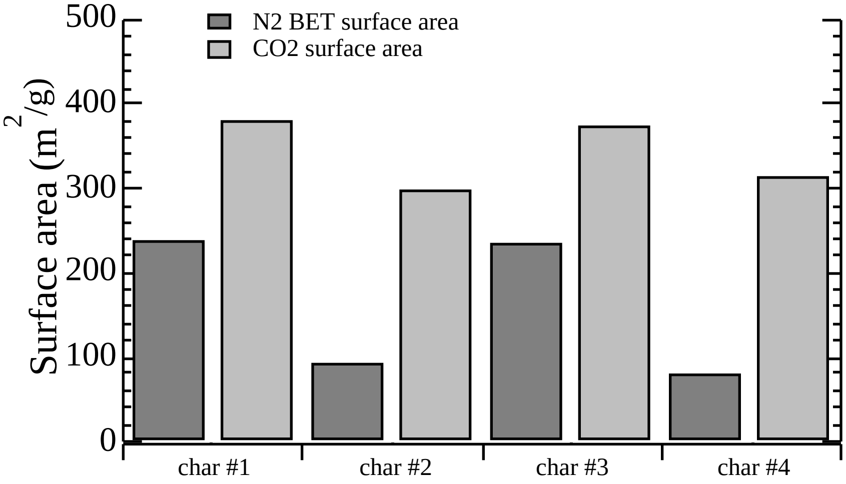

Figure A.4. Surface areas of Koonfontain chars obtained in four different reactor conditions

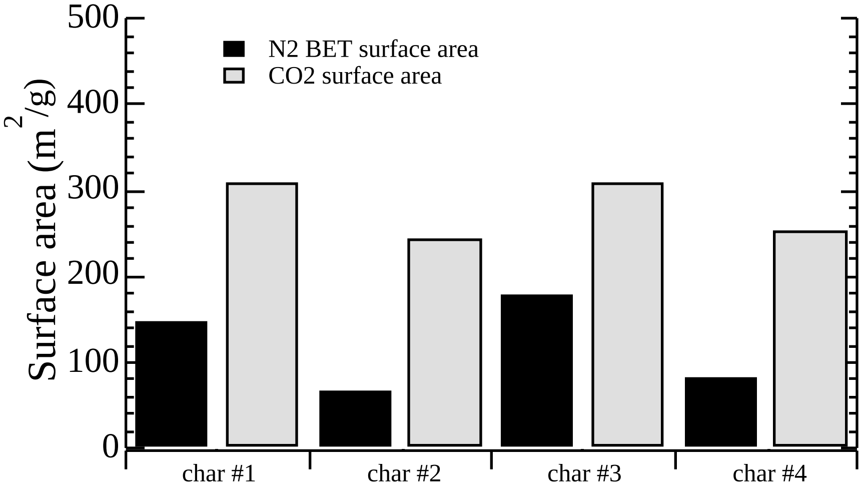

Figure A.5. Surface areas of Middleburg chars obtained in four different reactor conditions.

This observation is somewhat surprising, since Gale *et al.* (1995) performed experiments to show that the presence of steam in high heating rate experiments (drop tubes and FFB's) significantly increased the N_2 BET surface areas of chars prepared in such reactors. Reasons for this seeming discrepancy are not clear at this time.

TGA Reactivities: Effects of Reactor Conditions

The reactivities of Koonfontain chars and Middleburg chars prepared in these four conditions were measured using a thermogravimetric analyzer (TGA) at 550 º C in 10% oxygen. The results are shown in Figure A.6 and Figure A.7.

Figure A.6 indicates that the Koonfontain char #2 and char #4 collected at 1 inch have similar TGA reactivities; char #1 and char #3 collected at 1 inch also have similar TGA reactivities. However, chars #1 and #3 have higher TGA reactivities than chars #2 and #4. This means that the presence of oxygen in the preparation environment reduces the TGA reactivity of the char. The effect of reduced steam concentration in the char preparation environment is not significant for the Koonfontain chars. Similar trends with post-flame O_2 environment are observed for the Middleburg chars, except that char #3 has notably higher reactivity than that of char #1, indicating an effect of post-flame steam concentration for this coal. This is consistent with the fact that char #3 has higher N_2 BET surface area than char #1. The reason why the reduced steam concentration affects the N_2 BET surface area and TGA reactivity of the Middleburg char, but not the same properties of the Koonfontain char, is not clear at this point.

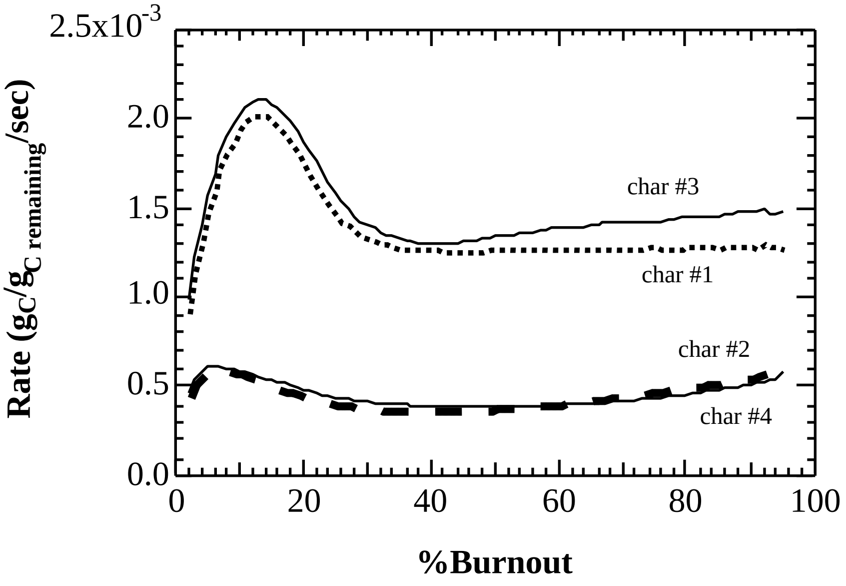

Figure A.6. TGA reactivities of Koonfontain chars (at 1” sampling height) obtained at 550 °C in 10 mole-% O_2.

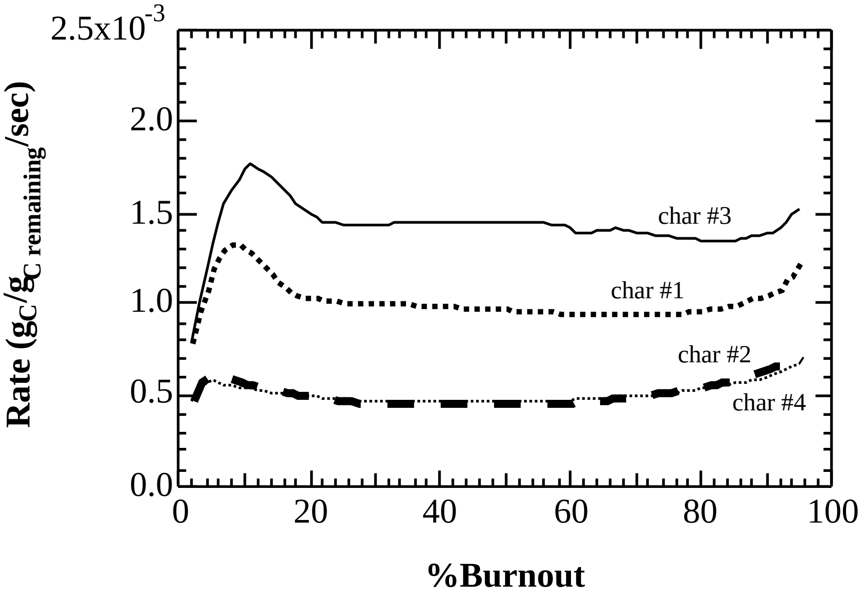

Figure A.7. TGA reactivities of Middleburg chars (at 1” sampling height) obtained at 550 °C in 10 mole-% O_2.

It is interesting to compare Figures A.4 and A.6; the TGA reactivities (the steady part of the curve) of Koonfontain chars are proportional to their N_2 BET surface areas, but poorly correlated to their CO_2 surface areas. From Figure A.5 and A.7, the variations of TGA reactivities of Middleburg chars are also well correlated to their N_2 BET surface areas but are weakly correlated to their CO_2 surface areas.

It is believed that the N_2 BET surface area represents the mesopore surface area while CO_2 surface area represents the micropore surface area (Gale *et al.*, 1995). Internal surface area is not accessible to oxygen unless the feeder pore is big enough or the reaction is slow enough to allow oxygen to penetrate the pores before it is consumed (Laurendeau, 1978). It is generally accepted that at typical TGA temperatures, the burning rate of char particles is slow enough to allow complete penetration of oxygen into all the pore structures and onto all the surface area in the particles. The data produced by this project seem to suggest:

1. At the temperature of the TGA experiments, all the surface area contributed by the mesopores is accessible to oxygen, but not all the surface area contributed by micropores is accessible.
2. In Zone I, oxygen completely penetrates bigger pore structures so that from a macroscopic perspective, a particle burns uniformly throughout the whole particle. However, oxygen fails to penetrate smaller pore structures, so that from a microscopic perspective the burning of the particle is not uniform. That is to say, complete oxygen penetration is a relative term; it occurs only for pore structures bigger than a certain size. The relative nature of complete oxygen penetration, if further substantiated, would imply that the activation energies measured in TGA

experiments (and reported by many researchers as true activation energies) are actually still coupled with mass diffusion effects in the micropores.

TGA Reactivities: Effects of Coal Types

Chars were prepared from all six parent coals (Koonfontain, Middleburg, Cerrejon, Yang Quan, Pittsburgh, and Han Cheng coals) under CH_4 fuel-lean condition at 1” sampling height. The TGA reactivities of these chars were measured at 550 °C in 10 mole-% O_2 and plotted in Figure A.8.

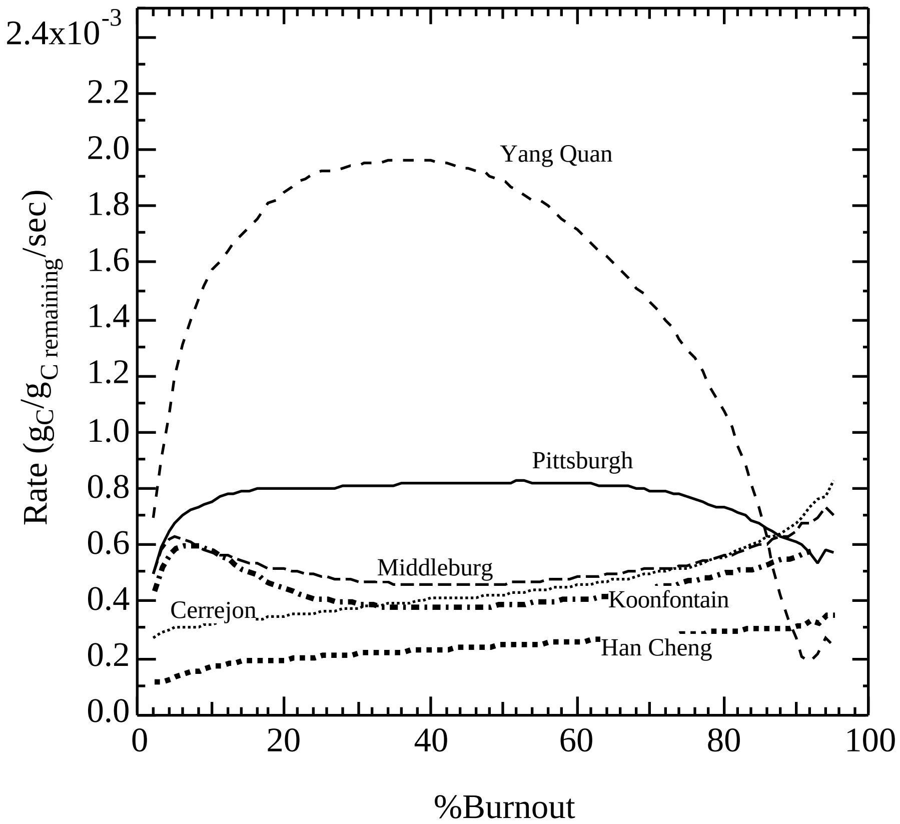

Figure A.8. TGA reactivities of all chars (prepared under CH_4 fuel-lean condition, collected at 1” sampling height) measured at 550 C in 10 mole-% oxygen.

The N_2 BET surfacea areas and H/C ratios of these chars are plotted in Figure A.9. The chars are in the order of decreasing TGA reactivity from left to right in Figure A.9. It can be seen that the N_2 surface areas and H/C ratios tend to decrease from left to right with a few exceptions. This means TGA reactivities are correlated with N_2 surface areas and H/C ratios even for chars of different parent coals.

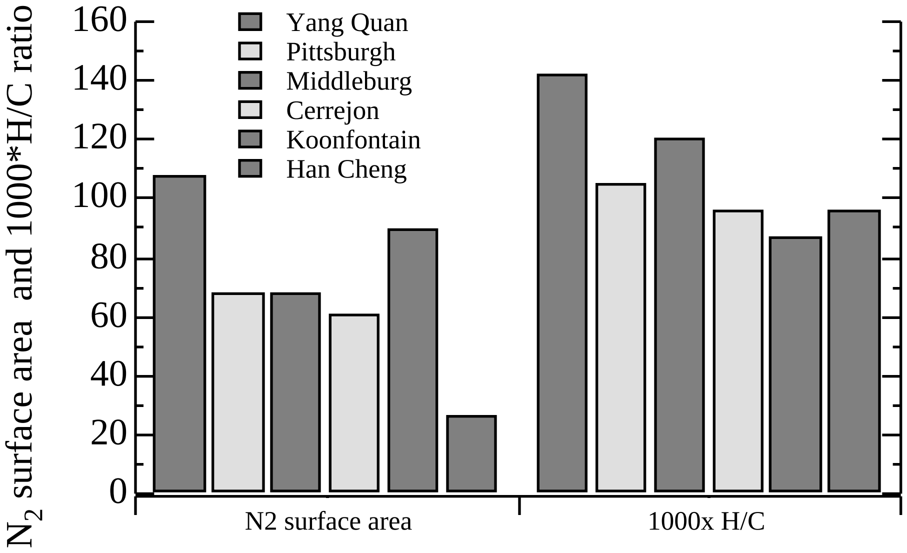

Figure A.9. N_2 surface areas and H/C ratios of six chars (at condition #2 and 1" sampling height)

High Temperature Reactivity

The percent of the daf mass remaining (m/m_0) of Koonfontain chars #2 and #4 from high temperature FFB experiments are plotted as functions of residence time in Figure A.10. The reactivities based on (a) the amount of carbon available in the particles, and (b) the external surface area of a representative particle (which has an average particle size), are shown in Figures A.11 and A.12. From Figures A.11 and A.12 it can be seen that the average (i.e., last set of bars) high temperature reactivity of char #4 is about twice as high as that of char #2, both on a per-gram-of-carbon and on a per-external-surface-area basis. This would indicate that the presence of steam decreases the high temperature reactivity of the Koonfontain char.

The χ factor is the ratio of the observed burning rate to the maximum possible burning rate calculated under film diffusion limitations. The χ factor was calculated for char #2 and #4 in three different intervals: 1~2"; 2~4"; and 4~6". The χ factor is less than 0.10 in most of the cases, as shown in Figure A.13, except for char #4 in the 2 to 4" interval. Therefore, in both conditions, film diffusion limitations are minimal.

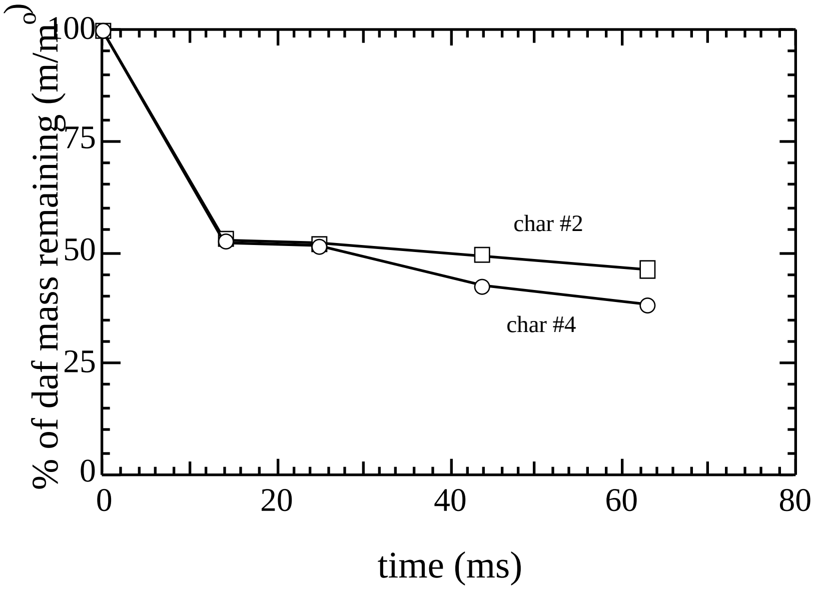

Figure A.10. Percentage of daf mass remaining of Koonfontain chars vs. residence time during char oxidation in condition #2 and #4.

The TGA reactivities of the high temperature Koonfontain chars, collected from the FFB under condition #2 and #4 at 1", 2", 4" and 6", were measured at 550 °C in 10% oxygen. These reactivities are shown in Figure A.14. It can be seen that the chars collected in the #4 reactor condition at 2”, 4” and 6” have much lower TGA reactivities than chars collected in the #2 reactor condition at the same reaction height. Note that high temperature reactivities of chars from the #4 reactor condition were higher than observed for chars from the #2 reactor condition (see Figures A.11 and A.12), but that *the opposite trend* is observed in Figure A.14. This could be because char #4 has a higher activation energy than char #2, or because char #4 has a pore structure that enhances the accessibility of the internal surface area at high temperatures (e.g., the feeder pores are larger).

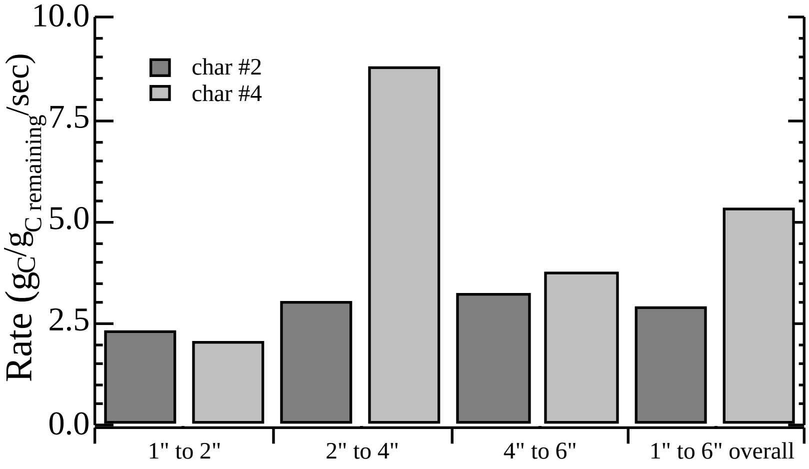

Figure A.11. High temperature reactivities (based on carbon available) of Koonfontain chars from reactor conditions #2 and #4.

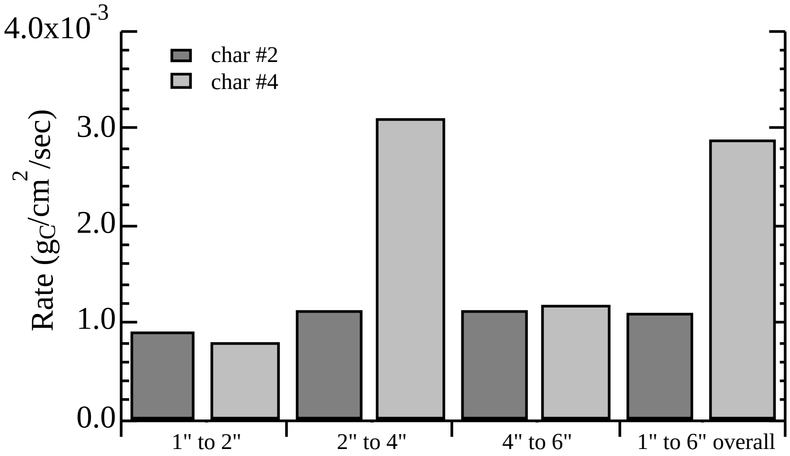

Figure A.12. High temperature reactivities (based on external surface area) of Koonfontain chars from reactor conditions #2 and #4.

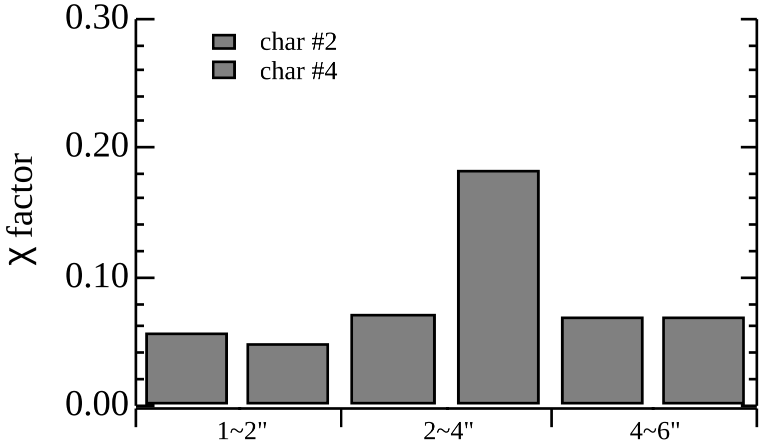

Figure A.13. Values of χ factor in three intervals of reaction length for Koonfontain char oxidation at reactor condition #2 (CH_4 fuel-lean) and condition #4 (CO fuel-lean).

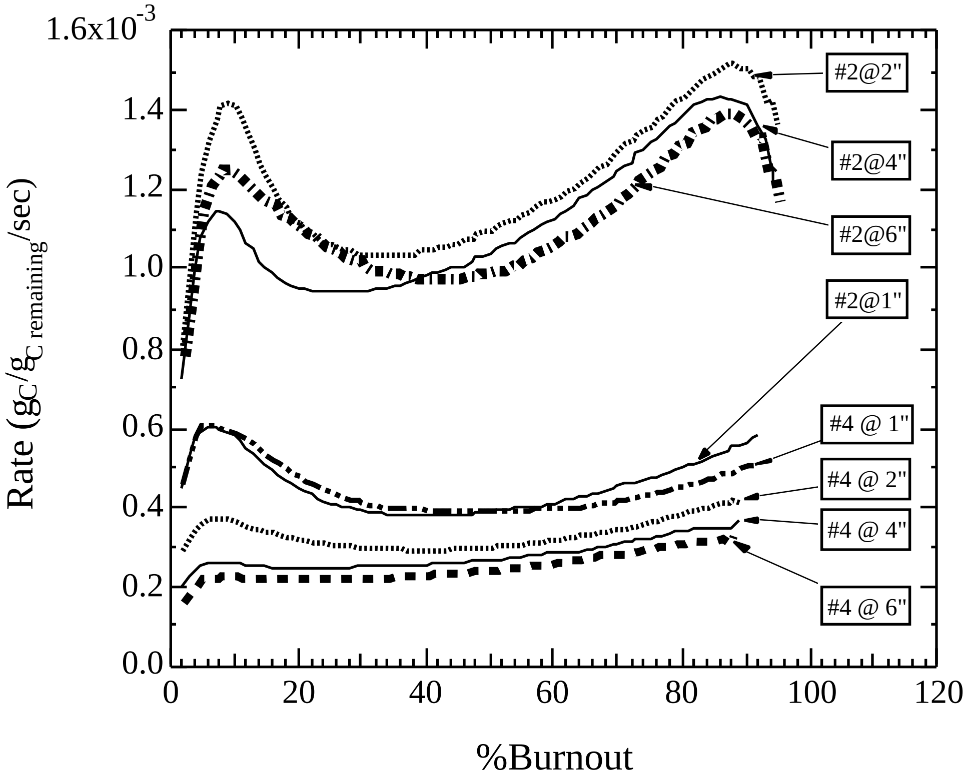

Figure A.14. TGA reactivities of Koonfontain chars from reactor conditions #2 and #4 collected at 1”, 2”, 4”, and 6”.

Elemental Analysis

From Tables A.7 and A.8, it can be seen that the chars made in fuel-lean conditions have lower H/C mole ratio than those chars made in fuel-rich conditions, as shown in Figure A.15. This may explain the higher reactivities of the chars made in fuel-rich conditions, since char reactivity has been correlated with hydrogen content (Charpenay *et al.*, 1992).

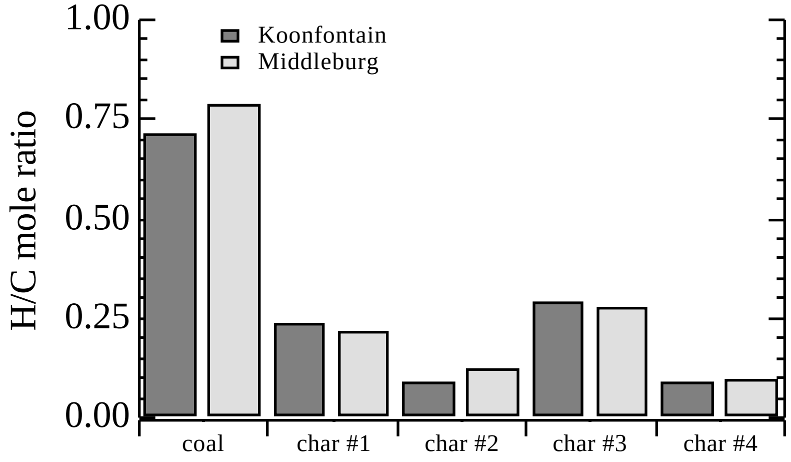

Figure A.15. H/C mole ratios of Koonfontain and Middleburg coals and chars prepared at four different conditions (at the 1” sampling height).

A problem was found in calculating the oxygen composition in some chars. The elemental analyzer only analyzes elemental compositions of C, H, N, and S. The value of ash content from the proximate analysis is used to convert the C, H, N, and S compositions to daf basis. The oxygen content is then calculated by difference: O% = 100% - (C%+H%+N%+S%). However, negative values were sometimes obtained for the oxygen content of these chars. Several possible reasons are listed here:

A. The ash content from the proximate analysis is too high. In the proximate analysis the ashing temperature is 750 °C but in the CHNS analysis the ashing temperature is 900 °C. Therefore, the ash content may be overestimated in the proximate analysis. However, the proximate analysis was repeated using an ashing temperature of 900 °C, but no change in the value of ash content was observed.

B. The deviations associated with the C, H, N, S contents are accumulated when oxygen content is calculated by difference. When the true value of oxygen content is very close to zero, the accumulated error can easily cause the calculated value of oxygen content to become slightly negative.

C. The standard coal sample (with known composition) may have a carbon content that is too low. The CHNS analyzer works best when the coal or char sample to be analyzed has a similar composition with the standard coal sample. Additional standards of coals and cokes with higher carbon contents will be used in the future to better calibrate the instrument.

D. The sulfur measured in the CHNS analysis is the total sulfur, including both inorganic and organic sulfur. Therefore, the inorganic sulfur contributes to inaccuracies in the mass balance.

Regardless of the slight negative oxygen concentrations for some chars, the H/C ratio can be used with confidence since it is independent of the O_2 concentration.

Conclusions

The presence of oxygen in the char preparation environment was examined by performing experiments in fuel-rich and fuel-lean FFB conditions. The following effects were observed for both the Koonfontain and Middleburg coals:

1) The mass release of chars obtained in conditions with post-flame O_2 exhibited 5-7% more mass release (on an absolute daf basis) than corresponding chars produced in fuel-rich environments. This was likely due to the initiation of char oxidation in the fuel-lean reactor conditions.

2) The H/C ratio is lower in the chars produced with O_2 present, i.e., more hydrogen is lost during pyrolysis in the presence of O_2.

3) Chars produced in the presence of O_2 exhibited a lower N_2 BET surface area, a lower TGA reactivity, and a slightly lower CO_2 surface area than corresponding chars produced in a fuel-rich environment. TGA reactivity correlates well with N_2 BET surface area, but does not correlate well with CO_2 surface area.

The presence of steam on char formation was studied by performing experiments in CH_4 flames and in CO flames in the FFB. The observed effects of steam were:

1) Markedly reduced steam concentration (<1%, condition #3 compared to condition #1) in the char preparation environment led to higher TGA reactivity of the resultant char at 550 ^{o} C. Moderately reduced steam concentration (5%, condition #4 compared to condition #2) did not affect TGA reactivity of the char.

2) Moderately reduced steam concentration (5%, condition #4 compared to condition #2) in the char preparation environment and in the oxidation environment led to notably higher reaction rates at typical industrial combustor temperature (about 1650 K), but lower TGA reactivities.

Appendix B: Errors and Standard Deviation

In the model evaluation session (Chapter 8), the word “error” is used to represent the relative error, which is defined as

$$x = \frac{\text{calculated value} - \text{measured value}}{\text{measured value}} \times 100\% \qquad \text{B.1}$$

The standard deviation σ is defined as

$$\sigma = \sqrt{\frac{\sum_{i=1}^{n} (x_i - \bar{x})^2}{(n-1)}} = \sqrt{\frac{n\sum_{i=1}^{n} x_i^2 - \left(\sum_{i=1}^{n} x_i\right)^2}{n(n-1)}} \qquad \text{B.2}$$

where x_i is the i-th relative error, n is the total number of measurements (equal to the number of relative errors), and $\bar{x}$ is the arithmetic mean of all x_i,:

$$\bar{x} = \frac{1}{n}\sum_{i=1}^{n} x_i \qquad \text{B.3}$$

The maximum error is the maximum of all relative errors:

$$x_{\max} = \max(x_1, x_2, x_3, \cdots, x_{n-1}, x_n) \qquad \text{B.4}$$